

**NUMERICAL SIMULATION OF STEADY AND PULSATILE FLOW IN STENOSED
TAPERED ARTERY AND ABDOMINAL AORTIC ANEURYSM USING κ - ω MODEL**

A Thesis by

Chiragkumar D. Tala

Bachelor of Engineering, Gujarat University, 2007

Submitted to the Department of Aerospace Engineering
and the faculty of the Graduate School of
Wichita State University
in partial fulfillment of
the requirements for the degree of
Master of Science

December 2010

© Copyright 2010 by Chiragkumar D. Tala

All Rights Reserved

**NUMERICAL SIMULATION OF STEADY AND PULSATILE FLOW IN STENOSED
TAPERED ARTERY AND ABDOMINAL AORTIC ANEURYSM USING κ - ω MODEL**

The following faculty members have examined the final copy of this thesis for form and content, and recommend that it be accepted in partial fulfillment of the requirement for the degree of Master of Science with a major in Aerospace Engineering.

Klaus A. Hoffmann, Committee Chair

Roy Y. Myose, Committee Member

Hamid M. Lankarani, Committee Member

DEDICATION

To my family, friends, and teachers

ACKNOWLEDGEMENTS

I would like to thank my advisor, Dr. Klaus A. Hoffmann for kindly helping me throughout my studies. I gained much experience from him during the course of my thesis, which I believe was not possible in the coursework alone. In many instances, my work was not up to his requirements, whereupon he patiently explained concepts and guided me professionally.

I would also like to express my gratitude to Dr. Jean-Francois Dietiker for his guidance regarding user-defined function. I believe that without his guidance, I would not have finished this thesis in time.

Last but not least, I thank my college friend and colleague Parth Dave for his selfless support in understanding the software and guiding me through the fluid dynamics concepts.

ABSTRACT

The effect of hemodynamics on cardiovascular disease (CVD) is very important since CVD is the number one killer nationwide and around the globe. Coronary artery disease (CAD), also called arteriosclerosis, is a common disease found in human arteries, including coronary arteries and the common carotid artery. The abdominal aorta is also affected by atherosclerotic aneurysm.

Formation of atherosclerosis obstructs the blood flow in arteries and changes the hemodynamics pattern. Numerical and experimental modeling in a tapered artery using turbulent models has been untouched so far. To investigate the cause of atherosclerosis and atherosclerotic aneurysm, simulations were done using the finite volume method via FLUENT 6.3.26.

Wilcox's two-equation standard κ - ω model was used for numerical simulation of a tapered artery and abdominal aortic aneurysm. The tapered artery had a diameter reduction of 25 percent at the stenosed area. The two-equation turbulence κ - ω model was employed on a geometry to validate the numerical results with velocity profiles of experimental results. Blood was assumed to be Newtonian in all simulations.

The main objectives of this thesis were as follows:

1. To study the shear stress and blood streamlines of tapered artery at different Reynolds number using the κ - ω model.
2. To simulate the pulsatile flow conditions on a tapered artery and abdominal aortic aneurysm.
3. To predict and validate the kick-start of atherosclerosis based on hemodynamic conditions.
4. To study the effect of turbulent viscosity on shear stress.

TABLE OF CONTENTS

Chapter	Page
1. INTRODUCTION	1
1.1 Motivation and Challenge.....	1
1.1.1 Out-of-Hospital Cardiac Arrest.....	2
1.1.2 Coronary Heart Disease	2
1.1.3 Stroke	3
1.1.4 High Blood Pressure	5
1.1.5 Congenital Cardiovascular Disease	5
1.1.6 Heart Failure.	6
1.2 Literature Review.....	7
1.2.1 Atherosclerosis.....	9
1.2.2 Abdominal Aortic Aneurysm.....	13
1.2.3 Stenosis	15
1.3 Cell Biology of Vessels	18
1.4 Biomechanics of Arterial Aneurysm	19
1.4.1 Thoracic Aortic Aneurysm.....	20
1.4.2 Cerebral Aneurysm	21
1.4.3 Peripheral Aneurysm	22
1.4.4 Fusiform Aneurysm	23
1.4.5 Pathogenesis for Arterial Aneurysm.....	23
1.4.6 Progression and Enlargement Rate	25
1.5 Introduction to Arterial Modeling.....	25
1.6 Two Theories for Aneurysm Progression.....	26
1.7 Difficulties in Modeling Blood Flow.....	27
1.8 Fluid Mechanics.....	28
1.9 Damages and Adaptation of Blood Vessels.....	30
1.9.1 Biological Response to Hemodynamic Process.....	30
1.9.2 Hemostasis	30
2. DESCRIPTION OF MODELS.....	31
2.1 Tapered Artery	31
2.2 Abdominal Aortic Aneurysm.....	32
3. GRID GENERATION	35
3.1 Tapered Stenosed Artery.....	35
3.2 Abdominal Aortic Aneurysm.....	38

TABLE OF CONTENTS (continued)

Chapter	Page
4. SOLUTION PROCEDURE.....	41
4.1 Governing Equations	41
4.2 Turbulence Model.....	42
4.3 Boundary Conditions	46
4.4 Physical Properties.....	47
4.4.1 Density	47
4.4.2 Viscosity (Newtonian)	47
4.5 Discretization Scheme	47
4.6 Relaxation Parameters	47
4.7 Convergence Criteria	47
4.8 Advantages of Original κ - ω Model by Wilcox.....	48
4.9 Disadvantages of κ - ω Model by Wilcox.....	48
5. VALIDATION AND GRID INDEPENDENCE.....	49
5.1 Validation of κ - ω Steady Case.....	49
5.2 Grid Independence	53
6. RESULTS	55
7. CONCLUSIONS.....	85
8. FUTURE RECOMMENDATIONS	87
REFERENCES	88
APPENDIXES.....	97
A. UDF for Steady Case.....	98
B. UDF for Pulsatile Case.....	99

LIST OF TABLES

Table	Page
1.1 Comparison of Patients Suffering from Heart Disease in 2004 and 2010	2
1.2 Portion of Total Congenital Cardiovascular Mortality for Males vs Females	6
1.3 2006 National Health Care Cost and Utilization Project Statistics: Mean Charges and In-Hospital Death Rates for Various Procedures	7
1.4 Estimated Direct and Indirect Costs (in billions of dollars) of CVD and Stroke: US 2009	7
2.1 Geometrical Aspects of Steady and Pulsatile Case Flow	32
3.1 Various Aspects of Boundary Layer Mesh for Geometry with 25 Percent Stenosed Artery	36
3.2 Skewness Value of Grid Elements	38
3.3 Various Aspects of Boundary Layer Mesh for AAA	40
3.4 Skewness Value of Grid Elements for AAA	40

LIST OF FIGURES

Figure	Page
1.1 Prevalence of Coronary Heart Disease by Age and Sex (NHANES, 1999–2004).....	3
1.2 Prevalence of Stroke by Age and Sex.....	4
1.3 Prevalence of HBP in Americans of Age 20 Years and Older by Age and Sex.....	5
1.4 Illustration of Balloon Angioplasty	11
1.5 Illustration of Stenting Procedure	11
1.6 Schematic Showing Layers of Artery.....	18
1.7 Different Forms of Aneurysm.....	19
1.8 Thoracic Aortic Aneurysm	20
1.9 Cerebral Aneurysm	21
1.10 Peripheral Aneurysm	22
2.1 Cross Section of Tapered Stenosed Artery	31
2.2 Schematic Diagram of Tapered Stenosed Artery with 25 Percent Diameter Reduction.....	31
2.3 Cross Section of Abdominal Aortic Aneurysm	33
2.4 Schematic Diagram of Abdominal Aortic Aneurysm (not scaled).....	33
3.1 Three-Dimensional Grid of Tapered Artery with 25 Percent Diameter Reduction.....	36
3.2 Mesh at Inlet of Geometry with 25 Percent Diameter Reduction.....	37
3.3 Mesh at Outlet of Geometry with 25 Percent Diameter Reduction	37
3.4 Magnified View of Mesh at Stenosis Region with 25 Percent Diameter Reduction.....	38
3.5 Three-Dimensional Grid of Abdominal Aortic Aneurysm.....	39
3.6 Magnified View of Abdominal Aortic Aneurysm	39
3.7 Inlet and Outlet Mesh of Abdominal Aortic Aneurysm	40

LIST OF FIGURES (continued)

Figure	Page
5.1	Location where X-Velocity Profiles are Compared with Experimental Results49
5.2	X-Velocity Profile for $X = 0.0 D$50
5.3	X-Velocity Profile for $X = 1.0 D$51
5.4	X-Velocity Profile for $X = 2.5 D$51
5.5	X-Velocity Profile for $X = 4.0 D$52
5.6	X-Velocity Profile for $X = 5.0 D$52
5.7	X-Velocity Profile for $X = 6.0 D$53
5.8	Comparison of WSS for Model 1 with $\theta = 0.5^\circ$ and Taper 50 Percent Diameter Reduction53
6.1	Comparison of WSS for $Re = 100\text{--}900$ with $T_{int} = 0.1$56
6.2	Comparison of WSS for $Re = 1100\text{--}1500$ with $T_{int} = 0.1$56
6.3	X-Velocity Contours and Streamlines for $Re = 100, T_{int} = 0.1$58
6.4	X-Velocity Contours and Streamlines for $Re = 300, T_{int} = 0.1$58
6.5	X-Velocity Contours and Streamlines for $Re = 500, T_{int} = 0.1$59
6.6	X-Velocity Contours and Streamlines for $Re = 700, T_{int} = 0.1$59
6.7	X-Velocity Contours and Streamlines for $Re = 900, T_{int} = 0.1$60
6.8	X-Velocity Contours and Streamlines for $Re = 1100, T_{int} = 0.1$60
6.9	X-Velocity Contours and Streamlines for $Re = 1300, T_{int} = 0.1$61
6.10	X-Velocity Contours and Streamlines for $Re = 1500, T_{int} = 0.1$61
6.11	Comparison of WSS for $Re = 100\text{--}900$ with $T_{int} = 1.0$62
6.12	Comparison of WSS for $Re = 1100\text{--}1500$ with $T_{int} = 1.0$62

LIST OF FIGURES (continued)

Figure	Page
6.13 Comparison of WSS for $Re = 100-900$ with $T_{int} = 2.0$	63
6.14 Comparison of WSS for $Re = 1100-1500$ with $T_{int} = 2.0$	63
6.15 Comparison of WSS for $Re = 100-900$ with $T_{int} = 4.0$	64
6.16 Comparison of WSS for $Re = 1100-1500$ with $T_{int} = 4.0$	64
6.17 X-Velocity Contours and Streamlines for $Re = 100, T_{int} = 4.0$	65
6.18 X-Velocity Contours and Streamlines for $Re = 300, T_{int} = 4.0$	65
6.19 X-Velocity Contours and Streamlines for $Re = 500, T_{int} = 4.0$	66
6.20 X-Velocity Contours and Streamlines for $Re = 700, T_{int} = 4.0$	66
6.21 X-Velocity Contours and Streamlines for $Re = 1300, T_{int} = 4.0$	67
6.22 X-Velocity Contours and Streamlines for $Re = 1500, T_{int} = 4.0$	67
6.23 Comparison of WSS for $Re = 100-900$ with $T_{int} = 0.1$ for $T_{\kappa-\omega}$ Model.....	69
6.24 Comparison of WSS for $Re = 1100-1500$ with $T_{int} = 0.1$ for $T_{\kappa-\omega}$ Model.....	69
6.25 Comparison of WSS for $Re = 100-900$ with $T_{int} = 2.0$ for $T_{\kappa-\omega}$ Model.....	70
6.26 Comparison of WSS for $Re = 1100-1500$ with $T_{int} = 2.0$ for $T_{\kappa-\omega}$ Model.....	70
6.27 Recirculation as a Function of Reynolds Numbers with 25 Percent Diameter Reduction under Steady Condition for $\kappa-\omega$ Model with $T_{int} = 0.1, 1.0, 2.0, 4.0$	71
6.28 Recirculation as a Function of Reynolds Numbers with 25 Percent Diameter Reduction under Steady Condition for $T_{\kappa-\omega}$ Model with $T_{int} = 0.1, 2.0$	71
6.29 Comparison of Recirculation Length as a Function of Reynolds Numbers with 25 Percent Diameter Reduction of $\kappa-\omega$ and $T_{\kappa-\omega}$ Models with Different Turbulent Intensities.	71
6.30 Validation for Pulsatile Case	73
6.31 Comparison of WSS using Unsteady $\kappa-\omega$ Model with $T_{int} = 0.1$ at $t/T = 0.25$	76

LIST OF FIGURES (continued)

Figure	Page
6.32 Comparison of WSS using Unsteady $\kappa\text{-}\omega$ Model with $T_{\text{int}} = 0.1$ at $t/T = 0.5$	77
6.33 Comparison of WSS Using Unsteady $\kappa\text{-}\omega$ Model with $T_{\text{int}} = 0.1$ at $t/T = 0.75$	77
6.34 Comparison of WSS Using Unsteady $\kappa\text{-}\omega$ Model with $T_{\text{int}} = 0.1$ at $t/T = 1.0$	78
6.35 WSS of AAA Using Unsteady $\kappa\text{-}\omega$ Model with $T_{\text{int}} = 0.1$ at $t/T = 0.25$	79
6.36 WSS of AAA Using Unsteady $\kappa\text{-}\omega$ Model with $T_{\text{int}} = 0.1$ at $t/T = 0.5$	80
6.37 WSS of AAA Using Unsteady $\kappa\text{-}\omega$ Model with $T_{\text{int}} = 0.1$ at $t/T = 0.75$	80
6.38 WSS of AAA Using Unsteady $\kappa\text{-}\omega$ Model with $T_{\text{int}} = 0.1$ at $t/T = 1.0$	81
6.39 X-Velocity Contour and Streamlines for $t/T = 0.25$	82
6.40 X-Velocity Contour and Streamlines for $t/T = 0.5$	83
6.41 X-Velocity Contour and Streamlines for $t/T = 0.75$	83
6.42 Schematic of Geometry Showing X-Velocity Contour and Streamlines for $t/T = 0.75$	84
6.43 X-Velocity Contour Streamlines for $t/T = 1.0$	84

LIST OF ABBREVIATIONS

AAA	Abdominal Aortic Aneurysm
AP	Angina Pectoris
CFD	Computational Fluid Dynamics
CHD	Coronary Heart Disease
CVA	Cerebrovascular Accident
CVD	Cardiovascular Disease
EC	Endothelial Cell
EMS	Emergency Medical Services
EU	European Union
FDM	Finite Difference Method
FEM	Finite Element Method
FGF-2	Fibroblast Growth Factor-2
FVM	Finite Volume Method
HBP	High Blood Pressure
HF	Heart Failure
IH	Intimal Hyperplasia
MCP-1	Monocyte Chemoattractant Protein-1
MI	Miocardial Infarction
NCHS	National Center for Health Statistics
NHANES	National Health and Nutrition Examination Survey
NO	Nitrogen Oxide
PDGF-A	Platelet Derived Growth Factor-A

LIST OF ABBREVIATIONS (continued)

SMC	Smooth Muscle Cells
UDF	User-Defined Function
VEC	Vascular Endothelial Cell
VSMC	Vascular Smooth Muscle Cells
WSS	Wall Shear Stress
WSSG	Wall Shear Stress Gradient
WSSTG	Wall Shear Stress Temporal Gradient

LIST OF VARIABLES

(u_i)	Phase-Averaged Velocity in the X Direction
κ	Turbulent Kinetic Energy
(κ)	Phase Averaged Turbulent Kinetic Energy
l	Turbulent Length Scale
D	Diameter
(D_H)	Hydraulic Diameter
ω	Specific Dissipation Rate
(ω)	Phase-Averaged Specific Dissipation Rate
U_{avg}	Mean Flow Velocity
ρ	Density
μ	Dynamic Viscosity
μ_t	Turbulent Eddy Viscosity
I	Turbulent Intensity
(p)	Phase-Averaged Pressure
Re	Reynolds Number
Re_t	Turbulent Reynolds Number
α	Womersley Number
$T_{\kappa-\omega}$	Transitional Version of $\kappa-\omega$ Model
V_m	Inlet Velocity
T_{int}	Turbulent Intensity

CHAPTER 1

INTRODUCTION

1.1. Motivation and Challenge

Cardiovascular disease (CVD) is turning out to be a major health concern in the western world. Twenty million deaths occurred in 2002, out of which 5.5 million were due to strokes alone [1]. A person of age 20 or above is considered an adult. On average, 80,070,000 American adults have one or more types of cardiovascular disease, and of these, 38,200,000 are at least 60 years old.

Each year CVD causes 4.3 million deaths in Europe and more than 2.0 million deaths in the European Union (EU). This translates to 48 percent of the deaths in Europe and 42 percent of the deaths in the EU. CVD is the main cause of death among women in all countries of Europe and is the main cause of death among men in all countries except France, the Netherlands, and Spain. Deaths occurring from coronary heart disease (CHD) are generally higher in Central and Eastern Europe than in Northern, Southern, and Western Europe. The death rate due to stroke is generally higher in Central and Eastern Europe than in Northern, Southern, and Western Europe. Every year, the EU spends around £ 192 billion for the treatment of CVD. The main aim for mentioning these statistics is to show the prevalence of CVD disease and number of deaths as the result of it in Europe and U.S.

It is estimated that one in every three American adults (around 81,000,000 people) suffers from different types of CVD. Of these patients, 38,000,000 are age 60 or older [2]. Table 1.1 compares the number of patients suffering from heart disease in 2004 and 2010.

TABLE 1.1

COMPARISON OF PATIENTS SUFFERING FROM HEART DISEASE IN 2004 AND 2010 [2]

DISEASE	NUMBER OF PATIENTS	
	2004	2010
Coronary Heart Disease	16,000,000	17,600,000
Myocardial Infarction (MI or heart attack)	8,100,000	8,500,000
Angina pectoris (AP or chest pain)	9,100,000	10,200,000
Stroke	5,800,000	6,400,000
Congenital Cardiovascular Defects	650,000–1,300,000	650,000–1,300,000

1.1.1. Out-of-Hospital Cardiac Arrest

According to statistics of the National Center for Health Statistics (NCHS) Data Warehouse, approximately 310,000 deaths as the result of CHD in 2004. These deaths occurred out of the hospital (home, work, on the way to hospital, etc.) or in a hospital emergency department [3]. In 2010, around 60 percent of sudden cardiac deaths are treated by the Emergency Medical Services (EMS) [4]. Also in 2010, the estimated amount of money spent for CHD is \$ 177.1 billion, compared to \$ 156.4 billion in 2008. One of the reasons for this increase in health costs is because of the soaring price of health care facilities.

1.1.2. Coronary Heart Disease

CHD is the leading cause of human death. The prevalence of CHD among adults from 2003 to 2006 was 16,000,000, of which 8,700,000 were men and 7,300,000 were women. In 2010, it is estimated that 785,000 Americans will suffer from new coronary attacks, and 470,000 will have recurring attacks. It is predicted that 195,000 silent first heart attacks will occur in 2010. It is believed that 600,000 new American patients will suffer from their first heart attack, and around 320,000 patients will have recurrent annual attacks in 2010. In 2010, the average age of a person's first heart attack is calculated to be 64.5 years for men and 70.3 years for women. About 38 percent of people who die experience a fatal coronary attack in a given year, and 82

percent of people who die from CHD are age 65 or more. From 1994 to 2004, non-sudden CHD deaths decreased by 64 percent, and sudden deaths fell by 49 percent [5]. Figure 1.1 illustrates the prevalence of CHD by age and sex from 1994 to 2004.

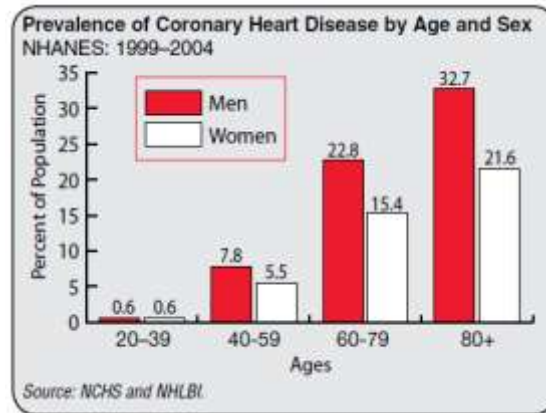


Figure 1.1 Prevalence of Coronary Heart Disease by Age and Sex (NHANES,1999–2004) [2].

The risk factors for CHD are summarized below [5]:

- High total blood pressure
- High cholesterol level
- Hypertension
- Cigarette smoking and diabetes

1.1.3. Stroke

In medical terms, stroke is a cerebrovascular accident (CVA). Stroke occurs when the supply of the blood is disturbed or decreased. A severe stroke can damage the brain and cause paralysis.

The two types of stroke are ischemic and hemorrhagic.

- Ischemic Stroke
 - Embolism (sometimes due to the high velocity of blood or weakening of the cellular material), whereby a clot detaches from the blood vessel and blocks the flow downstream in the brain.

- Thrombosis (obstruction to blood flow by formation of local blood clotting).
- Systemic hypo-perfusion (due to arrhythmia of the heart), whereby the blood supply is decreased to brain.
- Venous thrombosis (local venous pressure exceeds the arterial pressure).
- Hemorrhagic Stroke
 - Intra-axial hemorrhage (blood gathers in the brain).
 - Extra-axial hemorrhage (blood gathers outside the brain but inside the skull).

Figure 1.2 illustrates the prevalence of stroke by age and sex from 1999 to 2004. Among adults in the United States, the prevalence of stroke in 2006 was 6,400,000 of which 2,500,000 were males and 3,900,000 were females [2]. Every year about 795,000 people experience a new or recurrent stroke in the U.S. Out of 795,000 patients, 610,000 are new stroke patients and 185,000 are recurrent ones. On average, every 40 seconds, one person in the U.S. has a stroke. Approximately 55,000 more women than men in the U.S. have a stroke each year. Blacks are two times more vulnerable to stroke than whites. The risk of ischemic stroke in smokers is about double that of non-smokers. High blood pressure is also a main cause of stroke. The estimated direct and indirect cost of stroke in the U.S. in 2010 is estimated to be \$ 73.7 billion [1]. Stroke is also considered to be the leading cause of serious, long-term disability in the United States.

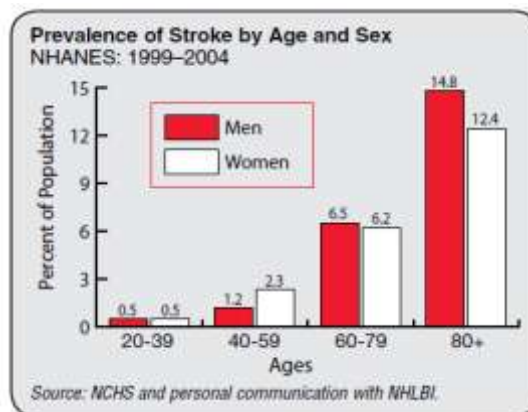


Figure 1.2 Prevalence of stroke by age and sex [2].

1.1.4. High Blood Pressure

CVD includes high blood pressure (HBP). A person is said to be hypertensive if the systolic pressure is 140 mm Hg or greater and/or the diastolic pressure of 90 mm Hg or greater. In 2005, the estimated prevalence for HBP was 74,500,000 in the United States. Out of 74,500,000 HBP patients, 35,700,000 of them were males and 38,800,000 were females [2]. Nearly one out of every three people in the U.S. has HBP [2]. The prevalence of HBP in Americans by age and sex is shown in Figure 1.3. As can be seen, from age 45 to 50, the number of males and females suffering from HBP is the same. Past the age of 50, more women suffer from HBP than men do [6]. In 2010, the direct and indirect amount of money spent for the treatment of HBP in the U.S. is estimated to be \$ 76.6 million.

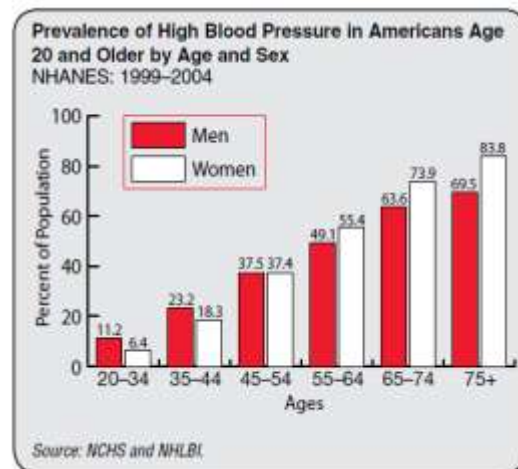


Figure 1.3 Prevalence of HBP in Americans of age 20 years and older by age and sex [2].

1.1.5. Congenital Cardiovascular Disease

In 2020, the cost of congenital cardiovascular disease in the United States was estimated to be between \$ 650,000 and \$ 1,300,000 [7] as shown in Table 1.2. Congenital cardiovascular defects, also known as congenital heart defects, are structural problems arising from the abnormal formation of the heart or major blood vessels [2].

TABLE 1.2

PORTION OF TOTAL CONGENITAL CARDIOVASCULAR MORTALITY
FOR MALE VS FEMALES [2]

Population Group	Estimated Prevalence All Ages	Incidence in Infants	Mortality 2004 All Ages	Hospital Discharges 2005 All Ages
Both sexes	650,000 to 1.3 million	36,000	3,861	59,000
Males	—	—	2,087 (54.1%)*	29,000
Females	—	—	1,774 (45.9%)*	30,000
White males	—	—	1,640	—
White females	—	—	1,422	—
Black males	—	—	364	—
Black females	—	—	293	—

NOTE: — = data not available.* These percentages represent the portion of total congenital cardiovascular mortality that is for males vs females.

Sources: *Mortality: NCHS (these data represent underlying cause of death only; data for white and black males and females include Hispanics). Hospital discharges: NHDS, NCHS; data include inpatients discharged alive, dead, or status unknown.*

1.1.6. Heart Failure

In 2010, the estimated prevalence of heart failure (HF) in adults of age 20 and older was 5,800,000. Of this number, about 3,100,000 were males and 2,700,000 were females [2]. The estimated cost of HF in 2010 is \$ 39.2 billion. At age 40, the lifetime risk of developing HF for both men and women is one in five. In spite of excellent medical facilities, a large number of people die in the U.S. alone. Table 1.3 illustrates different heart surgery procedures and mean charges for these procedures for the year 2006. Table 1.4 lists the estimated direct and indirect costs in billions for CVD and stroke.

TABLE 1.3

2006 NATIONAL HEALTH CARE COST AND UTILIZATION PROJECT STATISTICS:
MEAN CHARGES AND IN-HOSPITAL DEATH RATES FOR VARIOUS PROCEDURES [8]

Procedure	Mean Charge	In-Hospital Death Rate (percent)
Coronary Artery Bypass Graft	\$ 99,743	1.94
Percutaneous Coronary Intervention	48,399	0.71
Diagnostic Cardiac Catheterization	28,835	0.77
Pacemaker	47,081	0.90
Implantable Defibrillator	104,743	0.64
Endarterectomy	25,658	0.38
Valves	141,120	4.98

TABLE 1.4

ESTIMATED DIRECT AND INDIRECT COSTS (IN BILLIONS OF DOLLARS)
OF CVD AND STROKE: US 2009 [2]

	Heart Disease	Coronary Heart Disease	Stroke	Hypertensive Disease	Heart Failure	Total Cardiovascular Disease
Direct Cost						
Hospital	\$106.3	\$54.6	\$20.2	\$ 8.2	\$20.1	\$150.1
Nursing Home	23.4	12.3	16.2	4.8	4.5	48.2
Physicians/Others	23.8	13.4	3.7	13.4	2.4	46.4
Drugs/Other						
Medical Durables	22.1	10.3	1.4	25.4	3.3	52.3
Home Health Care	7.4	2.2	4.4	2.4	3.4	16.8
Total Expenditures	183.0	92.8	45.9	54.2	33.7	313.8
Indirect Costs						
Morbidity	24	10.6	7.0	8.4	NA	39.1
Mortality	97.6	62.0	16.0	10.8	3.5	122.4

1.2. Literature Review

Until 1980, it was difficult to model blood flow due to the lack of computing power and lack of sufficient knowledge in the field of computational fluid dynamics. Now it is possible to model blood flow, but there are still some areas that are untouched and require more attention.

Most investigations concentrate on the bifurcation of the arteries, pressure-velocity distribution, and shear stress concentration. Many investigations consider the arteries as rigid, but in real cases, they are not rigid; therefore, elasticity must be considered in order to simulate the in vivo conditions. It is almost impossible to investigate CVD physically because it takes a long time to develop and is patient-specific. Each patient has his or her own human genetic structure, which differs from others. What might be favorable to one person may not be favorable to another person. Various numerical techniques used by researchers to investigate blood flow in humans using computational fluid dynamics (CFD) are the finite element method (FEM), finite difference method (FDM), and finite volume method (FVM).

Many experiments have been carried out to study the effect of transient blood flow in bifurcating arteries in order to examine the regions of recirculation and separated blood flow, which are low shear areas or areas that have a high oscillatory shear index. Most fluid mechanic techniques have been applied to the arterial models. Much of the work on particle-tracking velocimetry, hydrogen bubbles, dye-streak lines, photochromic lines, and dye washout has been done by Karino & Goldsmith [9], Ku & Giddens [10], Ohja et al. [11], Keynton et al. [12], Nerem & Seed [13], Friedman et al. [14], and Khalifa & Giddens [15]. Ku & Giddens [16] worked on Doppler ultra sound to construct detailed velocity profiles in blood vessels. Recently Meier et al. [17] and Kim et al. [18] did considerable work on magnetic resonance velocimetry. Close investigation of local hemodynamic condition of the diseased site reveals a strongly consistent curve in which low shear stress is correlated with atherosclerotic intimal hyperplasia (IH). Ku et al. [19], Moore et al. [20] and He & Ku et al. [21] reported that early atherosclerotic lesions develop preferentially in the vicinity of arterial branching and curvature where blood flow patterns are complex and multi-directional.

1.2.1. Atherosclerosis

Atherosclerosis is a disease responsible for CVD. It is a syndrome that affects arterial blood vessels. The Greek word “-ather” means gruel or paste and “-sclerosis” means hardness. In general, it is the name of the process in which deposits of the fatty substance cholesterol, cellular waste products, calcium, and other substances build up in the lining of the arteries. This build-up is called plaque. The built-up plaque occludes the arteries, and as a result of decreased lumen, the blood supply downstream decreases and may even stop in severe cases. This causes severe problems to human life. Atherosclerosis disease tends to be localized in these sites and results in a narrowing of the artery lumen.

Atherosclerosis is asymptomatic for a large period of time and causes two problems. It is unnoticeable and causes no harm until it fully develops. During its course of development, the patient is unaware of the progressing disease. The hardened plaque that forms over a period of time constricts the vessel and occludes the passage of blood. To satisfy the conservation of mass, blood moves at a higher speed through the stenosed site, and if the velocity-induced shear is beyond a certain limit, then the endothelial layer is damaged and thrombosis forms. First, the plaque that forms at the sensitive site over a long period of hardening and withstanding extreme hemodynamic condition tends to rupture and break, which is called thrombosis. Second, if the artery that enlarges in size has an unstoppable growth, then an aneurysm may develop.

Many factors pertaining to human lifestyle are important in atherosclerosis:

- Food habits (diet)
- Smoking
- High blood pressure
- Elevated levels of cholesterol and triglycerides

- Hereditary factors

Tobacco smoking increases the risk of deposition of atherosclerosis in coronary arteries and arteries in the leg. Thrombosis causes damage to the endothelium and results in deposition of fats, cholesterol, platelets, cellular waste products, calcium, and other substances. These substances thicken the endothelium and shrink the lumen of the artery diameter. Decreased lumen decreases the blood supply downstream and hence the oxygen supply. Scientists believe and have proven that hemodynamic conditions play a vital role in the formation of atherosclerosis. However, it is still a challenge to find a specific mechanism by which the arterial disease develops. Atherosclerosis develops on the walls of the artery, diminishing its elasticity and interfering with blood flow.

Atherosclerosis is not completely curable since it grows with time. But various treatments are available to cure the diseased arteries by invasive or non-invasive procedures depending upon the severity of the problem. Two of these types of procedures are as follows:

- Non-Invasive Procedures
 - Cholestipol, cholestyramine
 - Angioplasty
 - Stenting
- Invasive Procedure
 - Bypass surgery

Medications such as cholestipol and cholestyramine are available in drug stores, and there are many more. These drugs are not directly absorbed by the intestines like other drugs and food, but rather combine with bile acids in the intestine to lower the production of cholesterol. Bile acids are formed in the liver from cholesterol. These bile acids are mostly reabsorbed by the

intestine through the liver and bile. Thus, cholestipol forces the liver to convert it into bile acids, which ultimately reduces the cholesterol level in body.

Balloon angioplasty, as shown in Figure 1.4, is another non-invasive procedure, whereby a balloon-tipped catheter is inserted at the stenosed site. It is then inflated by air to flatten the plaque, which opens the artery and increases the blood flow and hence the oxygen supply.

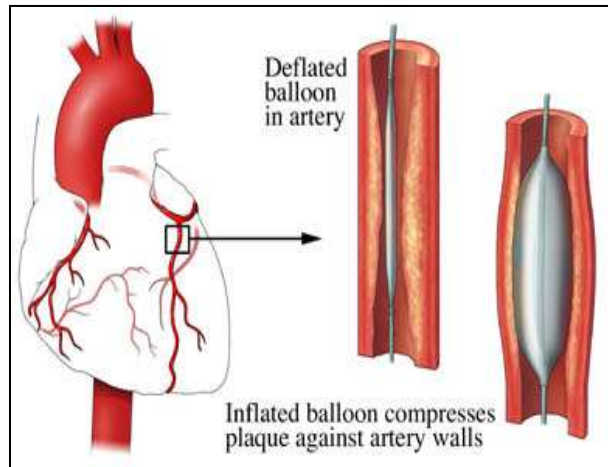


Figure 1.4 Illustration of balloon angioplasty [91].

The third non-invasive procedure, shown in Figure 1.5, is stenting, whereby a metal structure is replaced at a diseased site and inflated by a balloon. The inflated metal structure increases the lumen and blood supply downstream [22].

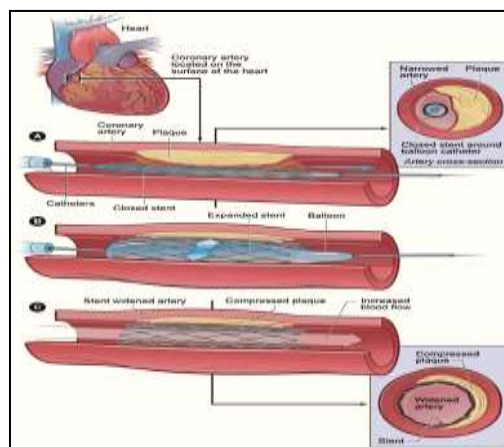


Figure 1.5 Illustration of stenting procedure [92].

The invasive procedure used for atherosclerosis is bypass surgery. In this process either a healthy human artery or vein is used to bypass the blood flow from the stenosed artery. This process of bypassing blood from one part to another is called grafting. It is now possible to bypass blood with certain techniques by using synthetic grafts. Synthetic grafts are of primary importance in patients with pre-existing vascular disease or patients that have already had an autograft procedure. These patients have already used their healthy blood vessels and none remain to serve as replacements. The first artificial graft used in the humans was ePTFE (extended polytetrafluoroethylene) or decron (polyethylene terephthalate) to permanently replace the damage.

Dr. William J. Von Liebig [23] was the first to use patented techniques for manufacturing grafts for use in vascular implants. Currently, research for advanced grafts is being done to treat natural tissues and laboratory-engineered tissues. The success of synthetic grafts is believed to depend on a variety of factors, such as mechanical properties and biocompatibility. With respect to the biocompatibility issue, there are two types of mismatch:

1. Geometrical mismatch, i.e., variation in the diameters of the arteries.
2. Compliance mismatch, i.e., variation in the mechanical properties of both the graft and the artery.

For bypass surgery to be successful, both the geometry and compliance of the host artery and graft should be the same, which is difficult to achieve. The formation of intimal hyperplasia after bypass surgery leads to failure of the bypass graft in 20 to 50 percent of cases [24, 25]. Carrel and Guthrie [26, 27], in the case of bypass grafting after a few days of vein graft implantation, noticed a glistening substance covering the site of the anastomotic stitches that joined the two blood vessels. This covering substance looked similar to an endothelium layer.

After their discovery, IH was cited in vein graft implantation of many mammals like mice, rats, humans, and dogs. IH is not a disease but rather a responsive healing process after the arterial wall is injured. After injury to the endothelium layer, inflammatory mediators are released by endothelial cells, which assist in platelet aggregation. These growth factors promote smooth muscle cells from tunica media to tunica intima. With the healing process and passage of time, smooth muscle cells proliferate in the tunica intima and deposition of extracellular matrix is initiated [28].

1.2.2. Abdominal Aortic Aneurysm

Abdominal aortic aneurysms (AAA) are locally enlarged balloon-shaped expansions found to lie between the region of renal and iliac bifurcation. The precise cause of this disease is still unknown. It is supposedly caused by multi-factors together with several other biological factors. Once the weak area of the artery bulges out, the hemodynamic forces constantly hammer the weaker parts and cause them to lose strength and expand. If it goes on for a long period of time, the geometry, composition, and strength continuously degrade through the enlargement progress, and the artery ruptures when it loses the supportive strength to withstand the degenerative forces. AAA is the 15th leading cause of death [29] and kills almost 15,000 humans in the U.S. every year [30, 31]. AAA is estimated to affect 3 to 9 percent of the population with a mortality rate between 78 to 94 percent [46, 32, 33, 34]. Due to insufficient information on how to decide on operative procedures for aneurysms, current information and knowledge recommend going for an invasive procedure only when the diameter of the aneurysm exceeds 5 cm [35, 36]. This criterion or base for deciding whether to have an operative procedure is not sufficient, since it does not consider the following factors:

- Bulge shape

- Wall thickness
- Flow dynamics
- Blood vessel mechanical properties

It has also been shown that AAAs less than 4 cm do rupture frequently [45, 37]. Willie [38] was the first to numerically simulate the pulsatile blood flow in an aneurysm and identify the presence of a vortex and its variation in size with the cardiac cycle. Perktold et al. [39, 40] showed the velocity vectors and streamlines with pulsatile flow in axisymmetric aneurysm models. Fukushima et al. [41] confirmed numerically and experimentally the presence of a relatively high negative shear stress and variation in pressure at the distal end of an AAA where the flow reattaches. Elger et al. and Budwig et al. [42, 43] did a numerical investigation of blood flow through an AAA and showed the correlation between the blood-flow pattern and its influence on wall shear stress (WSS). Grabowski [44] stated that blood vessels withstand three forces induced by blood flow:

- Tangential shear stress at the inner layer.
- Transmural pressure, which is balanced by hoop stresses.
- Elastic forces, such as wall stretching and flexion.

Fox and Hugh [45], Glagov et al. [46], Hademenos [47], Lei et al. [48], Malek et al. [49], Pedersen et al. [50], Soliman [51], and He and Ku [21] proposed that variation in the hemodynamics of blood flow in the arteries could play a key role in initiation of disease in arteries. Keeping in mind this fact, most researchers focus on analyzing the blood-flow pattern in an aneurysm. Apart from that, certain locations of arteries are more prone to an aneurysm; therefore, study of flow in this segment is of prime importance. Failure of an aneurysm can be considered a material failure due to varying forces as well as material properties [52].

Recently many attempts have been made to determine the dependence of bulge shape and aneurysm diameter on internal stress [53, 54, 55]. Predicting a magnitude of shear stress requires complex boundary conditions. The complex flow pattern in an AAA strongly impacts the stress distribution on the aneurysm wall, clearly indicating the use of complex boundary conditions. Budwig et al. [43] studied the steady flow in an AAA and concluded that wall shear stress in the recirculation zone is ten times less than the shear stress at the entrance length. They also reported two peaks of wall shear stress at the distal end of the aneurysm where the flow reattaches. At present, there is no accurate method to determine the rate of expansion, size or rupture time of an aneurysm. Due to the lack of scientific knowledge on aneurysms, scientists and doctors judge the degree of severity by their size.

1.2.3. Stenosis

Two leading causes of death in the western world are heart attack and stroke due to plaque formation in the carotid and coronary arteries [56]. This is called stenosis. Atherosclerosis is a location-specific disease, which is primarily found in carotid, coronary, and femoral arteries and the abdominal aorta. It has been reported that 15 percent of atherosclerosis cases and 6 percent of other related deaths are due to an AAA. Of the total atherosclerosis cases reported, 35 percent of these people have been advised by doctors to restrict their work and other activities to avoid further worsening of the disease [57]. As the result of many deaths from stenosis, more research in this field needs to be done to accurately predict the shear stress. The complex flow patterns of blood due to multifactors at or downstream of stenosis lead to the formation of plaque, further development of atherosclerosis, or, in severe cases, stenosis, may lead to rupturing in the form of thrombosis [58, 59].

In a healthy vessel without stenosis, the blood flow is laminar (i.e., $Re < 1000$). But the presence of stenosis may induce turbulence [71]. Stein and Subbah [60] studied the coronary artery with stenosis and observed turbulence. It is very labor-intensive to carry out an experimental analysis of pulsatile and transitional flow. In comparison to experimental work, numerical studies offer a wide range of simulations, which was impossible in the past due to the lack of computing capacity and associated cost. Newer-generation computers offer advanced techniques, interface, better resolution, and better speed, compared to experimental results. However, experimental results are still necessary to validate numerical results. Ryval et al. [56] carried out a numerical simulation of 75 and 90 percent stenosed tubes with steady and pulsatile flow. They made a comprehensive study of flow statistics such as velocity, WSS, turbulence intensities, vortex shedding, and transition to turbulence. They compared the recirculation lengths of a simple $\kappa\text{-}\omega$ model with a transitional $\kappa\text{-}\omega$ model and concluded that the transitional version of $\kappa\text{-}\omega$ was found to be more promising for steady conditions.

The steady simulation of a straight stenosed tube was done using Wilcox's $\kappa\text{-}\omega$ model [61, 62] and the results were compared to experimental results [63, 64, 65]. Stroud et al. [66] investigated the steady and pulsatile flow through a severely stenosed artery and concluded that Chien's and Goldberg's study of low Re $\kappa\text{-}\epsilon$ model did not capture the results in different phases of the pulsatile case of laminar and turbulent flows. Dietiker and Hoffmann [67] simulated the steady and pulsatile flow in tapered arteries and noticed that the presence of stenosis increases shear stress at the stenosis site, and flow separation is found downstream of the stenosis. Liu et al. [68] numerically simulated the 2-D stenosed tapered artery and proved that the height of stenosis, more than the degree of taper, plays a major role in the complex blood-flow pattern downstream of the stenosis. With the increase in stenosis, the magnitude of shear stress is found

to increase at the throat and downstream of the throat [83]. Apart from causing damage to the endothelial layer, high WSS also causes intimal thickening, which activates platelets, results in deposition, and finally causes thrombus. Fry [69, 70] was the first to postulate that high shear stress, which is due to the higher flow velocity at the inner layer of an artery, damages the endothelial layer and consequently starts the development of atherosclerosis. Now it is widely accepted that low or oscillating shear stress leads to monocyte adhesion and atherogenesis [15, 21,71]. Studies have proven that low or oscillating shear stress of the artery leads to the adhesion of monocytes to the endothelium during early stages and progression of atherogenesis [72].

The wall shear stress gradient (WSSG) does play a vital role in atherosclerosis development by gene expression related to endothelial cells (ECs). Bao et al. [73] reported that the wall shear stress temporal gradient (WSSTG) expresses two chemicals: monocyte chemo attractant protein-1 (MCP-1) and platelet-derived growth factor-A (PDGF-A). MCP-1 is a chemotactic agent for monocytes, and PDGF-A is a mitogen and chemotactic agent for smooth muscle cells (SMCs) [73].

Apart from fluid shear stress, cyclic mechanical strain also plays a vital role in development of atherosclerosis. Current evidence suggests that ECs and vascular smooth muscle cells (VSMCs) are affected by cyclic strain. Upon mechanical deformation, ECs and VSMCs synthesize MCP-1 [74]. VSMCs are also stimulated by mechanical deformation due to cyclic strain and release fibroblast growth factor-2 (FGF-2) in cultured cells [75]. As a result, smooth muscle migrates and proliferation takes place, resulting in arterial injury [76].

1.3. Cell Biology of Vessels

Arteries consist of three layers, as shown in Figure 1.6:

- Tunica intima
- Tunica media
- Tunica adventitia

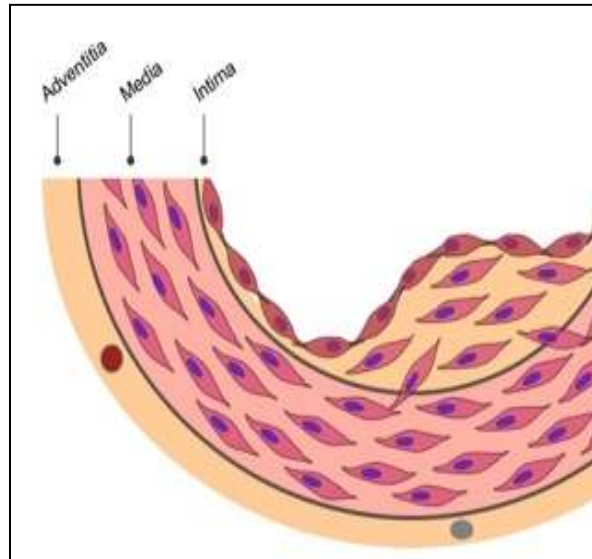


Figure 1.6 Schematic showing layers of artery [77].

Tunica Intima

The innermost layer of a vein or artery, which is directly in touch with blood, is called the tunica intima. It is composed of endothelial cells, which are either polygonal, oval, or fusiform. Endothelium cells are supported and separated from the sub-endothelium by thin basal lamina. The thickness of endothelium cells varies from 0.2 to 0.5 micrometers.

Tunica Media

The middle layer of a vein or artery, which is between the tunica intima and tunica adventitia, is called the tunica media. It is composed of smooth muscle cells and elastic tissues. Tunica media is distinguished from intima and adventitia by its color and structure. This layer is

thin in veins and thicker in arteries. It has a structural base of blood vessels, which gives it elasticity and contractility. Tunica media controls the lumen of blood vessels by contraction and expansion in response to hemodynamic changes.

Tunica Adventitia

The outermost layer a vein or artery is called tunica adventitia and is in direct contact with the tunica media. It is composed of collagen, elastic fibers, and connective tissues. This arrangement controls the over expansion of blood vessels due to changes in blood pressure exerted on walls as the result of blood flow.

1.4. Biomechanics of Arterial Aneurysm

As shown in Figure 1.7, aneurysms come in several forms. Fusiform and saccular are based on their shape. Fusiform aneurysms form before the bifurcation of the artery and are commonly found in the abdominal aorta or in the popliteal artery behind the knee. Saccular aneurysms predominantly are found in the main arteries of the cerebral circulation, mainly along the Circle of Willis.

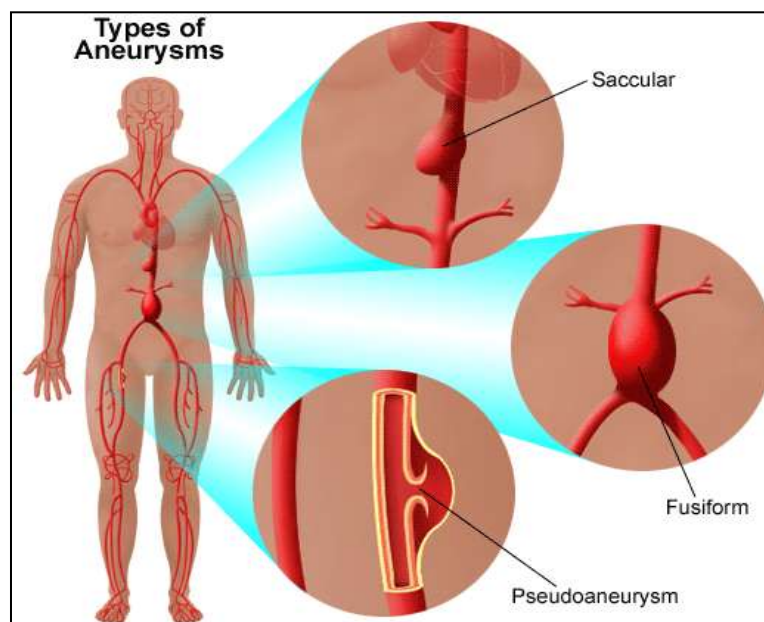


Figure 1.7 Different forms of aneurysm [93].

Pseudoaneurysms form as a result of hole in the arterial wall. The blood localizes outside the arterial wall. Aneurysms are also found in various locations and identified based on those locations. Three of them are as follows:

- Thoracic aortic aneurysm
- Cerebral aneurysm
- Peripheral aneurysm

1.4.1. Thoracic Aortic Aneurysm

An aortic aneurysm occurring in a part of the aorta running through the chest (thorax) is known as a thoracic aortic aneurysm, as shown in Figure 1.8. With this type of aneurysm, the part of the aorta closer to the heart becomes weak and enlarges. This results in improper functioning of the heart valves, leading to leakage of blood going back to the heart. An aneurysm in the abdomen is called an abdominal aortic aneurysm. If the thoracic aortic aneurysm ruptures, the chances of saving the patient are rare, since this aneurysm is in the main artery supplying blood to the bottom half of the body.

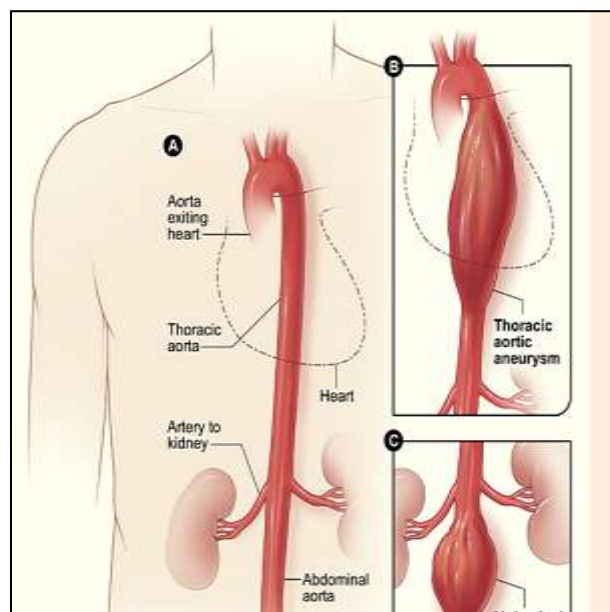


Figure 1.8 Thoracic aortic aneurysm [94].

1.4.2. Cerebral Aneurysm

An aneurysm in the artery of the brain is called a cerebral aneurysm. It is the size of a berry size and is often called a berry aneurysm. No symptoms are noticed until this type of aneurysm becomes very large. This aneurysm seldom ruptures and causes stroke. Its common symptoms are severe headache, nausea, vomiting, weakness, and difficulty in speaking. The danger of a cerebral aneurysm depends on the person's age, health, size, and the location of the aneurysm. Figure 1.9 shows a cerebral aneurysm.

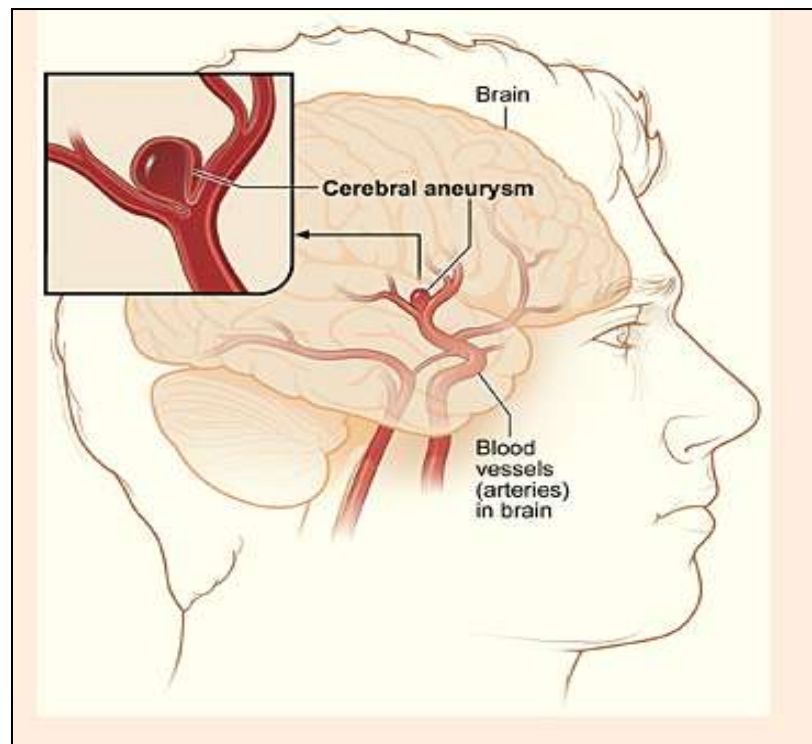


Figure 1.9 Cerebral aneurysm [95].

The causes of a cerebral aneurysm include the following:

- Congenital defect, a degenerative process, or a combination of both.
- A combination of hypertension and atherosclerosis that sometimes disturbs the blood flow, which in turn exerts pressure on the weak artery and leads to its failure.

1.4.3. Peripheral Aneurysm

Figure 1.10 shows a peripheral aneurysm in the arteries that run in the back of the thigh behind the knee, femoral artery, and carotid artery. A popliteal artery that bulges is due to an aneurysm. The symptoms of peripheral aneurysms are pain in the arm while exercising, pain in leg during rest, and numbness in arm. A life-threatening situation occurs when the carotid artery is infected instead of the popliteal artery.

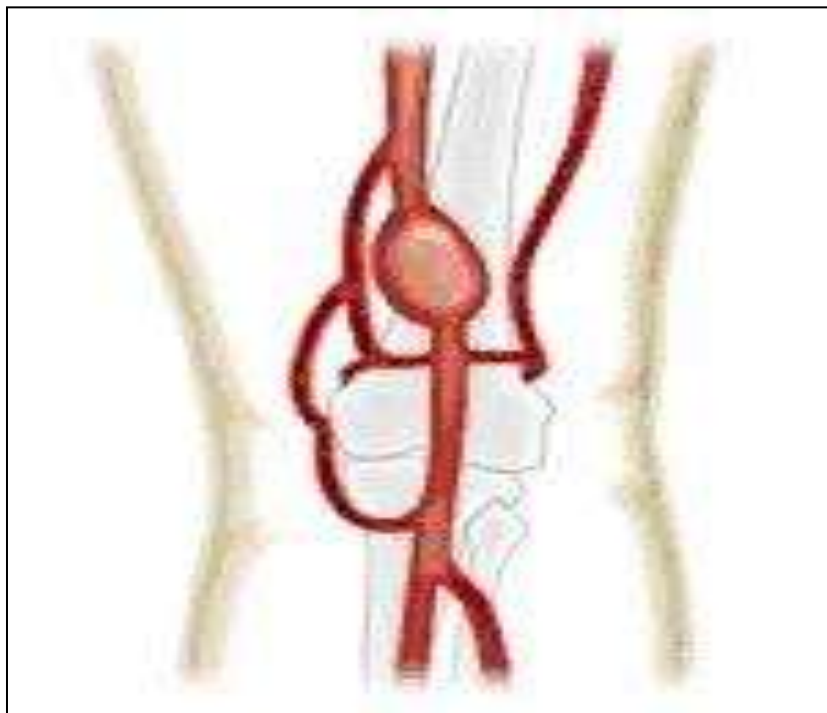


Figure 1.10 Peripheral aneurysm [96].

The causes of a peripheral aneurysm are as follows:

- Smoking
- High blood pressure
- High cholesterol
- Obesity
- A family history of heart or vascular disease

1.4.4. Fusiform Aneurysm

Salsac [78] stated that the areas of higher shear in the internal shear layer activates platelets that along with the blood flow settle in the low-velocity circulation regions. This is a favorable condition for the accumulation of platelets on the aneurysm wall, and the formation of endoluminal thrombus takes place in response to the low and oscillating shear stress.

Once a fusiform aneurysm forms, the shear stress may not be an important factor in controlling the expansion. Remodeling of the artery due to the tensional stress could be the main factor. After the initiation of the remodeling process, the permanent dilatation of the median layer is accompanied by a remodeling of the artery's structure [79]. Progressive changes are not sufficient enough to predict the rate of aneurysm. Along with progressive changes, the change in systolic pressure inside the bulge is also necessary to predict the rate of aneurysm expansion.

1.4.5. Pathogenesis for Arterial Aneurysm

Failure of arteries is a problem similar to that of plastic deformation in structural engineering, where a pipe bulges because of a weakened structure due to oscillatory internal pressure and fails due to fatigue. In the case of human arteries, the progression of disease is very difficult to analyze because an aneurysm is hardly detected until it is diagnosed. These cells, tissues, and sheets of fibers and proteins undergo continuous reformation as a response to the inflammatory processes, infection, degenerative processes, and aging.

Vascular endothelial cells (VECs) are selectively permeable, which allows certain substances to enter them and others not to. Fluid shear forces imparted by the blood flow play an important role in atherosclerosis formation and regulate many VEC functions through a process called mechanotransduction. The current hypothesis suggests that the unidentified mechanosensors on the endothelial cells integrates the external blood flow forces and sends the

feedback to the arteries by appropriate biomechanical responses. Flow shear also regulates the secretion of prostacyclin, a vasodilator which reduces the leukocyte adhesion.

1.4.5.1. The Aging Hypothesis

Many researchers have directed their attention to the aging of arteries. Over the years the diameter of systemic arteries increases and becomes stiffer. Major structural changes occur in the median layer. Over time, the median layer thins out and loses its orderly arrangement of elastin laminas and fibers which get defragmented and unorganized. This is followed by the deposition of collagen. Eventually, the ratio of elastin to collagen decreases, and the vessel loses its elasticity.

1.4.5.2. Vascular Endothelium: Flow Shear-Mediated Initiation Hypothesis

Davies et al. [80] showed that damage is caused to the endothelium layer by unsteady and disturbed flow in a cultured VEC. Chapell et al. [81] showed “correlation between very low shear stress and the loss of permeability of the endothelial cell membrane.” Bao et al. [73] found that endothelial cell expression can be modified by the high temporal and spatial gradients of wall shear stress, which affects the proliferation and migration of cells. During the course of aging, the relative constricted nature of the artery inside the abdominal cavity may lead to the formation of bends, kinks, and other morphological changes, which in turn lead to disturbed flow.

1.4.5.3. Fatigue/ Remodeling Hypothesis

The cyclic stress on arteries could be induced by various risk-causing factors such as hypertension, smoking, and alcohol consumption. This cyclic process may restructure the elastin sheets and fibers. This failure of the elastin structure assembly starts at the apex of the bifurcation where the absence of the muscular layer makes it more vulnerable to permanent

dilatation. The transition to turbulence is a function of the Reynolds number, Strouhal number, and Womersley number.

1.4.6. Progression and Enlargement Rate

It is believed that once an aneurysm forms and the arterial wall undergoes permanent dilatation, it will grow gradually at a steady pace. This is not always the case. Some aneurysms grow very slowly and some grow very rapidly. This is the key area of research for surgeons and physicians: What makes an aneurysm expand at different rates, and what are the factors responsible for it?

1.5. Introduction to Arterial Modeling

A human heart beats around 72 times a minute and supplies blood to the complex vascular system of the entire body. Per cycle, a heart ejects 70 ml of blood at a pressure of 120 mm Hg into the aorta where the mean pressure is 80 mm Hg. The pressure pulse generated by the heart provides oxygenated blood to the entire body via arteries, and veins bring the deoxygenated blood to the heart. In a human life, the heart beats around 3 billion times. Depending on the location and amount of blood required by a particular organ, each artery has its own structural and geometrical properties. Stiffness of an artery is partly controlled by endothelial cells, which send feedback signals to the regulatory part of the artery that controls stiffness. In short, endothelial cells sense the shear stress indirectly by measuring the velocity at the endothelial surface. Therefore, this feedback system works constantly around the clock, can adjust to any cardiac change in a short time, and can regulate normal body functions. In the case of hypertension over a long period of time, the artery thickens to adjust the structural rigidity. In this way, lumen may increase and the artery thickens. In the case of lower hypertension, the artery shrinks and the lumen decreases in size. During the human lifetime, arteries undergo many

regenerative changes and remodel continuously to maintain synergy and function of the system, and to withstand cyclic-wall stresses. In certain cases, however, the artery weakens due to several reasons, like aging and complex hemodynamics, and as a result forms an aneurysm.

1.6. Two Theories for Aneurysm Progression

Current research and knowledge in the field of aneurysms restricts this study to two basic theories explaining how an aneurysm forms and progresses:

- High blood flow effect
- Low blood flow effect

High Blood Flow Effect

An increase in wall shear stress damages the endothelial layer and the healing of the artery starts [82]. Due to an increase in the shear stress index, the production (expression) of nitrogen oxide (NO) increases. This expression can cause a lower, non-physiological arterial process by scarcity and apoptosis of the smooth muscle cells [83, 84]. This disturbs the blood pressure forces and internal wall stresses. When the magnitude of blood pressure forces goes beyond the magnitude of internal wall stresses, the artery starts bulging until both forces are in equilibrium.

Low Blood Flow Effect

Low blood flow or stagnant blood flow causes a lower expression of NO, which is usually expressed by an increase in WSS. This abnormality aggregates blood cells. Also, platelets and leukocytes accumulate and adhere to the tunica intima [85, 86]. This degenerative process damages the intimal layer by the penetration of white blood cells and fibrin in the tunica intima [87, 88]. This leads to the formation of an aneurysm at the low WSS site.

1.7. Difficulties in Modeling Blood Flow

Arteries differ considerably in size. No two humans have exactly same size and shape of arteries. Smaller arteries are more rigid compared to larger arteries. Due to their large deformations, larger arteries can store and release elastic energy, making the blood flow more regular than if they were rigid. Important parameters taken into consideration are pressure, velocity, and displacement; no consideration has been given to chemical interaction of the arterial wall and contents of the blood. The difficulties faced in modeling blood flow are as follows:

- The geometry is very complex. Moreover, the shape of the artery changes during some body movements.
- The fluid is in constant interaction with the vessel wall. Moreover, the shape of the artery is not constant throughout. Larger arteries vary by 10 percent.
- The blood flow is not steady throughout and is transient in nature, i.e., during systole, the blood is ejected out of the heart, and during diastole, the heart contracts and no blood flows out of the heart. For this reason, pulsatility and time are taken into consideration.
- Time scale is one of the prime factors in modeling blood flow. During regular work, sleep, and exercise, the cardiac cycle changes the blood-flow pattern (measured in years). With the growth of the humans body, arteries also grow. This may lead to the formation of plaque and stiffening of arteries, all of which change the geometry and thus the flow.

1.8. Fluid Mechanics

Womersley Number

The Reynolds number range varies in different vessels due to the different diameter. It ranges from 1 in small arterioles to 4,000 in a large artery. The Womersley, or Wilzig, parameter is also an important non-dimensional number, represented by

$$\alpha = R\sqrt{\frac{\omega}{\nu}} \quad (1.1)$$

where

α = Womersley number

R = tube radius

ω = angular frequency

ν = kinematic viscosity

The variable α can be treated as a ratio of inertial forces to viscous forces. It can be observed that when α is low, viscous forces dominate, and vice versa. When viscous forces dominate, the velocity profiles are parabolic in shape, and the centerline velocity periodically oscillates in phase with a driving pressure gradient.

Shear Stress

Shear stress is represented by

$$\tau_r = \mu \frac{du}{dr} \quad (1.2)$$

where

μ = dynamic viscosity

u = velocity in x direction

r = direction along y axis away from boundary

Shear stress for the straight tube is given by

$$\tau = \frac{32 \times \mu \times Q}{\pi \times D^3} \quad (1.3)$$

where

Q = volumetric flow rate

D = diameter of the tube

In cases where the lumen is not circular or irregular or blood flow may be highly skewed at the branched points, shear stress varies widely for pulsatile flow. It is very difficult to measure velocity very close to the wall. However, it is possible to measure steady and unidirectional flow by measuring heat transfer between two adjacent cells that are embedded in the wall. Glagov et al. [46] stated that arteries adapt to maintain a wall shear stress of 15 Dyne/cm². Thus, the shear stress modulates the reflex or adaptive response to maintain the proper shear stress by intimal thickening or stiffening of the arteries.

Hoop Stress

From a structural point of view, the transmural force acting on arteries plays a major role. Arteries have a mean pressure of 100 mm Hg, which keeps the arteries in a circular shape. The veins have a pressure of 10 mm Hg. The hoop stresses are circumferential forces that withstand distension forces. Hoop stresses can be shown by Laplace's Law as

$$\sigma = \frac{P \times R}{t} \quad (1.4)$$

where

P = pressure

R = radius

t = wall thickness

Endothelial cells are affected by shear stress, whereas smooth muscle cells are affected by hoop stresses. Hoop stresses regulate the wall thickness to balance blood pressure.

1.9. Damages and Adaptation of Blood Vessels

The human body is constantly in a reformation and regenerative process. Damaged cells and tissues are repaired at the site of injury. The following processes describe the regenerative process in a human body.

1.9.1. Biological Response to Hemodynamic Process

The inner layer of the vascular system containing endothelial cells and the outer layer containing smooth muscle cells are subjected to adverse stress conditions during their functioning time period. During this period, cells are damaged and replaced to maintain normal functioning of the circulatory system. The human body has a responsive system, which immediately acts in response to even minor changes from normal functioning. To maintain smooth functioning of the vascular system, arteries respond to minute-by-minute changes. This response is called adaptation.

1.9.2. Hemostasis

Hemostasis is the ability of living things to maintain relatively stable, overall internal conditions while experiencing constant metabolic changes. When an artery is damaged through trauma, it must heal in order for the blood to flow smoothly through it. Hemostasis must occur within a very small time scale of milliseconds. When an artery is injured, blood squirts out, leaving collagen and tissue factor (a protein-phospholipid mixture) exposed. Hemostasis is initiated by the blood platelets. This process is shear dependent.

CHAPTER 2
DESCRIPTION OF MODELS

2.1. Tapered Artery

A cross section of a tapered stenosed artery is shown in Figure 2.1, and a schematic diagram of a stenosed tapered artery used in this investigation is shown in Figure 2.2.

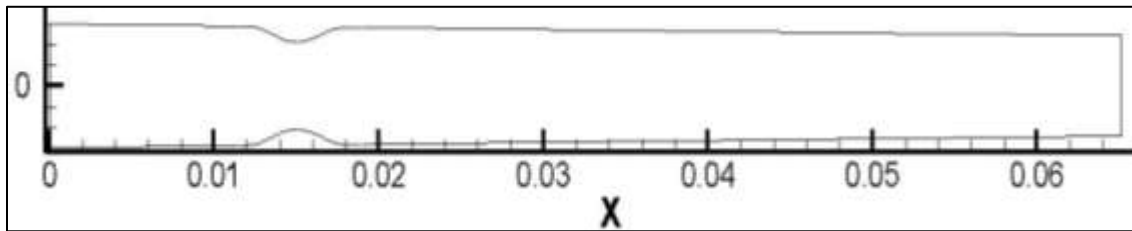


Figure 2.1 Cross section of tapered stenosed artery.

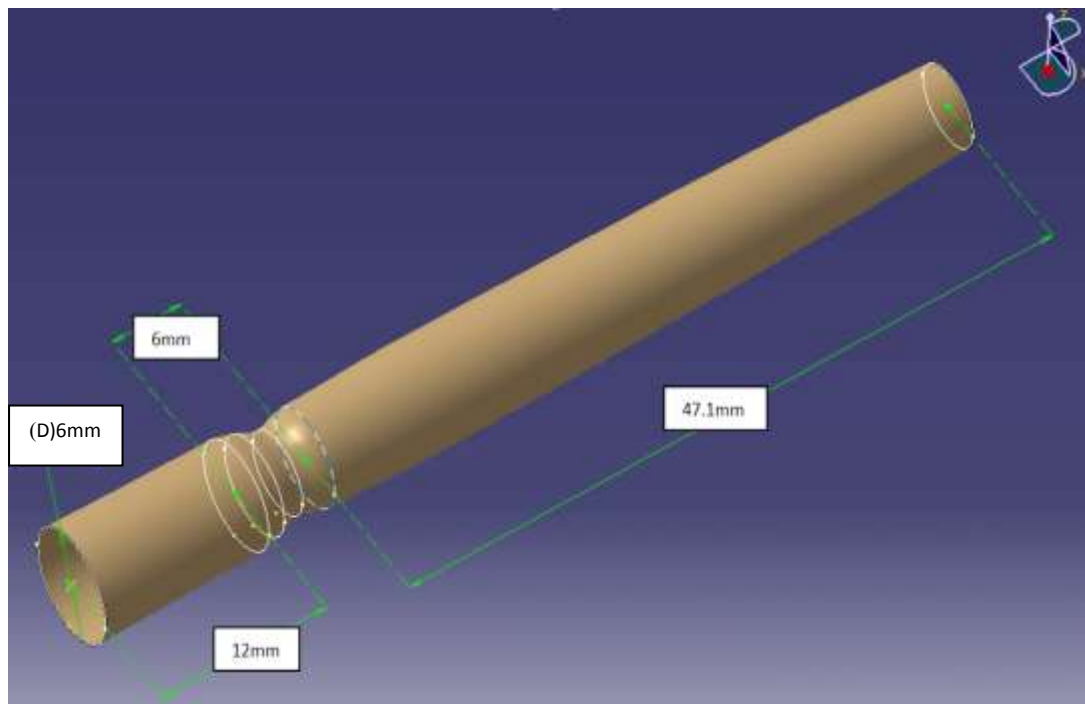


Figure 2.2 Schematic diagram of tapered stenosed artery with 25 percent diameter reduction.

The stenosed tapered artery is a three-dimensional axisymmetric tube with a 25 percent diameter reduction for κ - ω and κ - ω pulsatile cases. The geometry used for pulsatile validation

has a 50 percent reduction in diameter. Total length of the tube is 65.1 mm. The radius of the inlet and outlet is 3 mm and 2.43 mm, and is constantly reduced along the x-axis. In the current case, stenosis is located 15 mm away from the inlet, which is five times the radius. The exit length is 50.1 mm from the stenosis. Table 2.1 shows the geometrical aspects of the model.

TABLE 2.1

GEOMETRICAL ASPECTS OF STEADY AND PULSATILE CASE FLOW

	M1 (Steady Flow)	M2 (Pulsatile Flow)
h/R_0	1/4	1/2
X_0/R_0	1	1
	0.5°	0.5°

M1 represents the model used in the current simulation, and M2 represents the model used for pulsatile validation. Small h represents the height of the stenosis, and R_0 represents the inlet radius. X_0 represents the length of the stenosed region. Small d represents the distance between the inlet and the stenosis. The artery is tapered at a 0.5° angle. Equations of the tapered artery and abdominal aortic aneurysm used to construct the artery are provided in equations (2.1) and (2.2):

$$R(x) = \left\{ R_0 - (x+d) \tan \theta - \frac{h \cos \theta}{2} \left[1 + \cos \frac{\pi x}{x_0} \right] \right\} \text{ for } |x| \leq x_0 \quad (2.1)$$

$$R(x) = R_0 - (x+d) \tan \theta \text{ for } |x| > x_0 \quad (2.2)$$

2.2. Abdominal Aortic Aneurysm

Figure 2.3 shows a cross section of an abdominal aortic aneurysm, and Figure 2.4 shows the schematic diagram of an AAA. Dimensions of each are shown in the figures. The inlet and outlet lengths are both 32 mm, and the inlet and outlet diameters are both 1.0 mm. The geometry of the aneurysm is not tapered as in the previous case. The artery is bulged at the center. The

bulged portion has a maximum diameter of 2.5 mm and a minimum diameter of 1.0 mm. The length of the bulged portion is 4.0 mm.

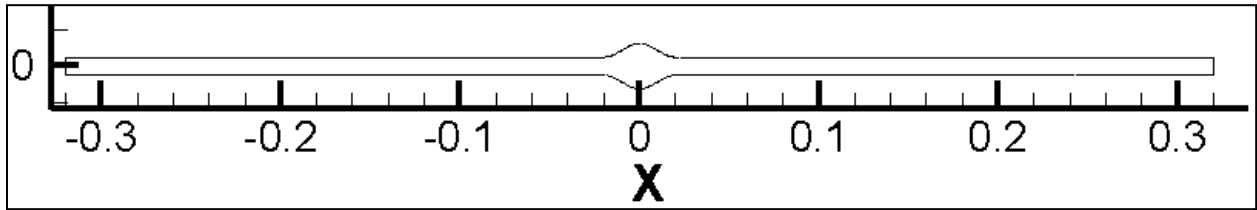


Figure 2.3 Cross section of abdominal aortic aneurysm.

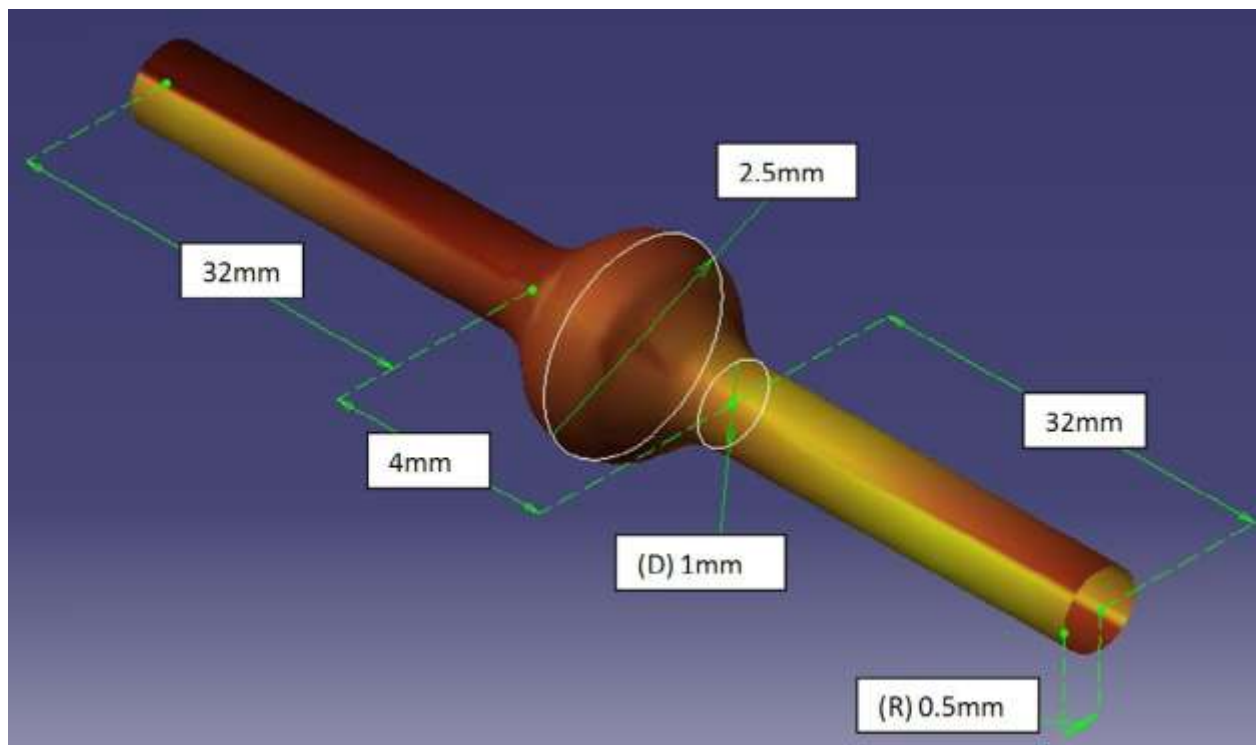


Figure 2.4 Schematic diagram of abdominal aortic aneurysm (not scaled).

The AAA model is taken from Taylor and Yamaguchi [89] who simulated a model A with the same parameters except the inlet and exit lengths. The diameters of both the inlet and outlet are the same. The maximum and minimum diameters of the aneurysm are also the same as in the model A by Taylor and Yamaguchi [89]. Moreover, the model A had an asymmetric aneurysm, whereas in the current simulation, the aneurysm was symmetric. In real cases, aneurysms are

asymmetric. The mathematical equation for the bulged portion of the aneurysm is given in equation (2.3).

$$R(x) = \left\{ R_0 - x + d + \frac{h \cos \theta}{2} \left[1 + \cos \frac{\pi x}{x_0} \right] \right\} \quad (2.3)$$

CHAPTER 3

GRID GENERATION

3.1 Tapered Stenosed Artery

For this investigation, the geometry and grid were generated in GAMBIT 2.4.6. FLUENT 6.3.26 was used as the solver since previous researchers have used the same processor for simulation. Ryval et al. [56] also used FLUENT 6.3.26 for simulating the straight stenosed artery geometry. TECPLOT 360 was used for post-processing. A geometry with various cells was used for validation purposes, and results were almost the same. The tapered artery had 1,436,400 grid points. The grid was denser at the boundary region and coarser at the inner region towards the center of the model. The stenosed region had a denser mesh since it was the area that would have maximum shear stress. The walls of the model were considered rigid since atherosclerosis reduces the elastic properties of the arteries and increases stiffness [73].

Rather than using the symmetry condition, 3-D axisymmetric geometry was used to make the case less complicated. The maximum aspect ratio of the grid and skewness of the worst element were 24.0 and 0.4, respectively. Walls of the geometry were more clustered to obtain accurate results for the wall shear stress.

Table 3.1 shows various aspects of the boundary layer mesh for geometry with 25 percent stenosed artery. Figure 3.1 illustrates the three dimensional geometry of the tapered artery with a structured grid. Figures 3.2 and 3.3 illustrate the mesh at the inlet and outlet, respectively, of the tapered geometry. Figure 3.4 shows a magnified view of mesh at the stenosis region with 25 percent diameter reduction. Table 3.2 illustrates the skewness of the grid elements used in the mesh. A mesh with skewness greater than 0.97 is not considered to be a good mesh for simulation.

TABLE 3.1

VARIOUS ASPECTS OF BOUNDARY LAYER MESH FOR GEOMETRY WITH 25 PERCENT STENOSED ARTERY

Algorithm	Aspect Ratio (First–Last)
First Percent (A/W)	1
Growth Factor (b/a)	1.26
Rows	20
Last Percentage (c/w)	80.731
Element Type for Inner Region Closer to Radius	Tri and Pave

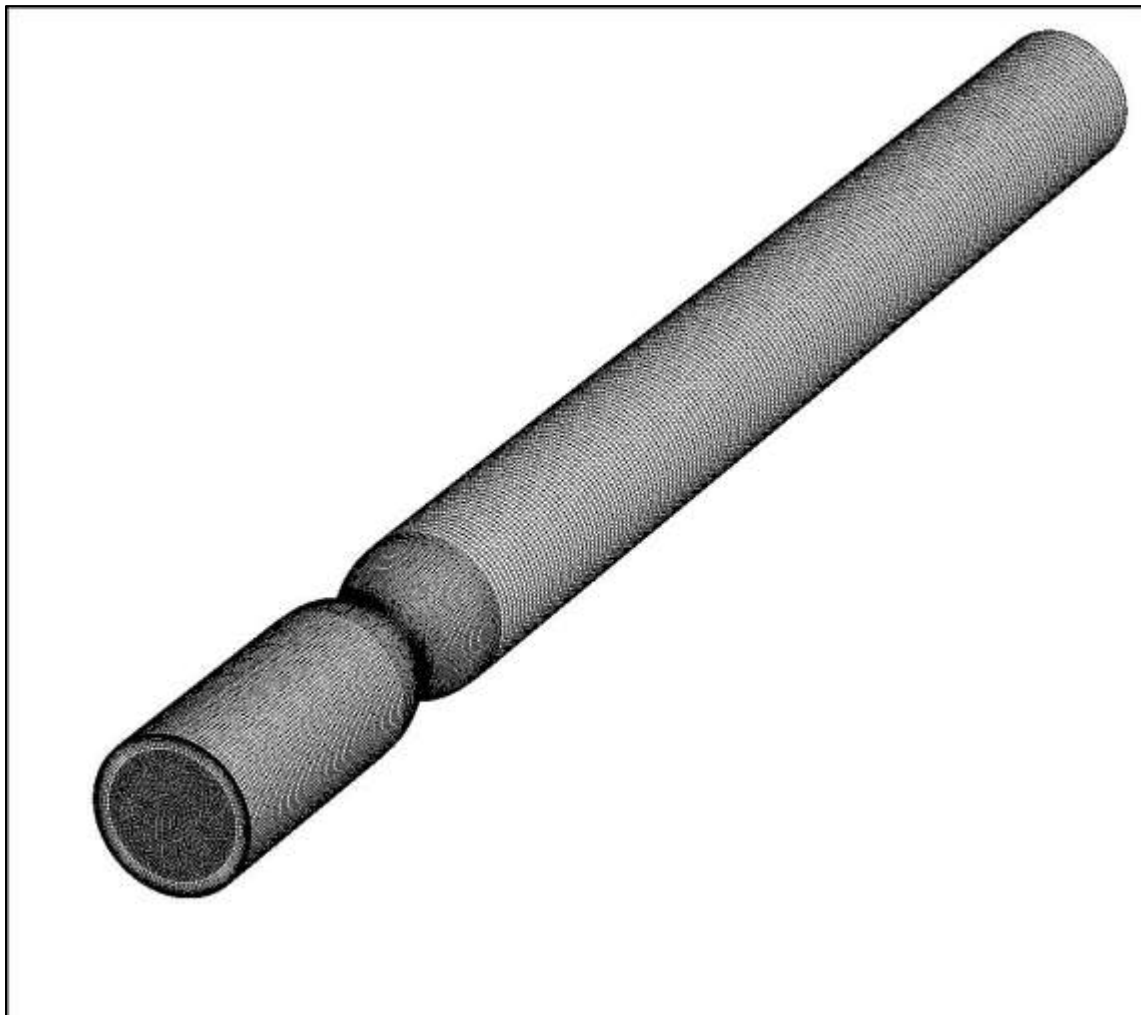


Figure 3.1 Three-dimensional grid of tapered artery with 25 percent diameter reduction.

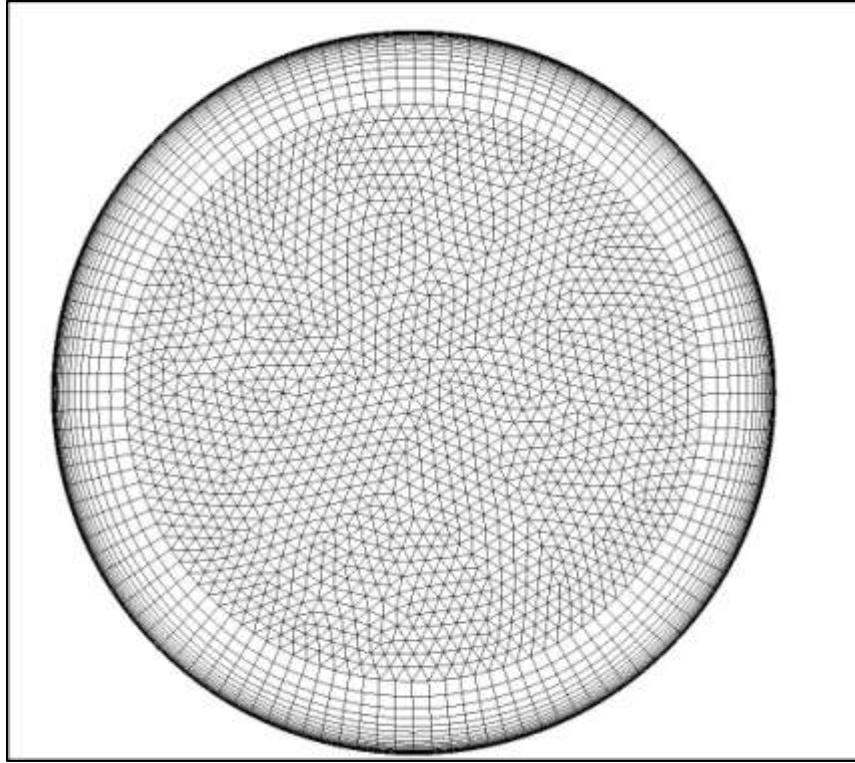


Figure 3.2 Mesh at inlet of geometry with 25 percent diameter reduction.

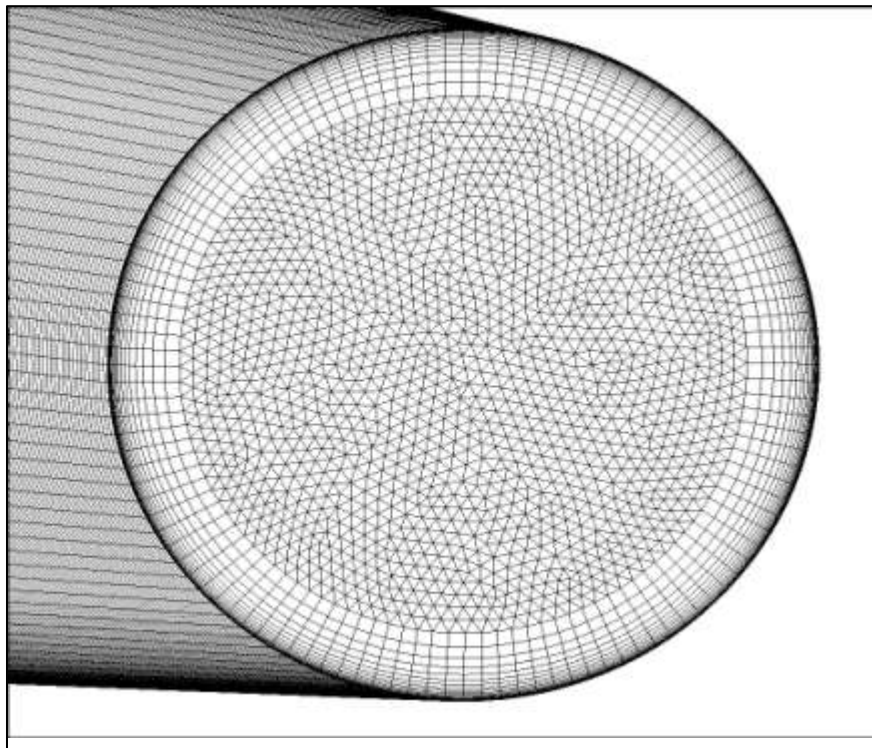


Figure 3.3 Mesh at outlet of geometry with 25 percent diameter reduction.

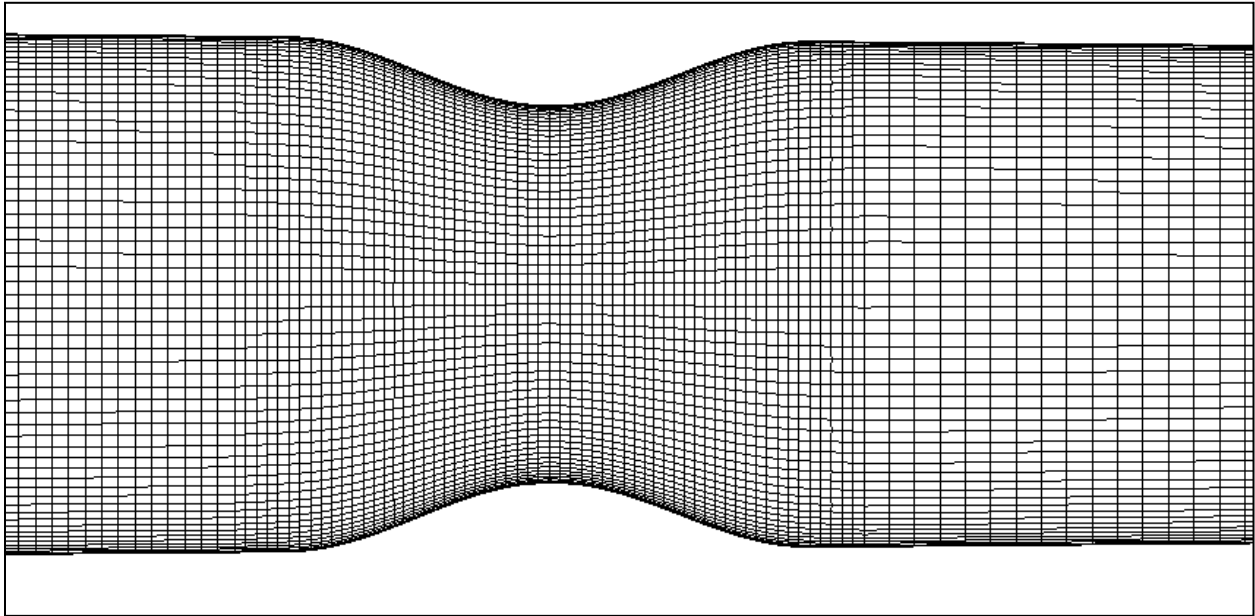


Figure 3.4 Magnified view of mesh at stenosis region with 25 percent diameter reduction.

TABLE 3.2

SKEWNESS VALUE OF GRID ELEMENTS

From Value	To Value	Counting Range 1,436,400	Percent of Total Elements
0.0	0.1	1,075,257	74.86
0.1	0.2	293,935	20.46
0.2	0.3	63,028	4.39
0.3	0.4	4,180	0.29
0.4	1.0	0	0

3.2 Abdominal Aortic Aneurysm

Figure 3.5 shows the three-dimensional grid of an abdominal aortic aneurysm. Boundary layer meshing was used at the wall to capture the wall shear stress accurately. Figure 3.6 shows the magnified view of the bulged section, which has a highly dense grid. Boundary layer meshing can be seen in Figure 3.7. Mesh was also denser at the center of the artery to capture the

oscillating vortex in the bulged portion. Boundary layer information is provided in Table 3.3, and skewness values of grid elements for the AAA can be seen in Table 3.4.

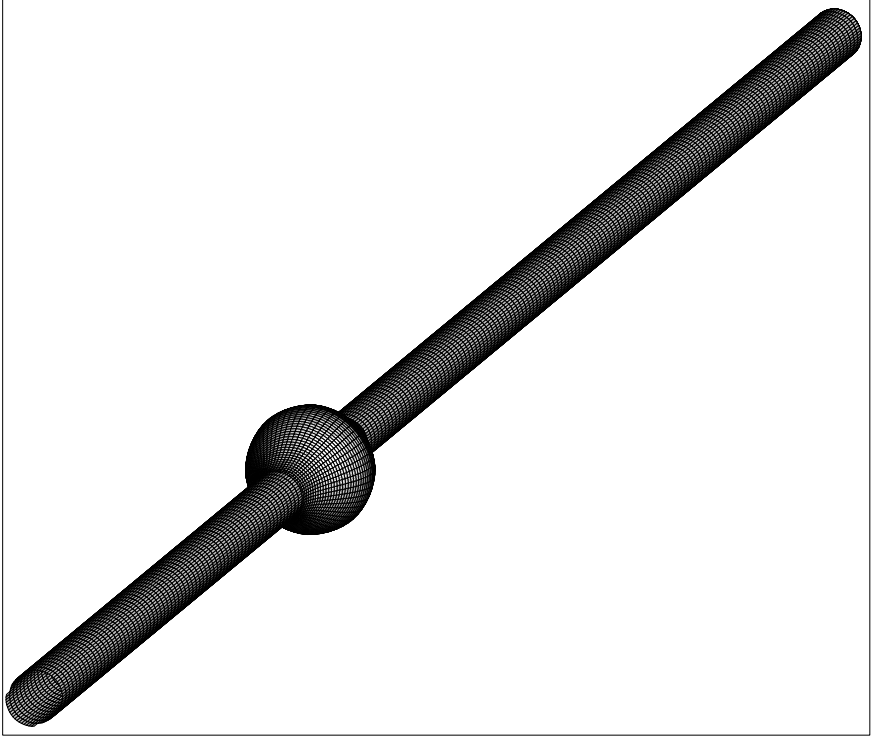


Figure 3.5 Three-dimensional grid of abdominal aortic aneurysm.

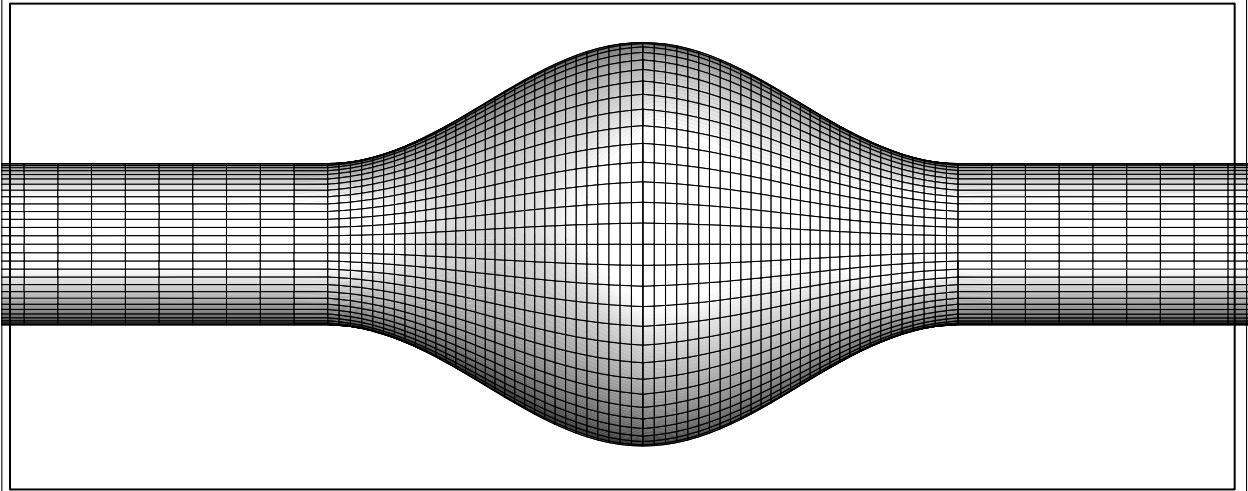


Figure 3.6 Magnified view of abdominal aortic aneurysm.

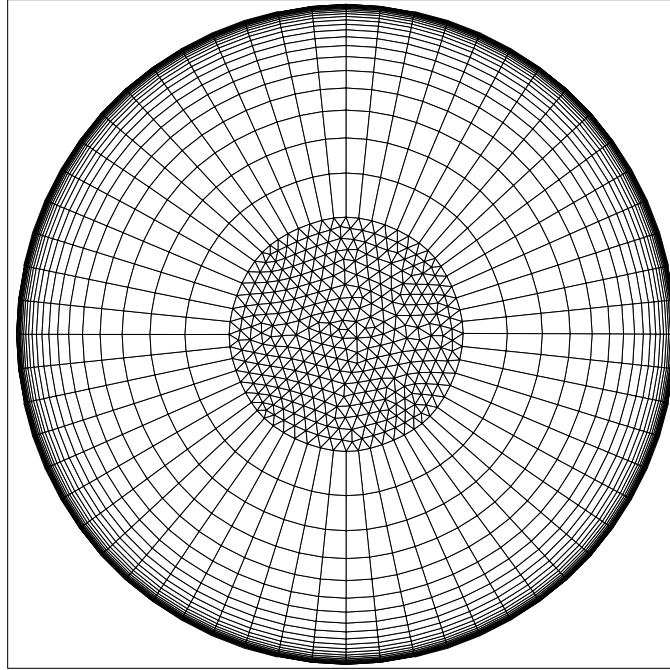


Figure 3.7 Inlet and outlet mesh of abdominal aortic aneurysm.

TABLE 3.3

VARIOUS ASPECTS OF BOUNDARY LAYER MESH FOR AAA

Algorithm	Aspect Ratio (First–Last)
First Percent (a/w)	1
Growth Factor (b/a)	1.26
Rows	22
Last Percentage (c/w)	128.169
Element Type for Inner Region Closer to Radius	Tri and Pave

TABLE 3.4

SKEWNESS VALUE OF THE GRID ELEMENTS FOR AAA

From Value	To Value	Counting Range 2,667,600	Percent of Total Elements
0.0	0.1	2,053,399	76.98
0.1	0.2	430,727	16.15
0.2	0.3	152,412	5.71
0.3	0.4	31,062	1.16
0.4	1.0	0	0.0

CHAPTER 4

SOLUTION PROCEDURE

4.1 Governing Equations

The current work illustrates the application of Wilcox's κ - ω model. Blood is assumed to be incompressible and Newtonian. In larger arteries, such as the abdominal aorta, blood behaves as Newtonian, and in smaller arteries it behaves as non-Newtonian, which is consistent with the experimental work done by Ahmed and Giddens in 1983 [63, 64]. Phase averaged (commonly called ensemble average) conservation of mass, as shown in equation (4.1), and conservation of momentum, as shown in equation (4.2), are required to predict the pulsatile flow in a stenosed tapered artery of the current that was investigated.

$$\frac{\partial u_i}{\partial x_i} = 0 \quad (4.1)$$

$$\rho \frac{\partial(u_i)}{\partial t} + \rho(u_j) \frac{\partial(u_i)}{\partial(u_j)} = -\frac{\partial(p)}{\partial x_i} + \frac{\partial}{\partial x_j} \left(\mu \left(\frac{\partial(u_i)}{\partial x_j} + \frac{\partial(u_j)}{\partial x_i} \right) - (\rho u_i u_j) \right) \quad (4.2)$$

where (u_i) is the ensemble-averaged velocity, (p) is the ensemble-averaged pressure in the x direction, ρ is density, and μ is the dynamic viscosity. The first term on the left-hand side of equation (4.2) represents unsteady acceleration, and the second term on left-hand side of the unsteady equation represents convective acceleration. On the right-hand side, the first term represents pressure gradient, the second term represents diffusion due to viscosity, and the third term represents body forces, such as Reynolds stresses, which represent the effect of turbulence on balance momentum.

Phase-averaging is the division of the ensemble sum of a particular quantity divided by phase averaging of a flow variable. Equations (4.1) and (4.2) are phase-averaged rather than

time-averaged because for periodic flow, the reported velocities and quantities are obtained from phase-averaging. It is a well-known fact that for steady-flow conditions, phase-averaging and time-averaging quantities are equal.

4.2 Turbulence Model

The κ - ω model has two transport variables. The first is phase-averaged turbulent kinetic energy, and the second is turbulent eddy viscosity. In equation (4.2), the last term, called Reynolds stresses, on the right-hand side, introduces the unknowns. Unknowns introduced in equation (4.2) raise an additional requirement of using a turbulent model to complete the equation. The Boussinesq relation for incompressible flow, shown in equation (4.3) was used to approximate the incompressible flow.

$$-(\rho u_i u_j) = \mu_t \left(\frac{\partial(u_i)}{\partial(x_j)} + \frac{\partial(u_j)}{\partial(x_i)} \right) - \frac{2}{3} \rho(k) \delta_{ij} \quad (4.3)$$

From equation (4.3), it can be known that the Reynolds stress term is directly proportional to the mean strain rate of flow, and the turbulent eddy viscosity is a constant of proportionality. As a result, shear stress can be divided into viscous stress and turbulent shear stress. The Boussinesq assumption is a base for the two-equation κ - ω . The κ - ω model is given by equations (4.4) to (4.20). The turbulent kinetic energy and ensemble phase-averaged specific dissipation rate are given by

$$\rho \frac{\partial(\kappa)}{\partial(t)} + \rho(U_j) \frac{\partial(\kappa)}{\partial x_j} = \frac{\partial}{\partial x_j} ((\mu + \sigma^* \mu_T) \frac{\partial(\kappa)}{\partial x_j}) - (\rho u_i u_j) \frac{\partial(U_i)}{\partial x_j} + \rho \beta^*(\kappa)(\omega) \quad (4.4)$$

and

$$\rho \frac{\partial(\omega)}{\partial(t)} + \rho(U_j) \frac{\partial(\omega)}{\partial x_j} = \frac{\partial}{\partial x_j} ((\mu + \sigma \mu_T) \frac{\partial(\omega)}{\partial x_j}) - \alpha \frac{(\omega)}{(\kappa)} (\rho u_i u_j) \frac{\partial(U_i)}{\partial x_j} + \rho \beta(\omega^2) \quad (4.5)$$

The eddy viscosity is determined by

$$\mu_t = \rho \frac{(\kappa)}{(\omega)} \quad (4.6)$$

The other relations are

$$\varepsilon = \beta^* \omega \kappa \quad (4.7)$$

$$l = \frac{\kappa^{1/2}}{\omega} \quad (4.8)$$

where

$$\alpha = 1$$

$$\beta = 0.072$$

$$\sigma = 0.5$$

$$\sigma^* = 0.5$$

$$\beta^* = 0.072$$

One or more variants of κ - ω are available. One of them is the transitional κ - ω model. In this model, flow transition is possible at the desired point of interest with some modifications. Since the flow is a low-Re number, a correction factor α^* was included in the turbulent eddy viscosity, which is calculated from

$$\alpha^* = \alpha_\infty^* \left(\frac{\alpha_\infty^* + \frac{\text{Re}_t}{R_k}}{1 + \frac{\text{Re}_t}{R_k}} \right), \quad (4.9)$$

where Re_t is the turbulent Reynolds number defined by

$$\text{Re}_t = \frac{\rho \kappa}{\mu \omega}, \quad (4.10)$$

$$R_k = 6 \quad (4.11)$$

$$\alpha_0^* = \frac{\beta_i}{3}, \quad (4.12)$$

$$\beta_i = 0.072, \quad (4.13)$$

$$\alpha_\infty^* = 1 \quad (4.14)$$

$$\mu_t = \alpha^* \rho \frac{\kappa}{\omega}, \quad (4.15)$$

The low-Re correction factor varies from 0 to 1 and influences the turbulent flow. From equations (4.9) to (4.15) it can be seen that a low-Re correction factor is very small in the case of laminar flow since a turbulent Reynolds number will be close to zero. At a low-Re, the eddy viscosity effect reaches nearly zero, and as a result the whole term is nearly zero. But in the case of turbulent flow, the turbulent Reynolds number will have a value, which is close to unity, and the model will behave as the κ - ω model.

Wilcox derived both the constants and correction factors. He made a Blasius transformation and applied through momentum and turbulence equations over the flat plate. He then observed when the flow transition occurred from laminar to turbulent from assumed constants κ and ω at the solid boundaries. The transport equations of κ and ω remain the same as in equations (4.4) and (4.5) but change after adding a low-Re correction factor to modify some coefficients and eddy viscosity to meet the local flow structure. The equation becomes

$$\beta^* = \beta_\infty^* \left(\frac{\frac{4}{15} + \left(\frac{\text{Re}_t}{R_\beta} \right)^4}{1 + \left(\frac{\text{Re}_t}{R_\beta} \right)^4} \right) \quad (4.16)$$

where

$$R_\beta = 8$$

$$\beta_{\infty}^* = 0.09$$

After modification, the equation becomes

$$\alpha = \frac{\alpha_{\infty}}{\alpha^*} \left(\frac{\alpha_0 + \left(\frac{Re_t}{R_{\omega}} \right)^4}{1 + \left(\frac{Re_t}{R_{\omega}} \right)^4} \right) \quad (4.17)$$

where

$$R_{\omega} = 2.95$$

$$\alpha_{\infty} = 0.52$$

$$\alpha_0 = 1/9$$

Various parameters have to be defined in a turbulent case. FLUENT has various options for defining turbulent parameters from which to choose. Turbulent length scale (l) and hydraulic diameter (D_H) were chosen. The turbulent length scale represents large energy and is given by

$$l = 0.07L \quad (4.18)$$

where $L = D_H$ for fully developed flow in circular pipes (where D_H = hydraulic diameter), and the constant value 0.07 is calculated in FLUENT 2001 from the maximum length in a fully developed pipe flow. The value of turbulent kinetic energy is calculated from FLUENT 2001 as

$$\kappa = \frac{3}{2} U_{avg} I^2 \quad (4.19)$$

where I is the turbulent intensity.

The rate of specific dissipation is given by

$$\omega = \frac{\kappa^{\frac{1}{2}}}{C_{\mu}^{1/4} l} \quad (4.20)$$

In equation (4.20), κ is calculated from equation (4.19) and an empirical constant $C_\mu = 0.09$.

4.3 Boundary Conditions

Boundary conditions are the most important aspect, along with other procedures, to obtain the correct results. If boundary conditions are not correct, then the solution does not yield the correct results. The boundary condition at the outlet was pressure outflow, and at the wall surfaces, the no-slip boundary conditions were prescribed. In order to reduce the length of the geometry, the grid size was decreased. And to decrease the computational time, the boundary condition at the inlet was made to be a parabolic (Poiseuille) velocity profile for the steady case. For this velocity profile, a user-defined function (UDF) was coupled in FLUENT 6.3.26 to give the correct results. In this thesis, the UDF was in C programming and chosen because it allowed customization of FLUENT to the needs herein. In the current case, UDF found the radius of each node, calculated the velocity, depending upon the radius, and gave a fully developed parabolic velocity profile at the inlet. For the unsteady case, another UDF with the same logic was used. UDFs for the steady and pulsatile cases can be found in Appendix A and B, respectively. The velocity profile was unsteady at the inlet. The period of oscillation was $T = 0.4$ sec. The Womersley number is a ratio of inertial effects to viscous effects, which is 1.01 and 6.1 in the pulsatile simulations of the abdominal aortic aneurysm and stenosed tapered artery, respectively. The maximum velocity is given as

$$U_0(t) = 0.25 \left[1 + \sin \left(2\pi \frac{t}{T} \right) \right] \quad (4.21)$$

4.4 Physical Properties

4.4.1 Density

The density of blood is considered to be $1,056 \text{ kg/m}^3$. In reality, blood is a multiphase solution consisting of proteins, lipoproteins, plasma, and red and white blood cells. For this research, the density of blood was considered to be constant.

4.4.2 Viscosity (Newtonian)

The viscosity of blood is not constant throughout the human cardiovascular system. It has been shown experimentally that blood shows shear thinning properties in arterioles, which have higher shear stress than large arteries such as the aorta. Many researchers have used different blood viscosity models such as the Carreau-Yasuda model. For this investigation, neither of the two models were arterioles nor did they exhibit the shear thinning property of blood. As a result, the viscosity of blood was assumed to be constant at 0.004 kg/m.s .

4.5 Discretization Scheme

For steady and unsteady cases of both the tapered stenosed artery and the abdominal aortic aneurysm, a first-order scheme for pressure and first-order upwind scheme were used. For momentum, turbulent kinetic energy and a specific dissipation rate first order upwind scheme were used. Pressure and velocity were coupled through SIMPLEC (Semi-Implicit Method for Pressure-Linked Equation Consistent) scheme.

4.6 Relaxation Parameters

For both models, the default relaxation factors were used.

4.7 Convergence Criteria

In this study, the convergence criteria were set to 10^{-3} .

4.8 Advantages of Original κ - ω Model by Wilcox

- The κ - ω model does not require any special conditions such as wall functions at the solid boundaries, whereas special considerations such as damping functions are required in the κ - ϵ model. This characteristic of κ - ω makes it suitable for internal flows.
- The κ - ω model accurately predicts skin friction and velocity profile at the wall.
- The κ - ω model gives more accurate results than the κ - ϵ model in the logarithmic region of the boundary layer in complex flows, such as with compressibility effects and adverse pressure gradient.

4.9 Disadvantages of κ - ω Model by Wilcox

- The κ - ω model grid must be very dense at the walls to obtain accurate results; consequently, more time is consumed.
- Like κ - ϵ , the κ - ω model fails to calculate the pressure-induced separation. The shear stress temporal only lessens this effect.
- Due to its sensitivity to ω , the κ - ω model fails to give accurate results in wakes and free-shear-layer zones.

CHAPTER 5

VALIDATION AND GRID INDEPENDENCE

5.1 Validation of $\kappa\text{-}\omega$ Steady Case

This investigation mainly focused on the simulation of steady and pulsatile flows through a stenosed tapered artery. It was necessary to validate the results with previous results since the experimental results were available for comparison. Since no experimental results of flow through a tapered artery are available, it was decided to validate results of the straight stenosed artery with 75 percent stenosis as done by Ryval et al. [56]. The model was simulated at $Re = 500$, and the results were compared to the experimental results of Ahmed and Giddens [63, 64]. The radius of the geometry for validation was 0.254 mm, as shown in Figure 5.1.

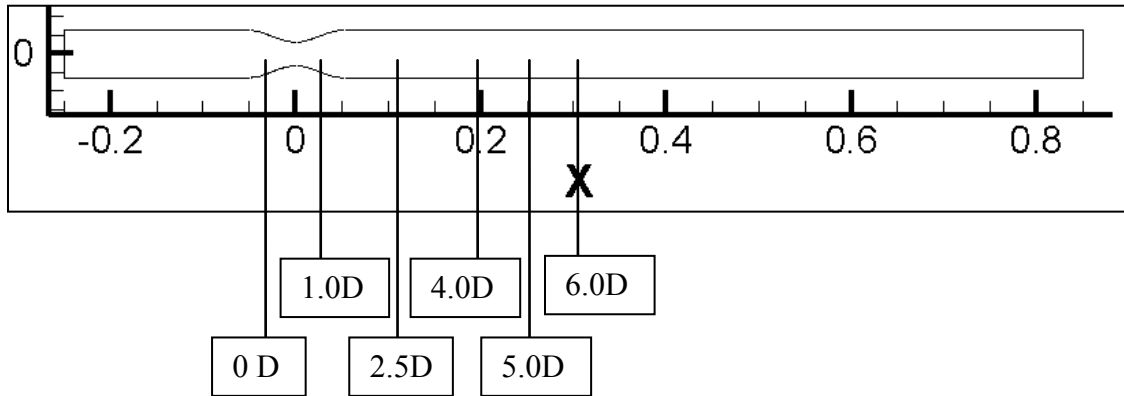


Figure 5.1 Location where X-velocity profiles are compared with experimental results.

Total length of the geometry was 110 mm. Inlet length was 24.492 mm from stenosis, and outlet length was 84.492 mm from stenosis. The length of a stenosis was 1.016 mm. The geometry had 1,425 K grid points. Boundary layer meshing was employed at the wall. The grid was denser at the boundary to capture the velocity profile and shear stress at the wall. In the initial investigation, the velocity profiles at desired locations were not behaving the same as the experimental data. Therefore, the standard $\kappa\text{-}\omega$ model was employed. As shown in Figure 5.1,

slices were cut at six different locations from the center of stenosis: $X = 0 D$, $1 D$, $2.5 D$, $4.0 D$, $5.0 D$, and $6.0 D$. For validation of the grid, five different models with different grids were simulated. The model had 300 K, 658 K, 1000 K, 1250 K, and 1425 K grid points. Figures 5.2 to 5.7 represent the X-velocity profiles for a flow in a straight stenosed artery with 75 percent stenosis at $Re = 500$. Results are shown at $X = 0.0 D$, $1.0 D$, $2.5 D$, $4.0 D$, $5.0 D$, and $6.0 D$ from the stenosis. The model with 300 K and 658 K grid points had some discrepancies near the center, as can be seen in Figures 5.4 to 5.7. The continuity of the velocity profile was not maintained near the center. To solve this problem, models with 1000 K, 1250 K, and 1425 K grid points were employed, and the results were compared to obtain the correct results. These results were in close proximity with the experimental results.

The horizontal axis represents velocity normalized by V_m . The vertical axis represents the radius normalized by the local radius. Figures 5.3 to 5.6 illustrate that as the distance from stenosis increases, the velocity profiles of the grid with 300 K and 658 K grid points diverge more from the experimental results at the center of the tube.

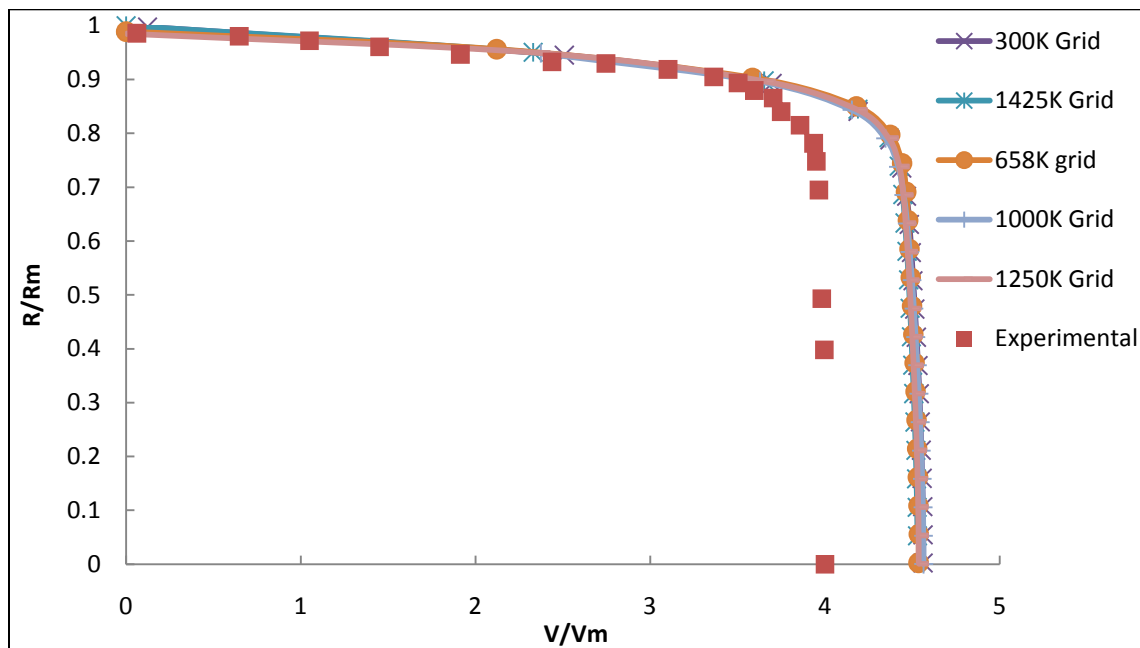


Figure 5.2 X-velocity profile for $X = 0 D$.

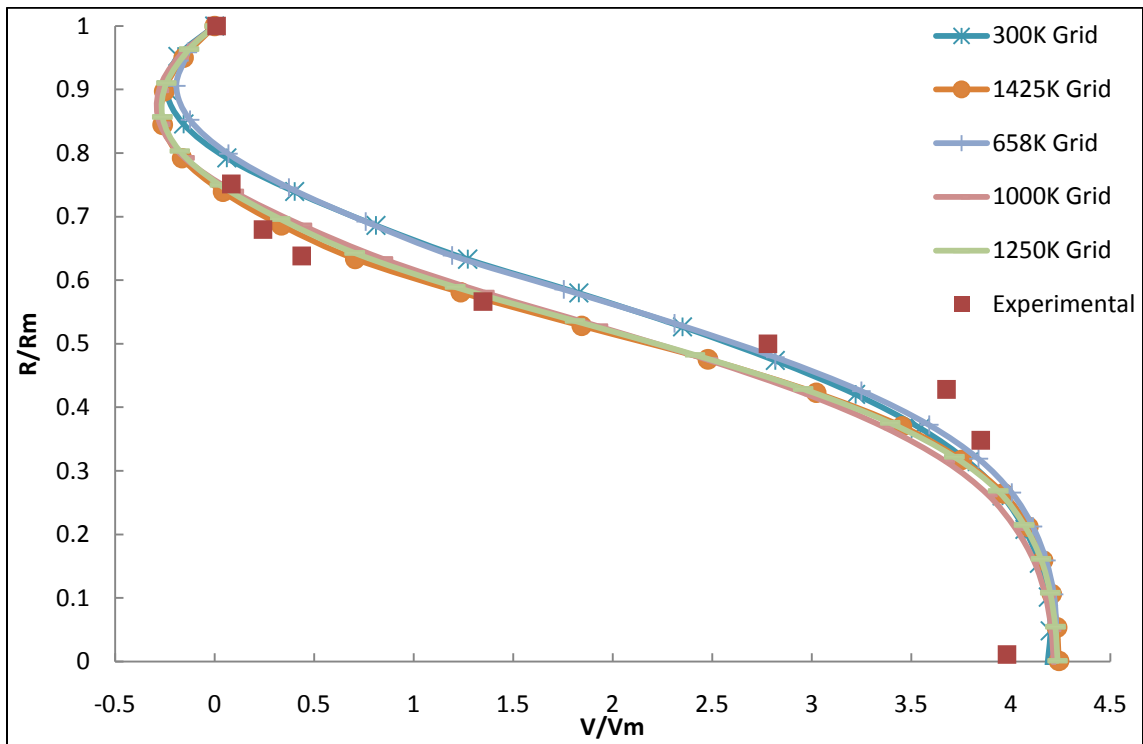


Figure 5.3 X-velocity profile for $X = 1.0 D$.

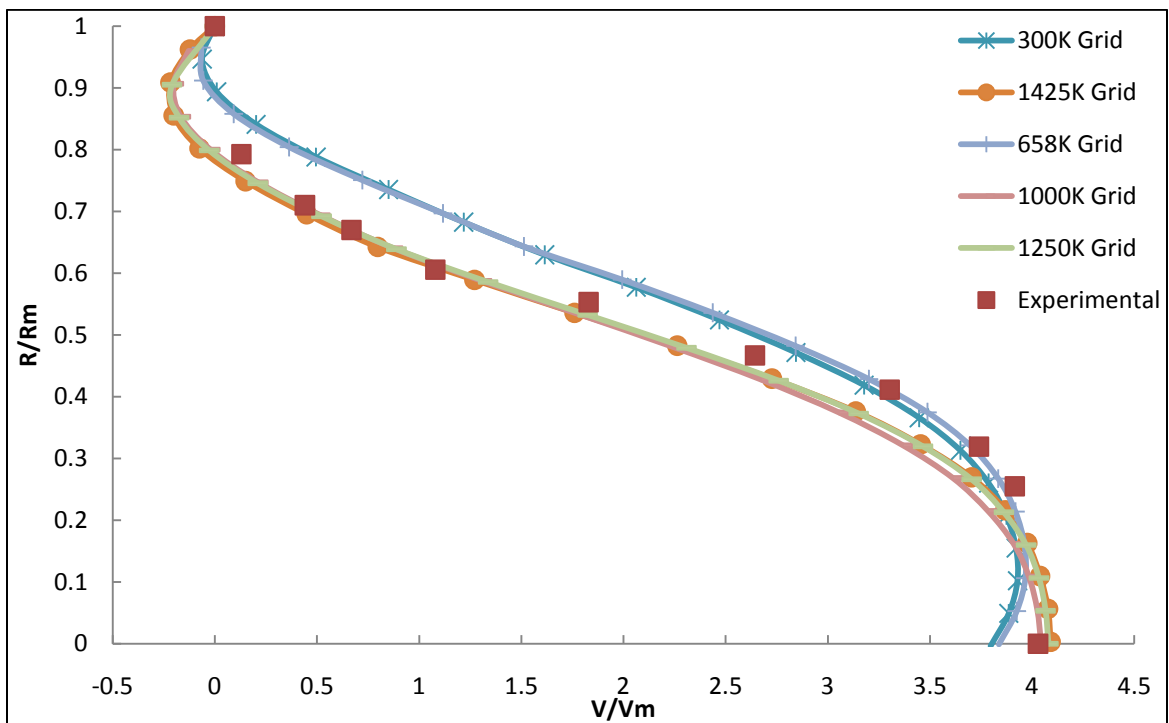


Figure 5.4 X-velocity profile for $X = 2.5 D$.

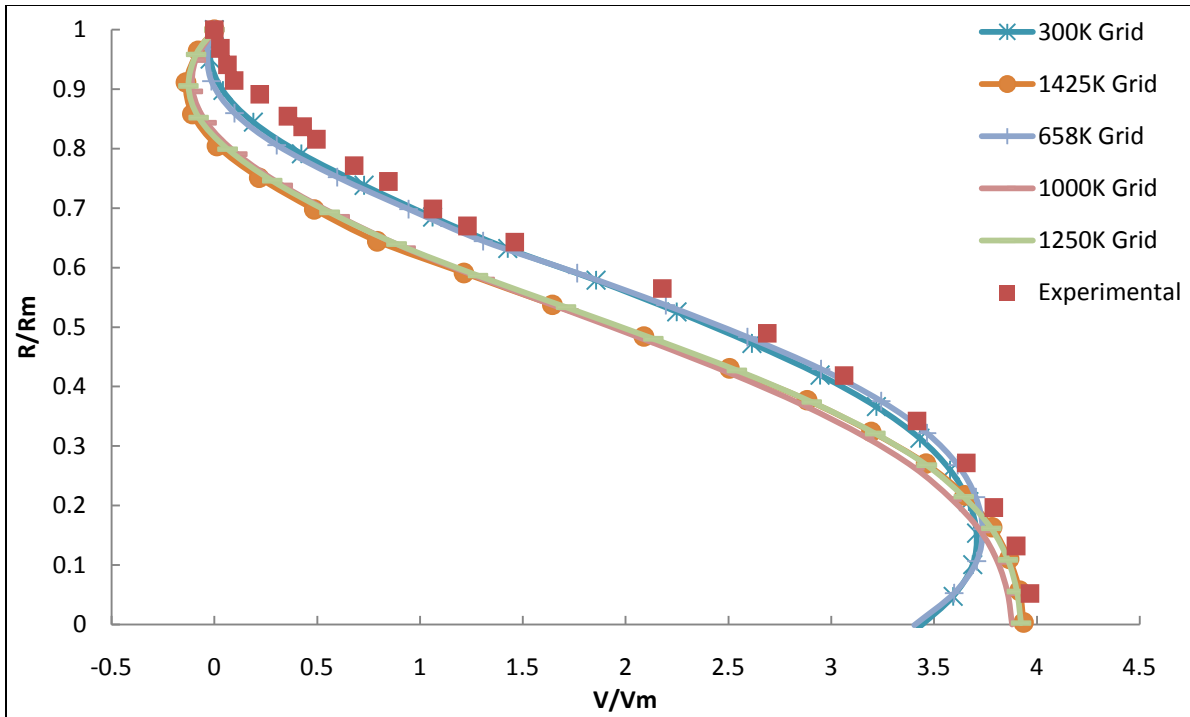


Figure 5.5 X-velocity profile for $X = 4.0 D$.

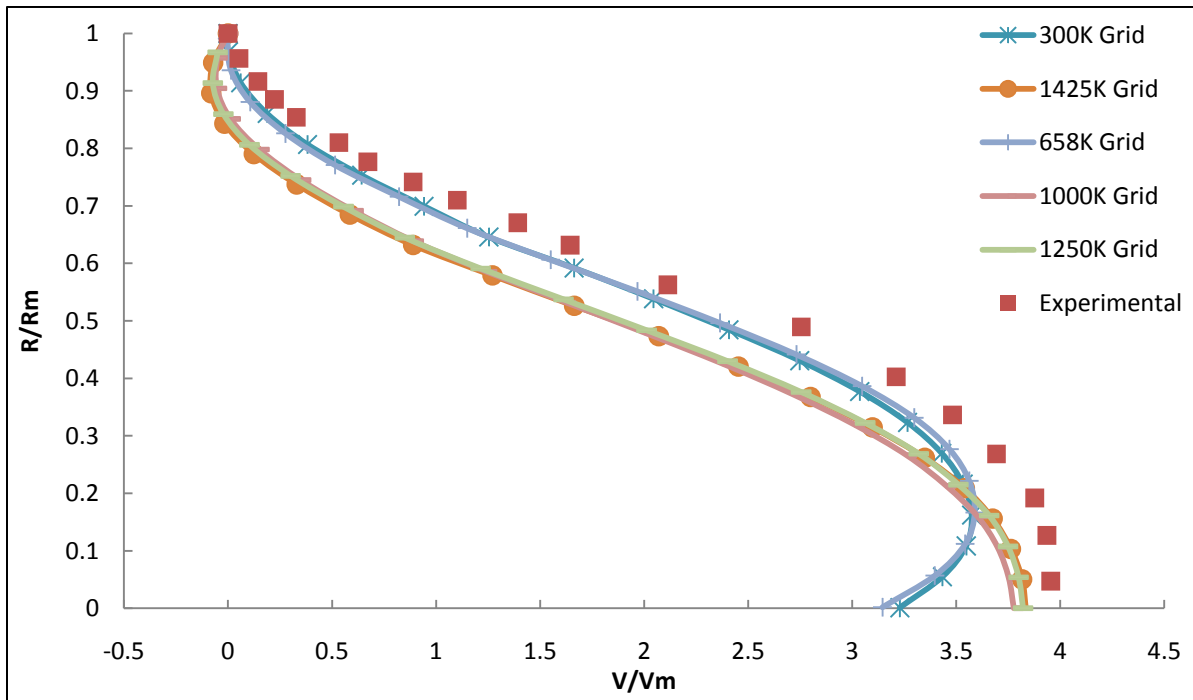


Figure 5.6 X-velocity profile for $X = 5.0 D$.

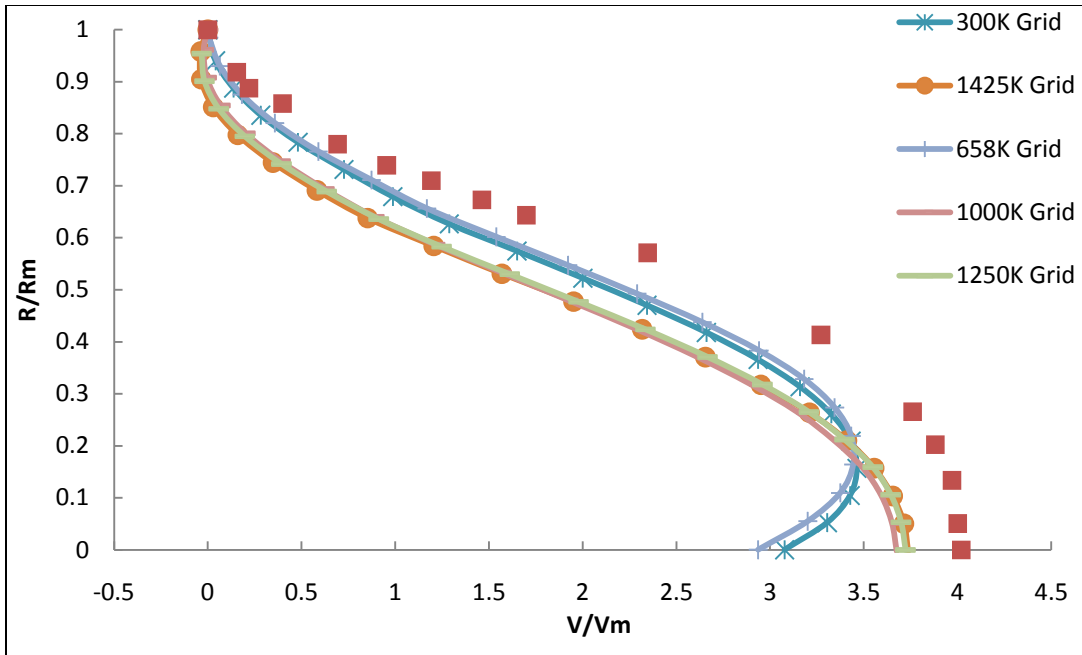


Figure 5.7 X-velocity profile for $X = 6.0 D$.

5.2 Grid Independence

In this investigation, wall shear stress was used to illustrate grid independence. Figure 5.8 illustrates the comparison of WSS using the κ - ω model at $Re = 100$.

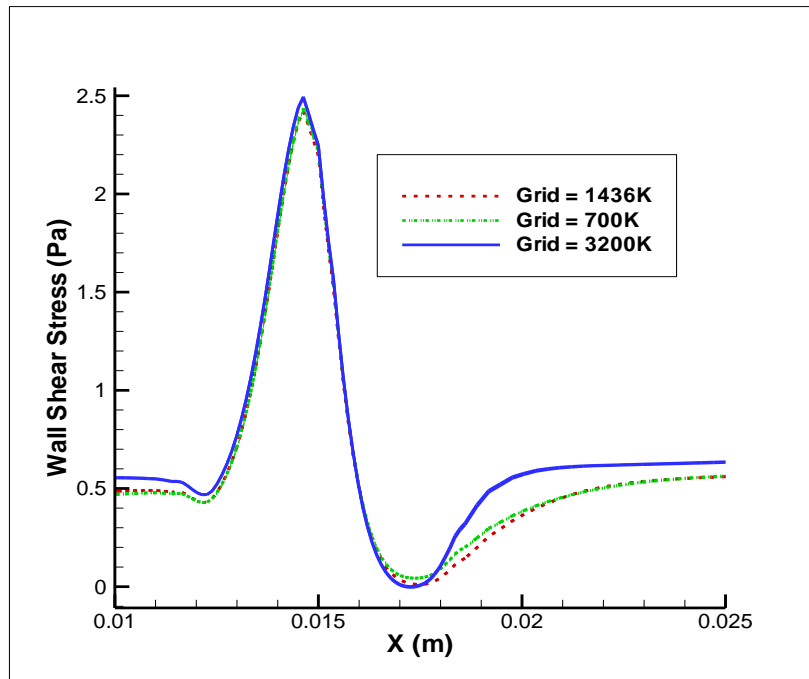


Figure 5.8 Comparison of WSS for model 1 with $\theta = 0.5^\circ$ and taper 25 percent diameter reduction.

It is very important to show grid independence when doing computational studies. To illustrate more and to show the grid independence, three different models using κ - ω model with different grid sizes were simulated. The grid sizes were 700 K, 1436 K, and 3200 K. The model with 3200 K grid points exhibited slightly higher shear stress at the stenosis and downstream of the stenosis, but it consumed a considerable amount of time. All three shear-stress values followed a similar pattern. It can be seen in Figure 5.8 that the results are almost similar and follow a similar pattern. For this simulation, the model with 1436 K grid points was simulated. The model with 3200 K grid points was not selected to avoid time consumption and memory storage. An increase in the outlet length had no effect on the WSS magnitude. A simulation was run with a 100 mm outlet length to investigate the effect of this on blood flow and WSS. The results are not shown, but WSS was the same as in the simulation in this thesis. Increasing outlet length had no effect on the results of the simulation.

CHAPTER 6

RESULTS

The numerical simulation of blood flow in a tapered artery with stenosis was performed by using the κ - ω model. The work in this thesis was an extension of the work by Dietiker and Hoffmann [67]. Thus far, the work done by various researchers has focused on a constant-diameter artery throughout the geometry. This thesis extended the fluid dynamics phenomenon taking place in a 3-D tapered artery. Liu et al. [68] and Deitiker and Hoffmann [67] simulated the same model with pulsatile flow in a 2-D and 3-D tapered artery, respectively. The investigation in this thesis included unsteady κ - ω model with pulsatile flow.

Figures 6.1 and 6.2 compare the WSS for a simple κ - ω model with a turbulent intensity of 0.1. A tapered artery with 25 percent diameter reduction was simulated for eight different Reynolds numbers ranging from 100 to 1500. It was observed that with a Reynolds number increase from 100 to 900, the WSS increased at the stenosed area, as shown in Figure 6.1. The same pattern can be observed in Figure 6.2. As the Reynolds number increased from 1100 to 1500 with turbulent intensity of 0.1, the WSS increased at a steady rate at the stenosed area.

The increase in WSS with an increasing Reynolds number could be due to an increase in the lateral velocity at the stenosed region. To maintain continuity, the velocity increased and the pressure decreased at the stenosed area. The velocity increased due to the difference in inlet and outer diameters. The inlet diameter was more than the outlet diameter. In other words, the tapered artery could be compared to the converging-diverging nozzle. In fact, the artery was constantly converging. A WSS greater than 34.4 Pascals was believed to rupture the endothelium and kick start the formation of thrombosis. In Figures 6.1 and 6.2 the WSS is greater than 34.4 Pascals.

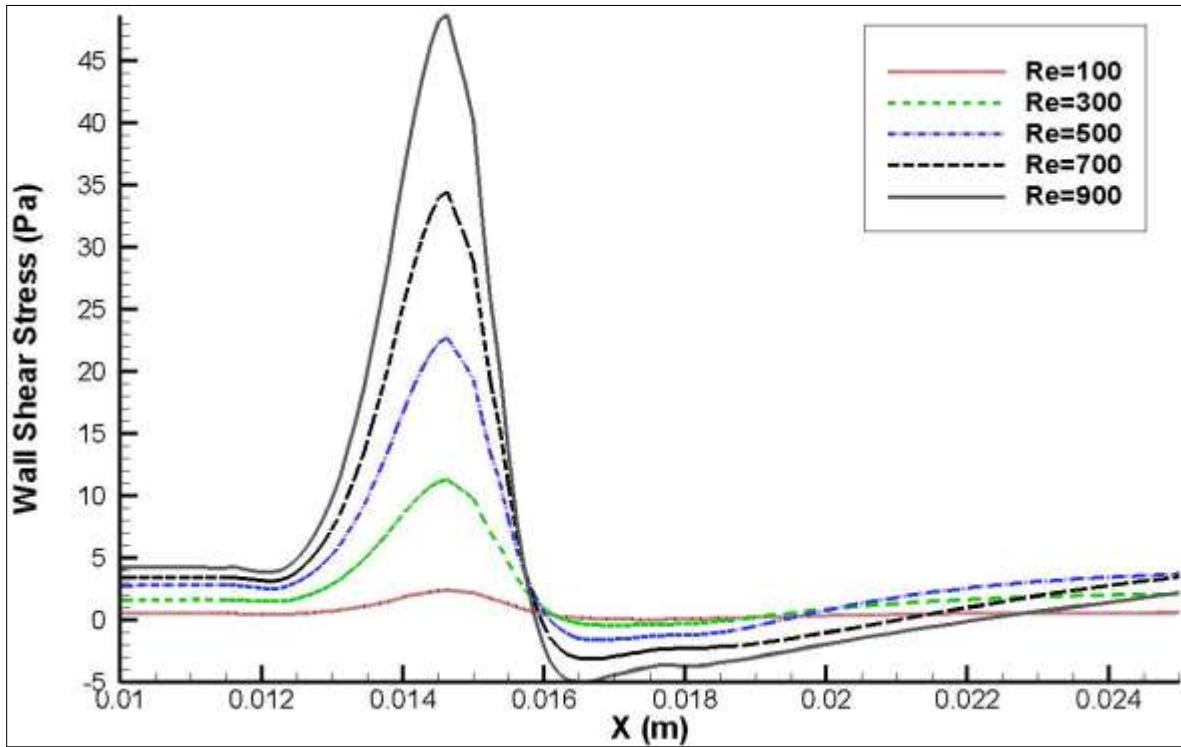


Figure 6.1 Comparison of WSS for Re = 100–900 with $T_{int} = 0.1$.

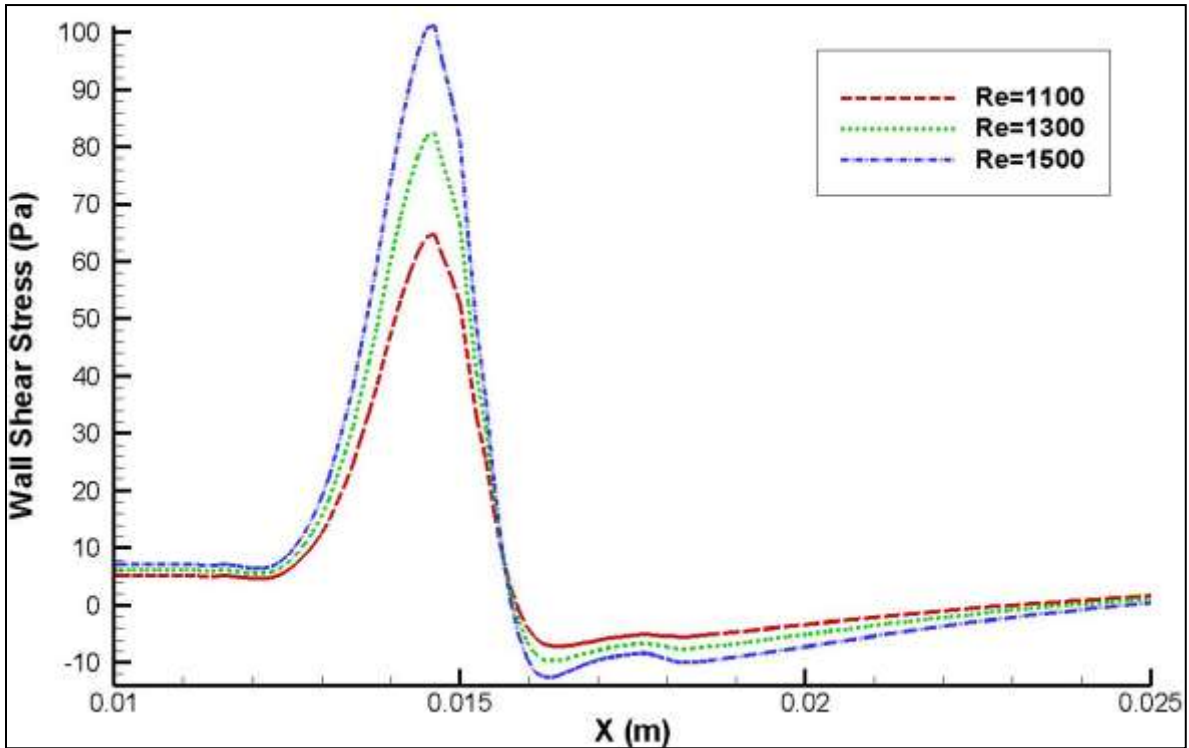


Figure 6.2 Comparison of WSS for Re = 1100–1500 with $T_{int} = 0.1$.

Figures 6.3 to 6.10 represent the X-velocity contours and streamline patterns for blood flow with the Reynolds number varying from 100 to 1500 at a constant turbulent intensity of 0.1. The streamlines in Figure 6.3 do not show any recirculation after the stenosis with $Re = 100$. The flow has no turbulence. But upon analyzing Figures 6.4 to 6.10, the recirculation zone after the stenosis is clearly visible. Flow separated when WSS was 0, and flow reattached when again WSS was 0.

Figures 6.11 and 6.12 illustrate the WSS for $Re = 100$ to 900 and $Re = 1100$ to 1500, respectively, with a turbulent intensity of 1.0. The trend observed in the WSS pattern is the same as shown in Figures 6.1 and 6.2. WSS increases with the increase in Reynolds number. Figures 6.13 and 6.14 and Figures 6.15 and 6.16 represent the WSS with a turbulent intensity of 2.0 and 4.0, respectively. A similar trend was observed in all four models with a turbulent intensity of 0.1 to 4.0. An increase in the turbulent intensity had no effect on shear stress at the same Reynolds number. A comparison of Figures 6.1, 6.2, and 6.13 to 6.16 reveals that the WSS in all four models remained constant at the respective Reynolds number, and there was no effect of increased turbulent intensity on the tapered stenosed artery.

Figures 6.17 to 6.22 represent the X-velocity contour and streamlines for $Re = 100$ to 700 and 1300 to 1500 with a turbulent intensity of 4.0. Streamlines in Figure 6.11 having a Reynolds number of 100 and a turbulent intensity of 4.0 did not show recirculation after stenosis. A similar pattern occurred as was observed in Figure 6.3. It can be concluded that an increase in turbulent intensity has no effect on recirculation and flow pattern. In a tapered artery, only the Reynolds number plays a significant role.

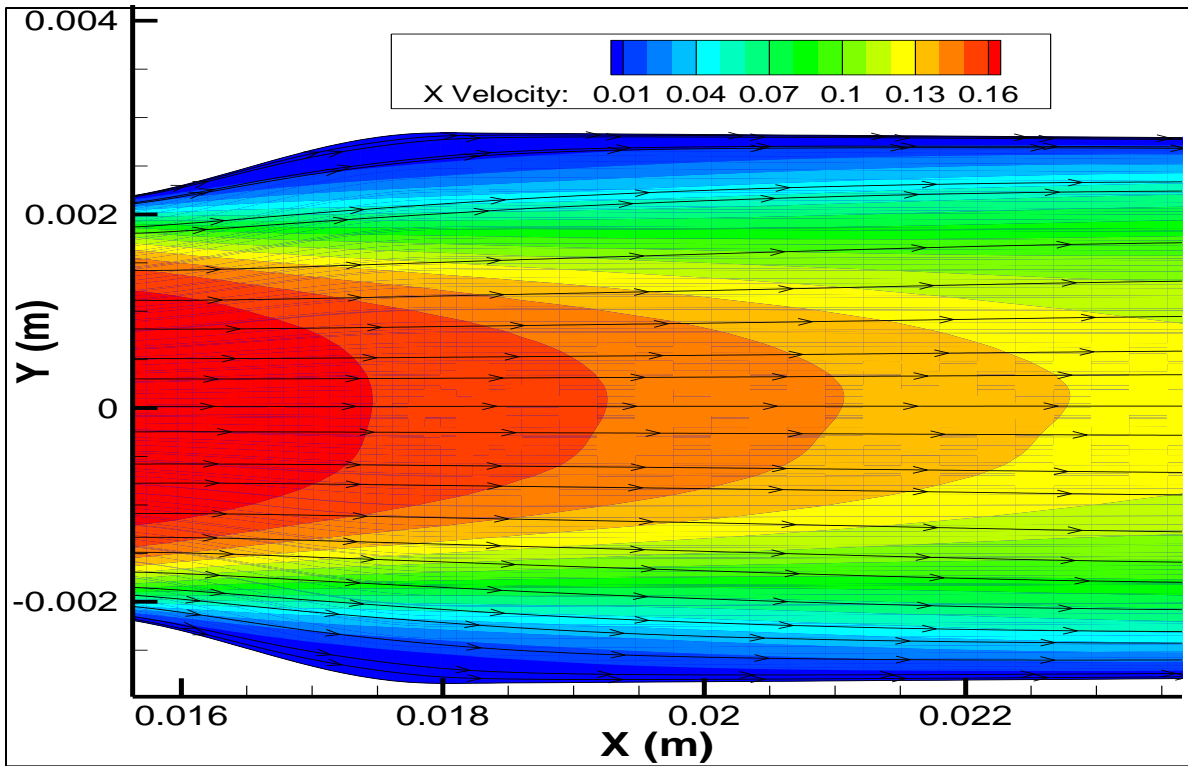


Figure 6.3 X-velocity contours and streamlines for $Re = 100$, $T_{int} = 0.1$.

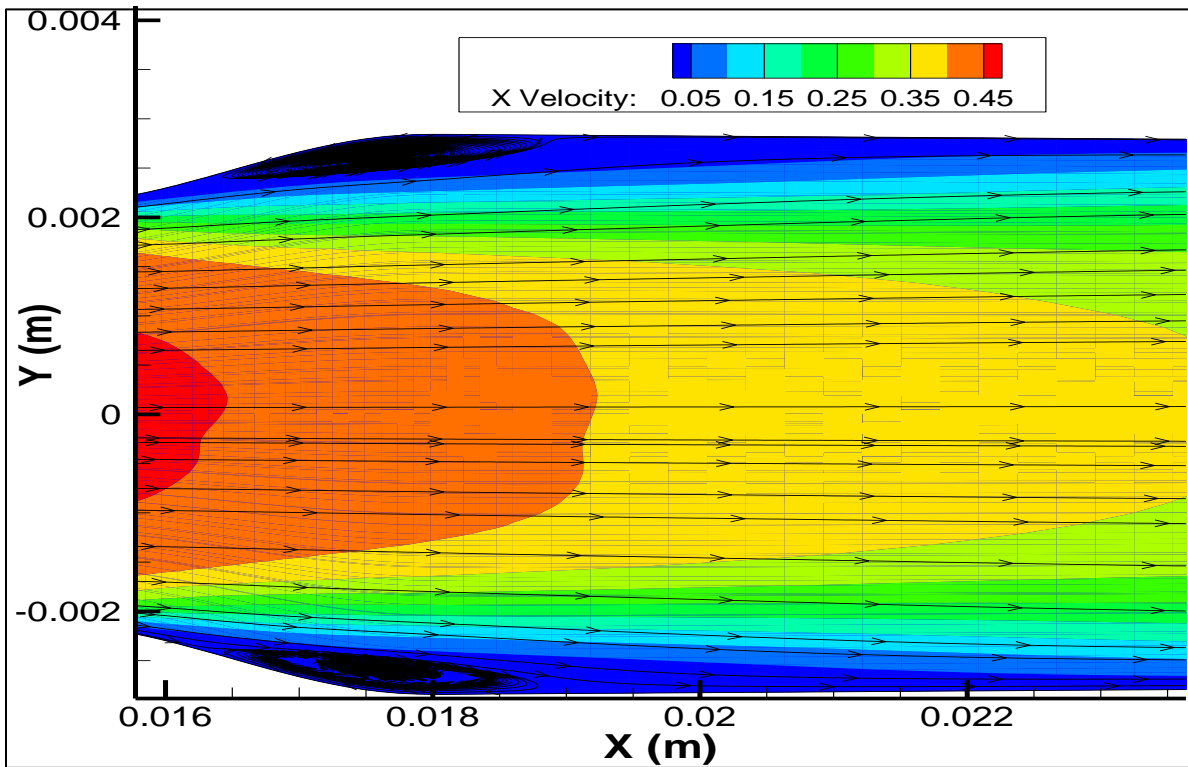


Figure 6.4 X-velocity contours and streamlines for $Re = 300$, $T_{int} = 0.1$.

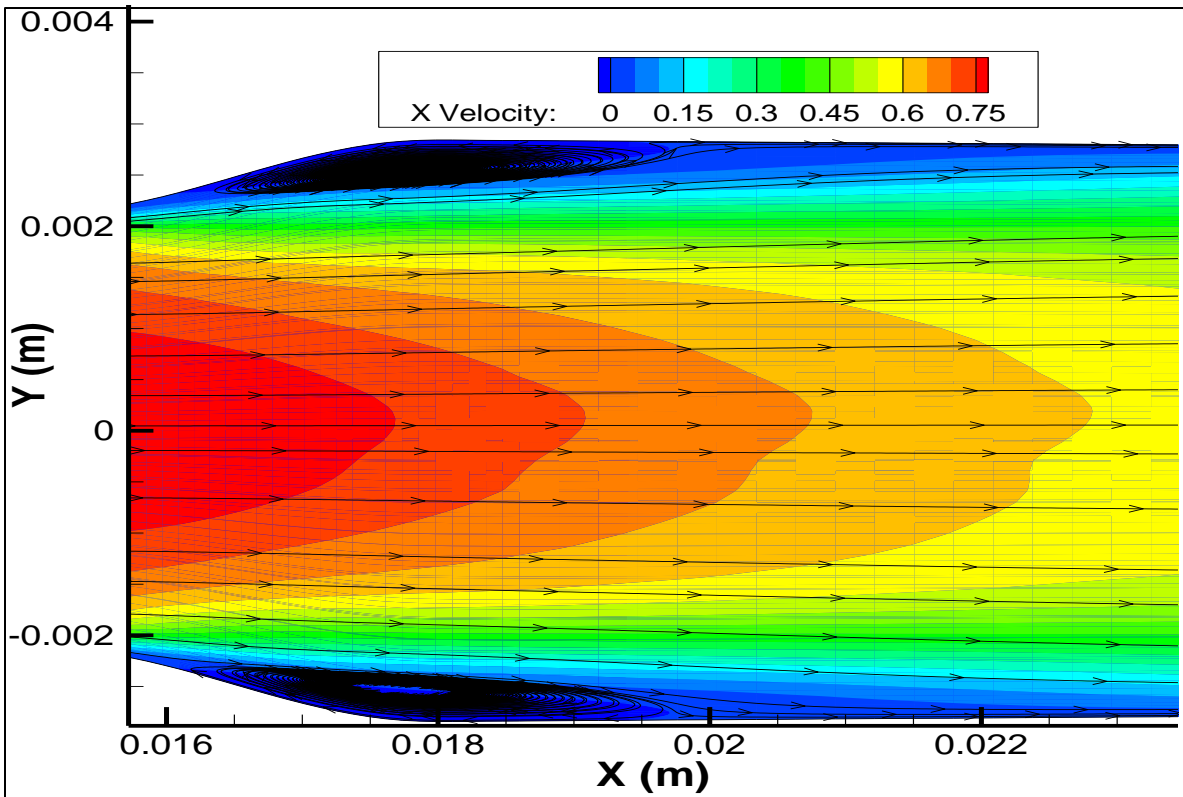


Figure 6.5 X-velocity contours and streamlines for $Re = 500$, $T_{int} = 0.1$.

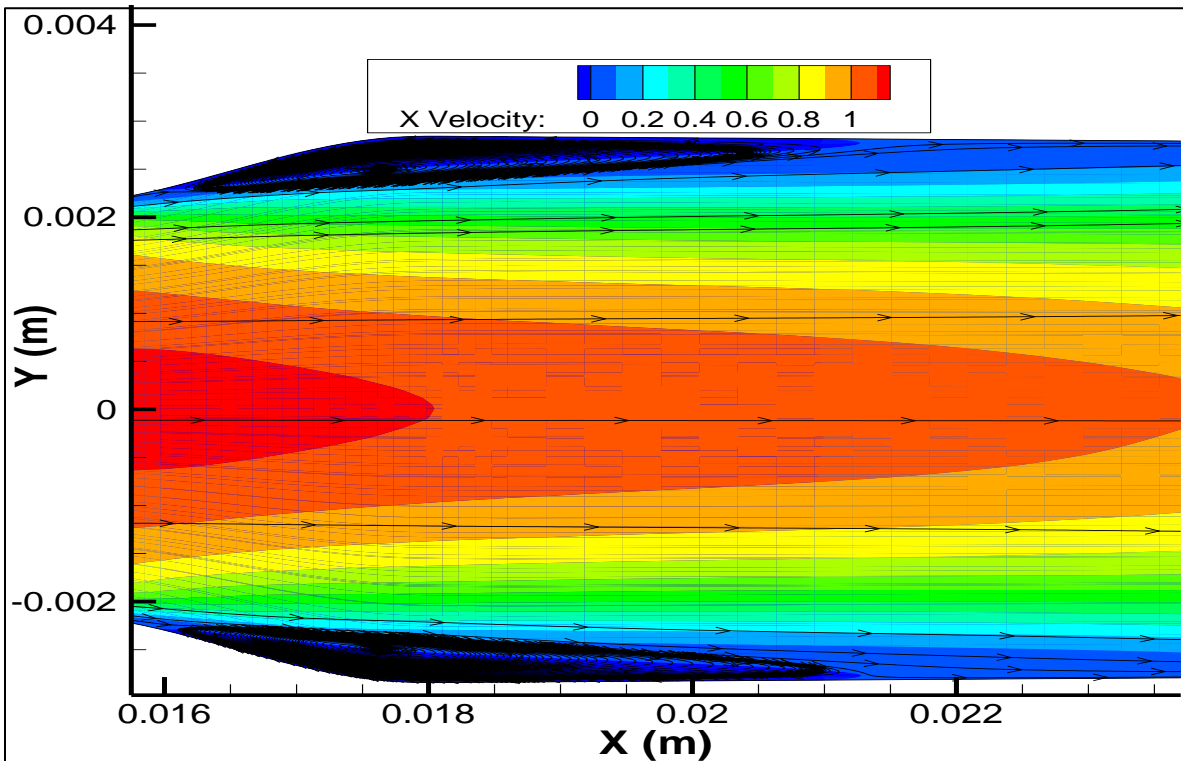


Figure 6.6 X-velocity contours and streamlines for $Re = 700$, $T_{int} = 0.1$.

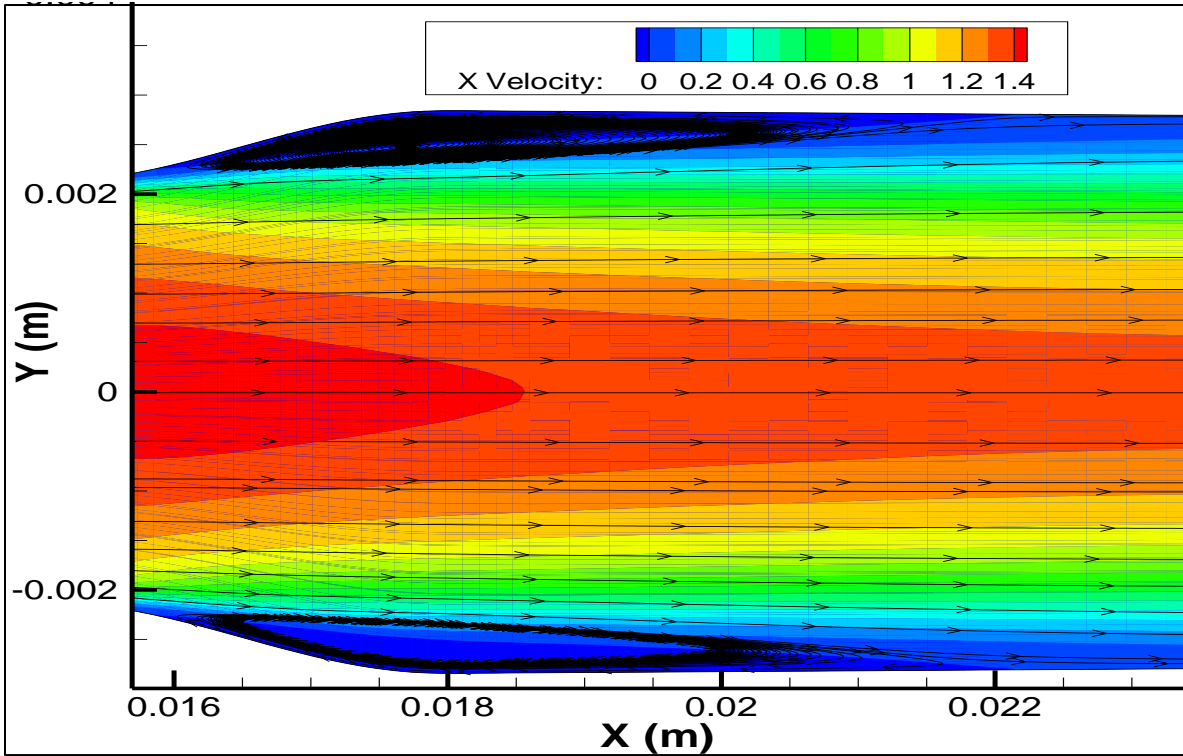


Figure 6.7 X-velocity contours and streamlines for $Re = 900$, $T_{int} = 0.1$.

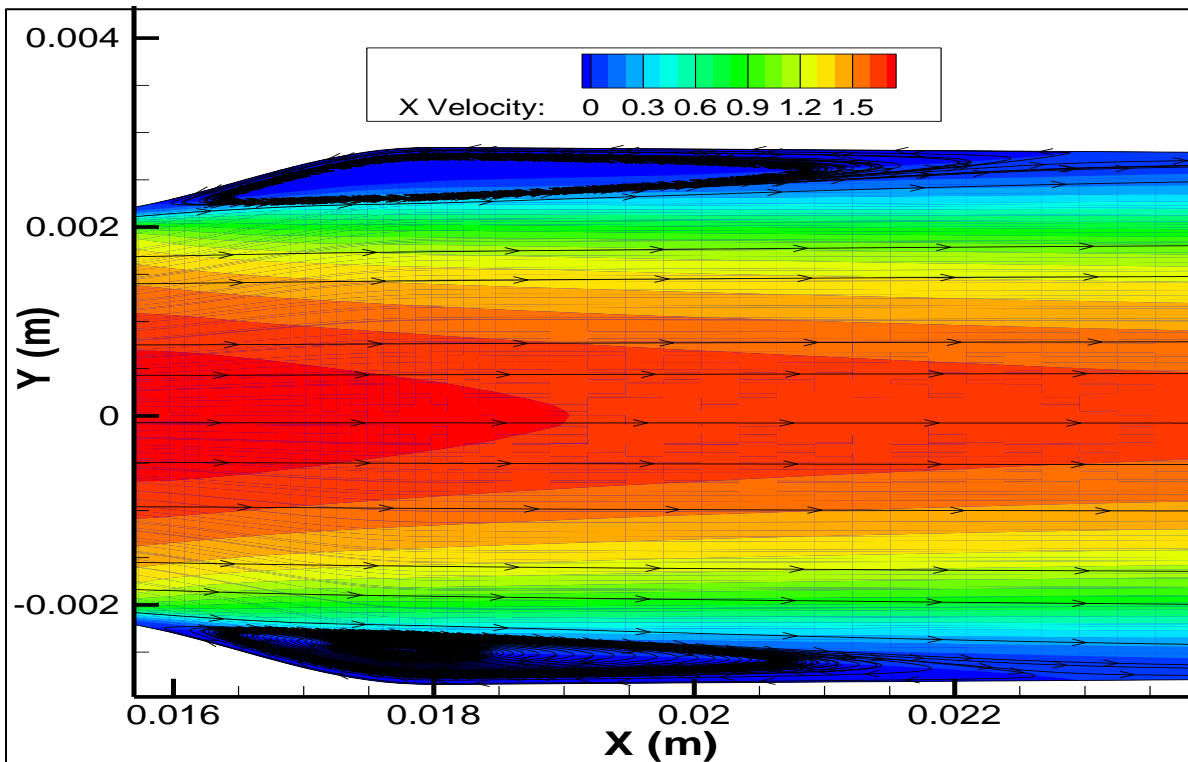


Figure 6.8 X-velocity contours and streamlines for $Re = 1100$, $T_{int} = 0.1$.

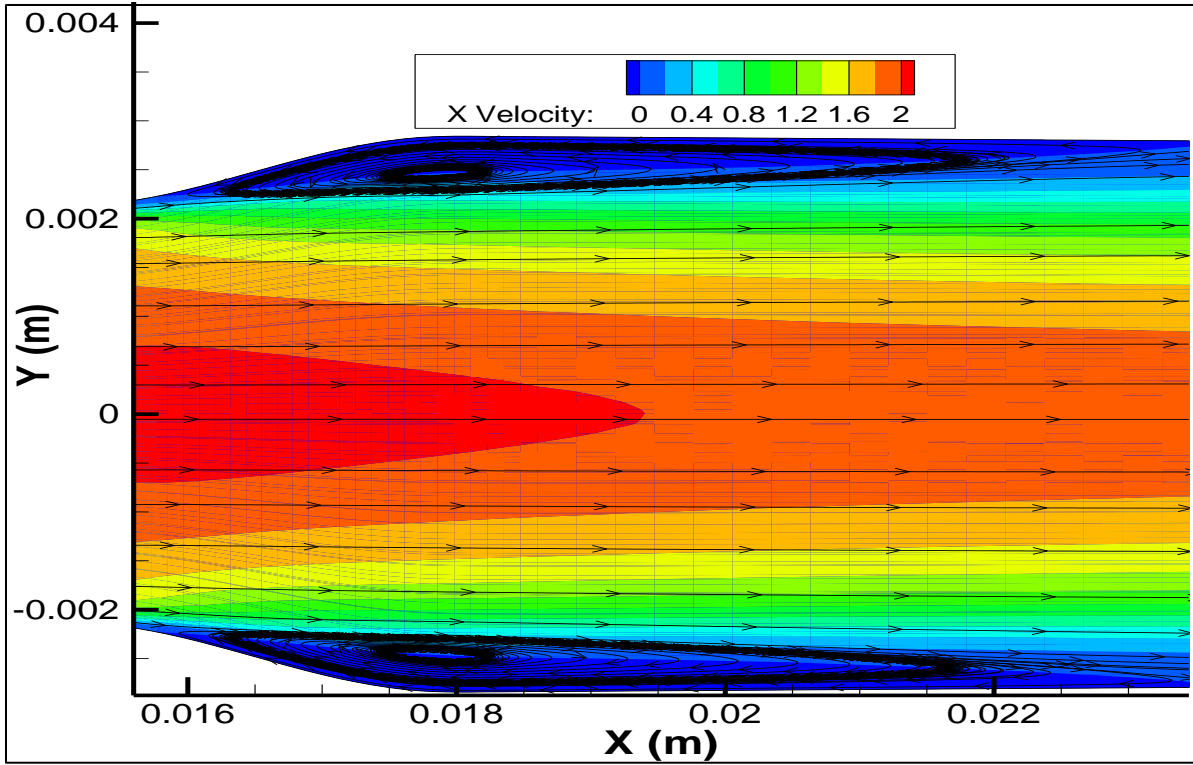


Figure 6.9 X-velocity contours and streamlines for $Re = 1300$, $T_{int} = 0.1$.

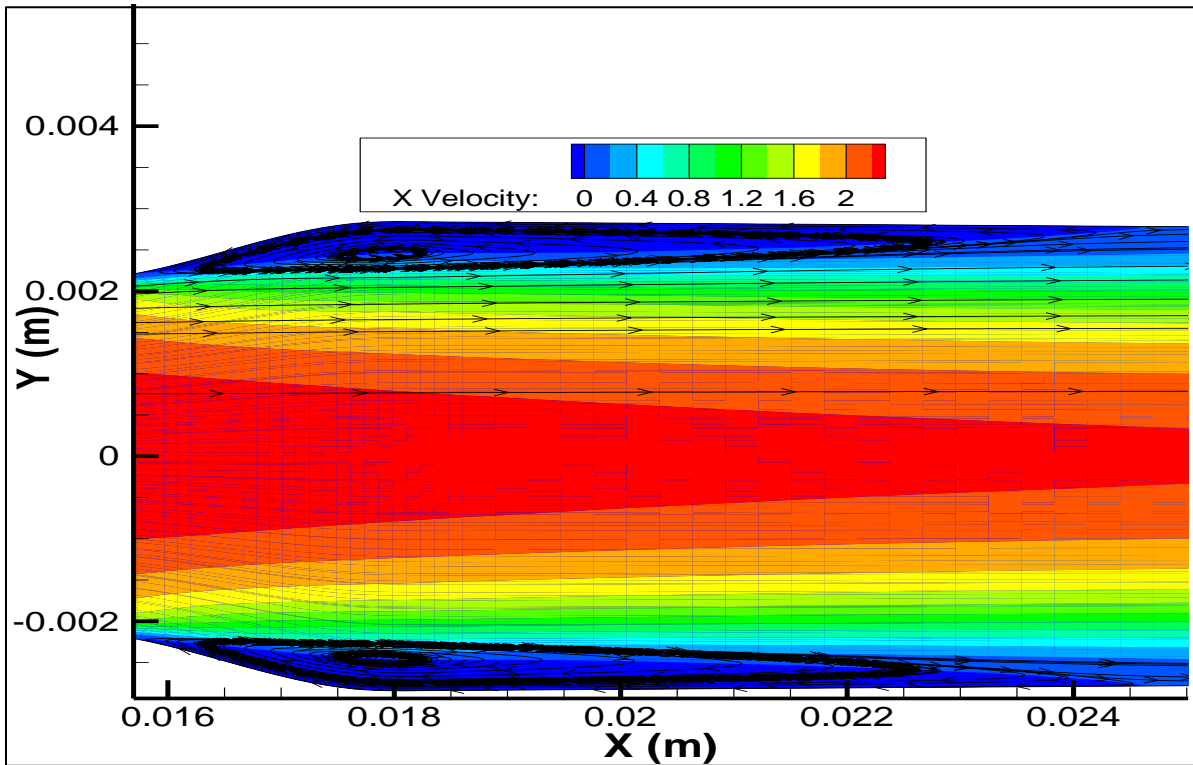


Figure 6.10 X-velocity contours and streamlines for $Re = 1500$, $T_{int} = 0.1$.

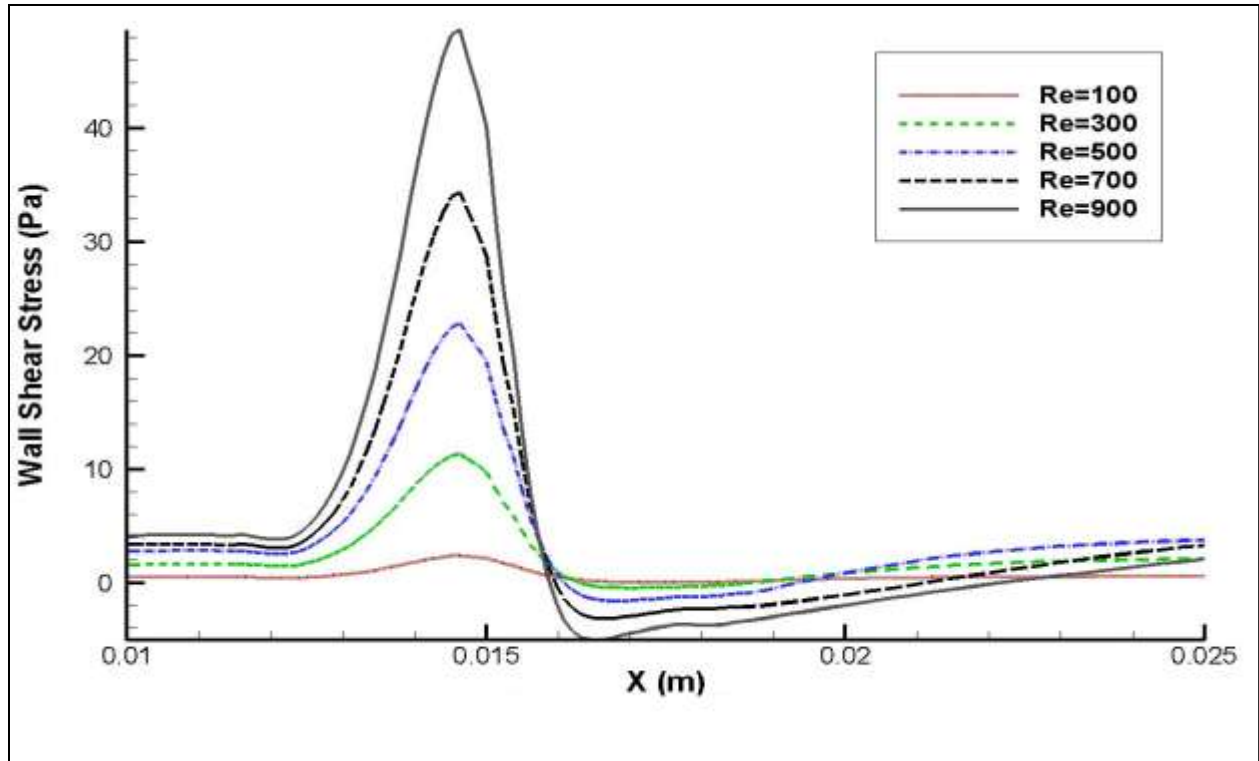


Figure 6.11 Comparison of WSS for $Re = 100-900$ with $T_{int} = 1.0$.

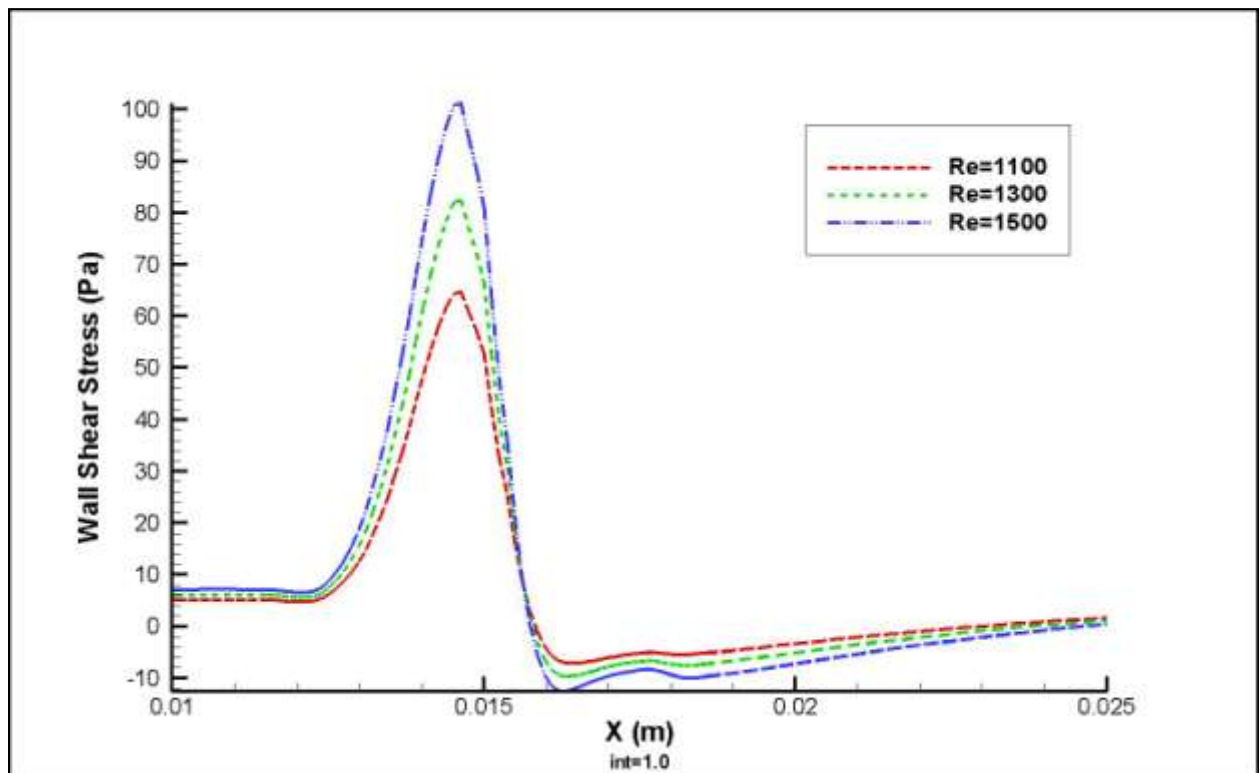


Figure 6.12 Comparison of WSS for $Re = 1100-1500$ with $T_{int} = 1.0$.

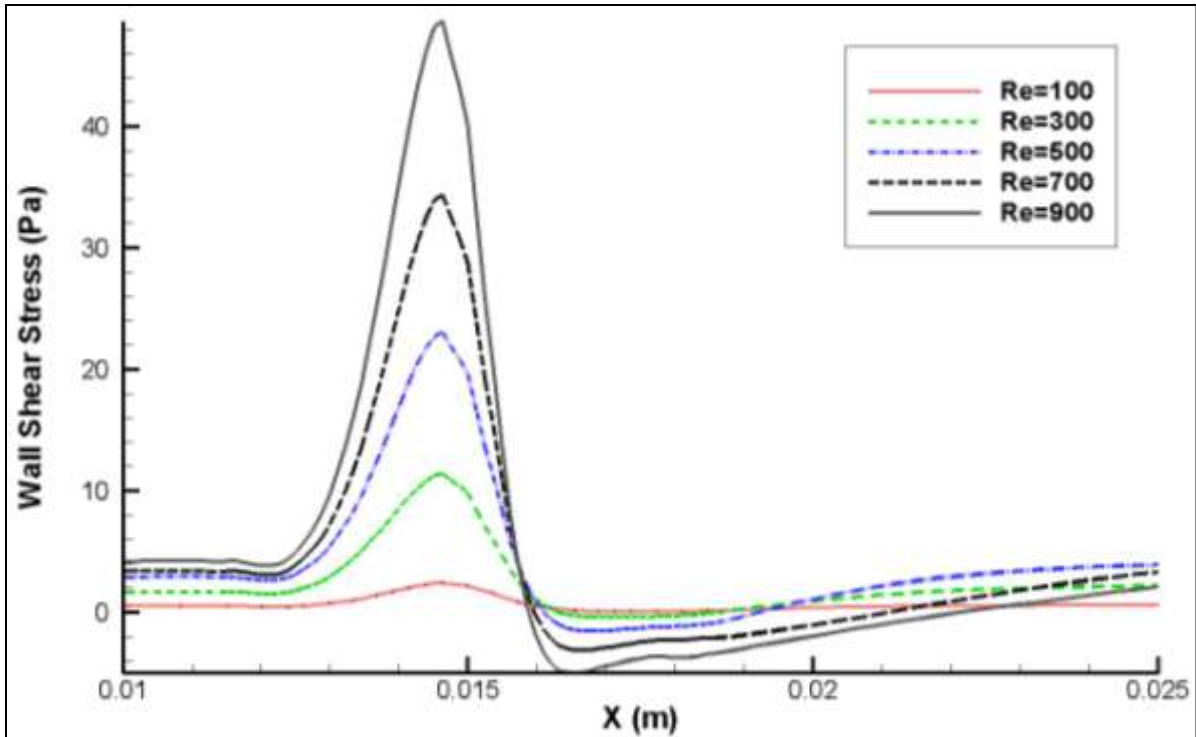


Figure 6.13 Comparison of WSS for $Re = 100-900$ with $T_{int} = 2.0$.

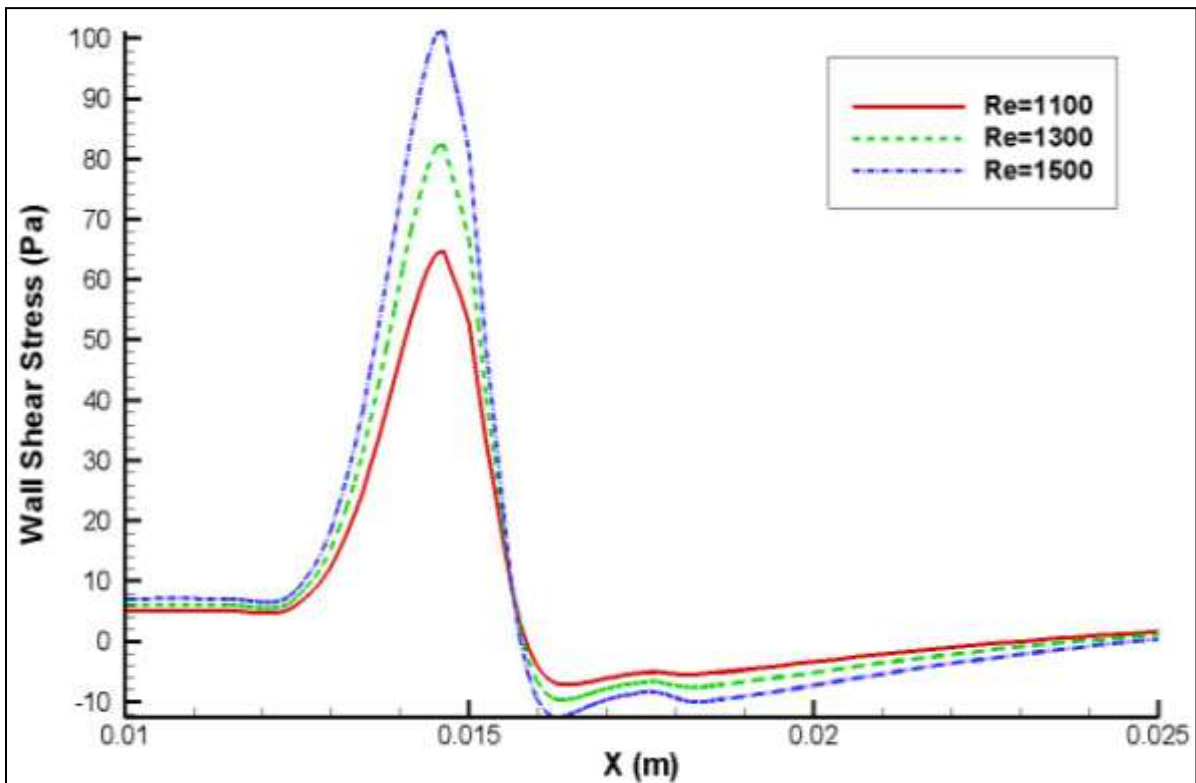


Figure 6.14 Comparison of WSS for $Re = 1100-1500$ with $T_{int} = 2.0$.

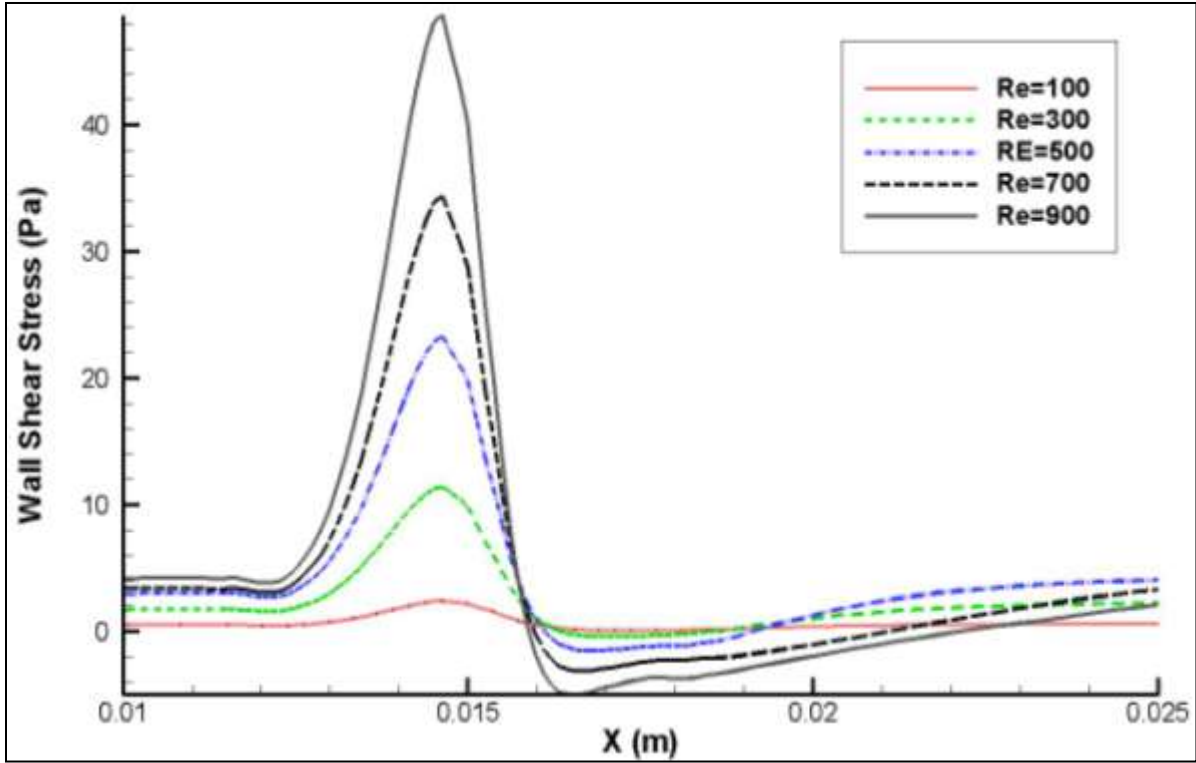


Figure 6.15 Comparison of WSS for $Re = 100-900$ with $T_{int} = 4.0$.

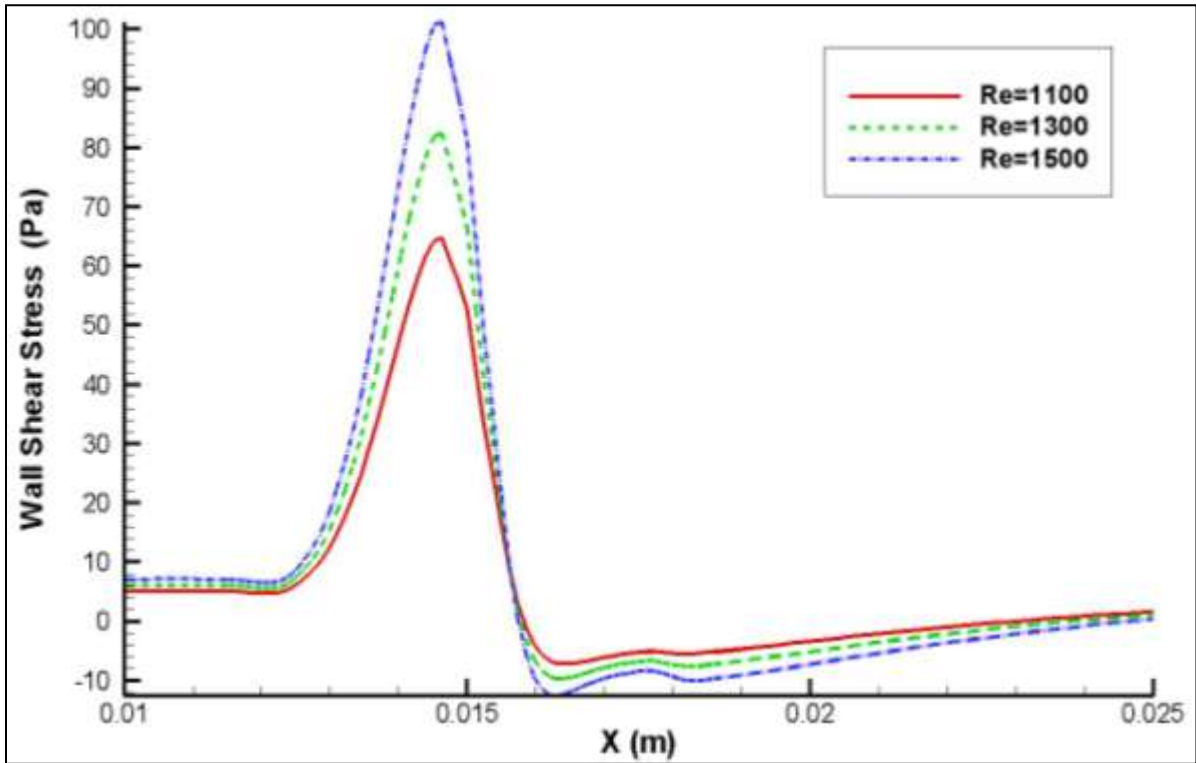


Figure 6.16 Comparison of WSS for $Re = 1100-1500$ with $T_{int} = 4.0$.

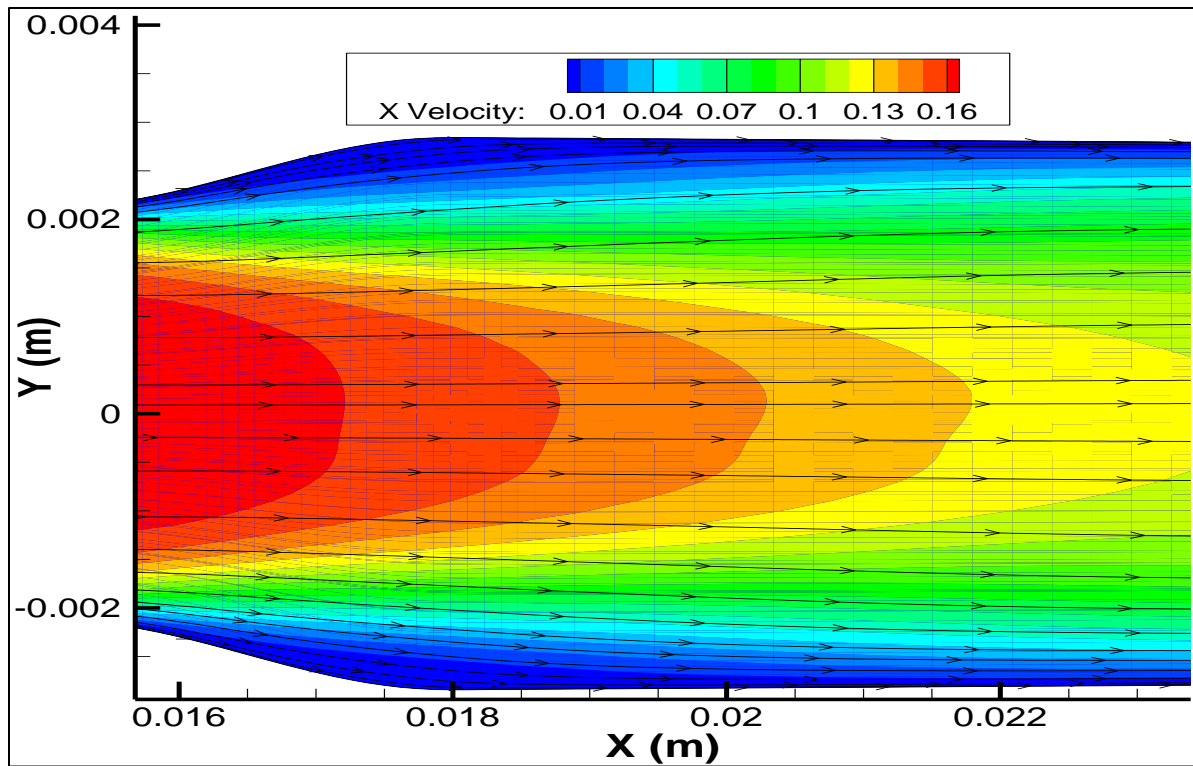


Figure 6.17 X-velocity contours and streamlines for $Re = 100$, $T_{int} = 4.0$.

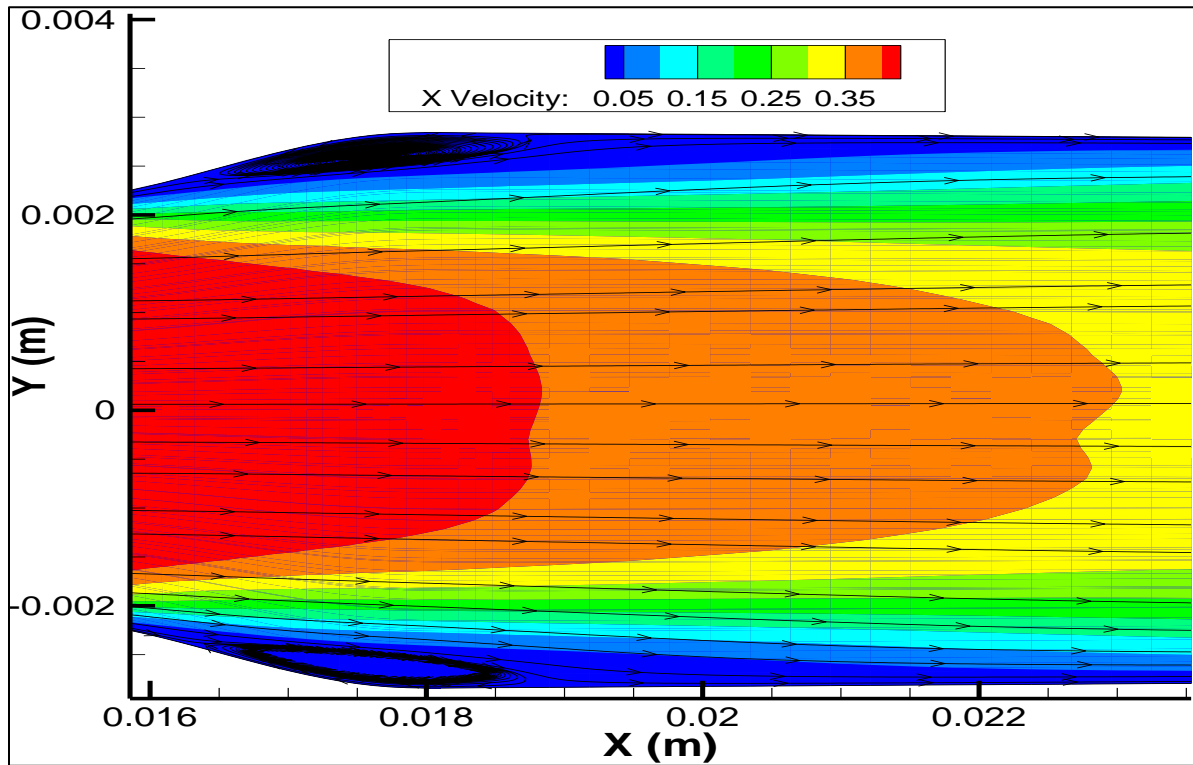


Figure 6.18 X-velocity contours and streamlines for $Re = 300$, $T_{int} = 4.0$.

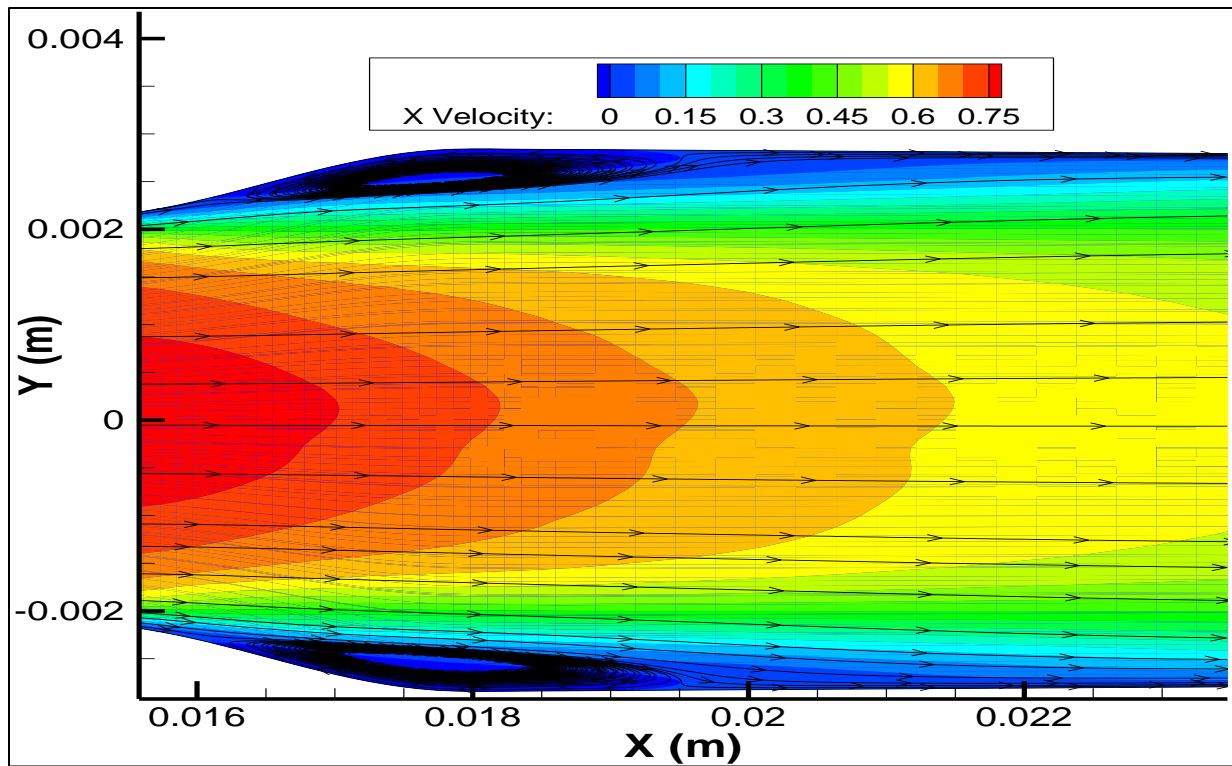


Figure 6.19 X-velocity contours and streamlines for $Re = 500$, $T_{int} = 4.0$.

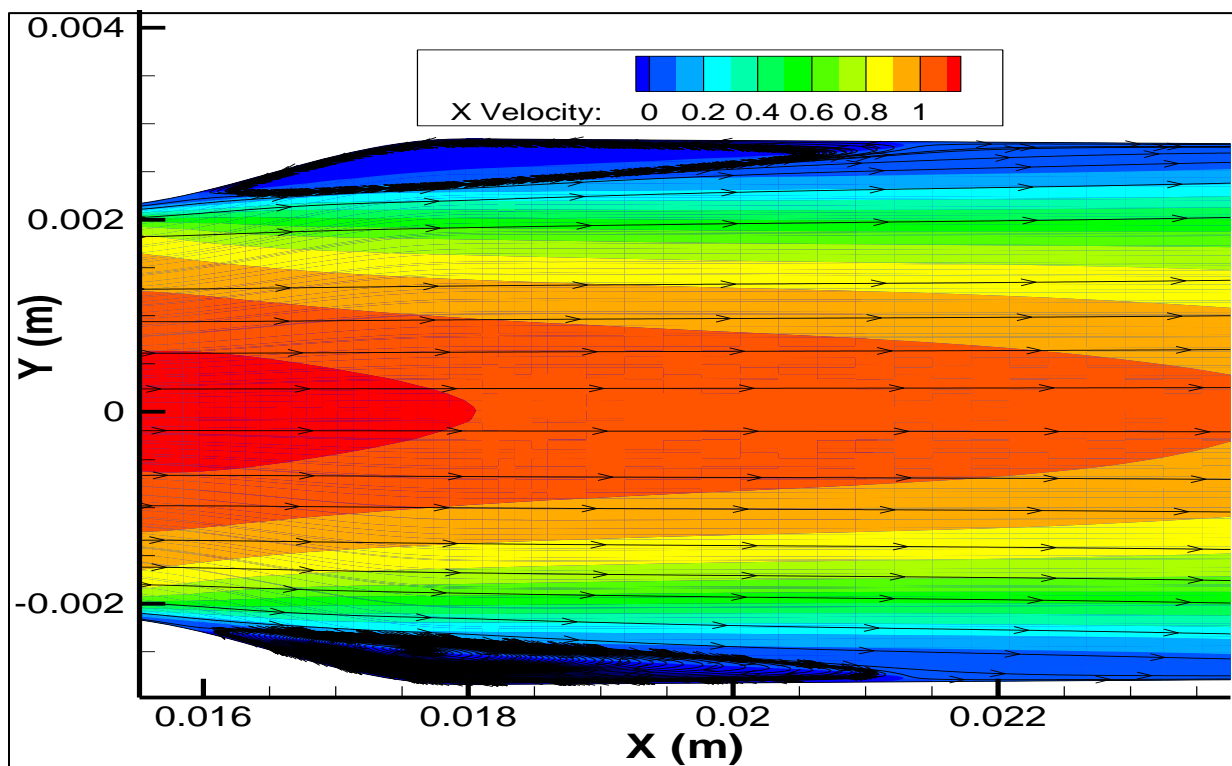


Figure 6.20 X-velocity contours and streamlines for $Re = 700$, $T_{int} = 4.0$.

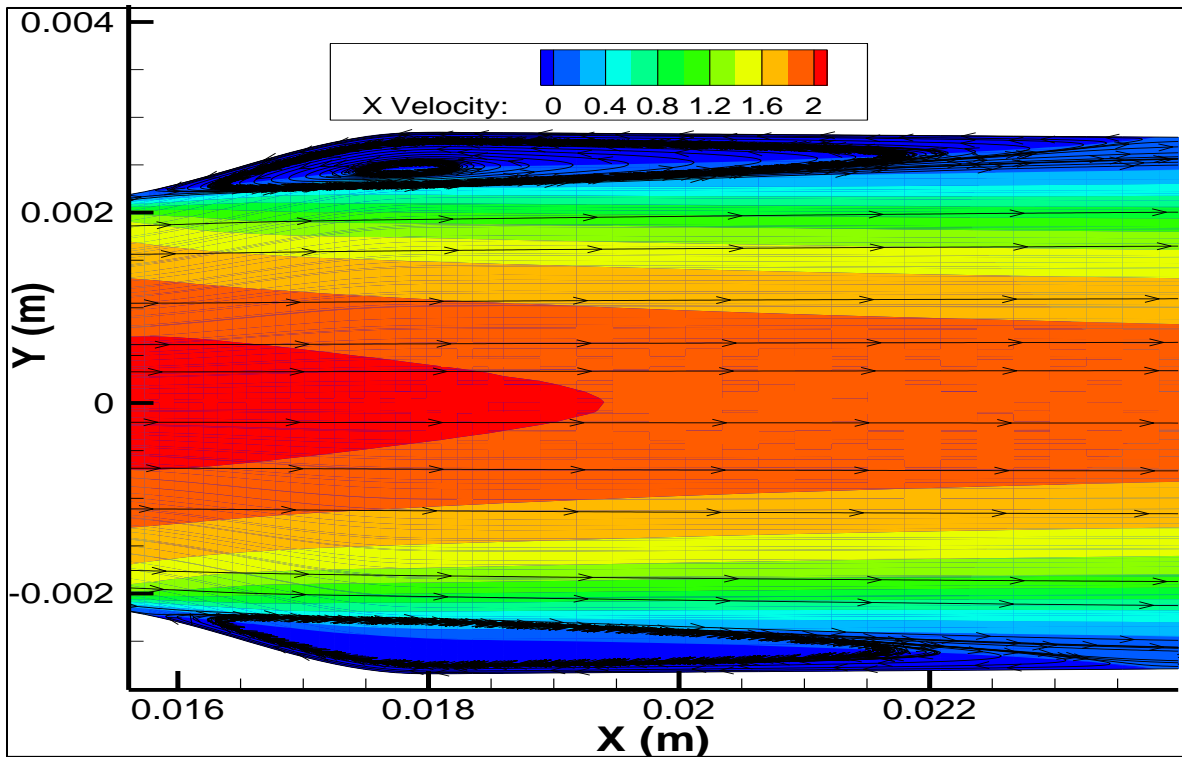


Figure 6.21 X-velocity contours and streamlines for $Re = 1300$, $T_{int} = 4.0$.

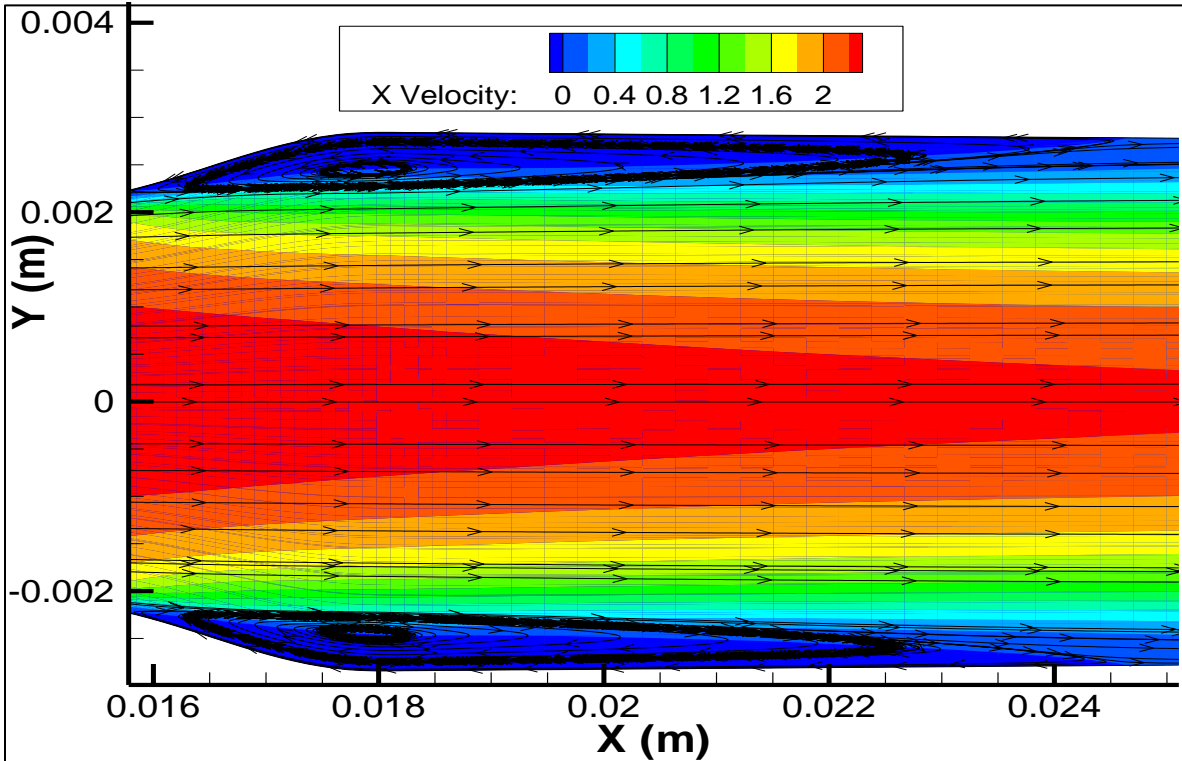


Figure 6.22 X-velocity contours and streamlines for $Re = 1500$, $T_{int} = 4.0$.

Figures 6.23 and 6.24 illustrate the wall shear stress for $Re = 100$ to 900 and $Re = 1100$ to 1500 , respectively, with a turbulent intensity of 0.1 . A transitional version of the $\kappa-\omega$ model was employed to obtain the WSS. No change in wall shear stress was observed for $Re = 100$ to 1500 with a turbulent intensity of 0.1 . WSS in Figures 6.23 and 6.24 illustrates the same pattern and results as observed in Figures 6.1 and 6.2. The $T_{\kappa-\omega}$ model predicted the same WSS as predicted by the simple $\kappa-\omega$ model. To further illustrate the effect of turbulent intensity on the $T_{\kappa-\omega}$ model, another simulation was run with a turbulent intensity of 2.0 for $Re = 100$ to 1500 . No significant change in WSS was observed with the increase in turbulent intensity using the $T_{\kappa-\omega}$ model. Both the simple $\kappa-\omega$ model and the $T_{\kappa-\omega}$ model predicted the same values of WSS, regardless of turbulent intensity. WSS in Figure 6.25 and 6.26 also illustrates the same pattern as observed in Figures 6.1 and 6.2 respectively.

One observation to be made here is that regardless of any place, or inlet and outlet length, the pattern of WSS was constant. The magnitude of shear stress at the stenosis depends on the geometry, degree of stenosis, and inlet conditions.

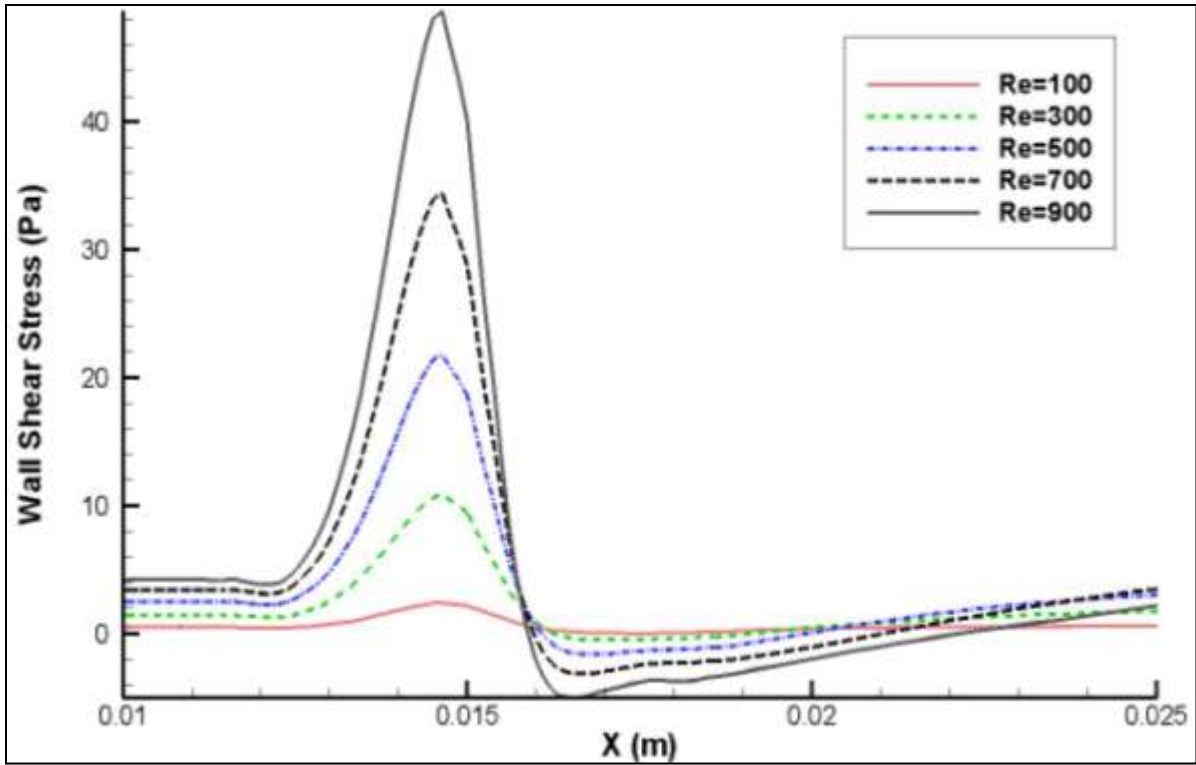


Figure 6.23 Comparison of WSS for $Re = 100\text{--}900$ with $T_{int} = 0.1$ for $T_{\kappa-\omega}$ model.

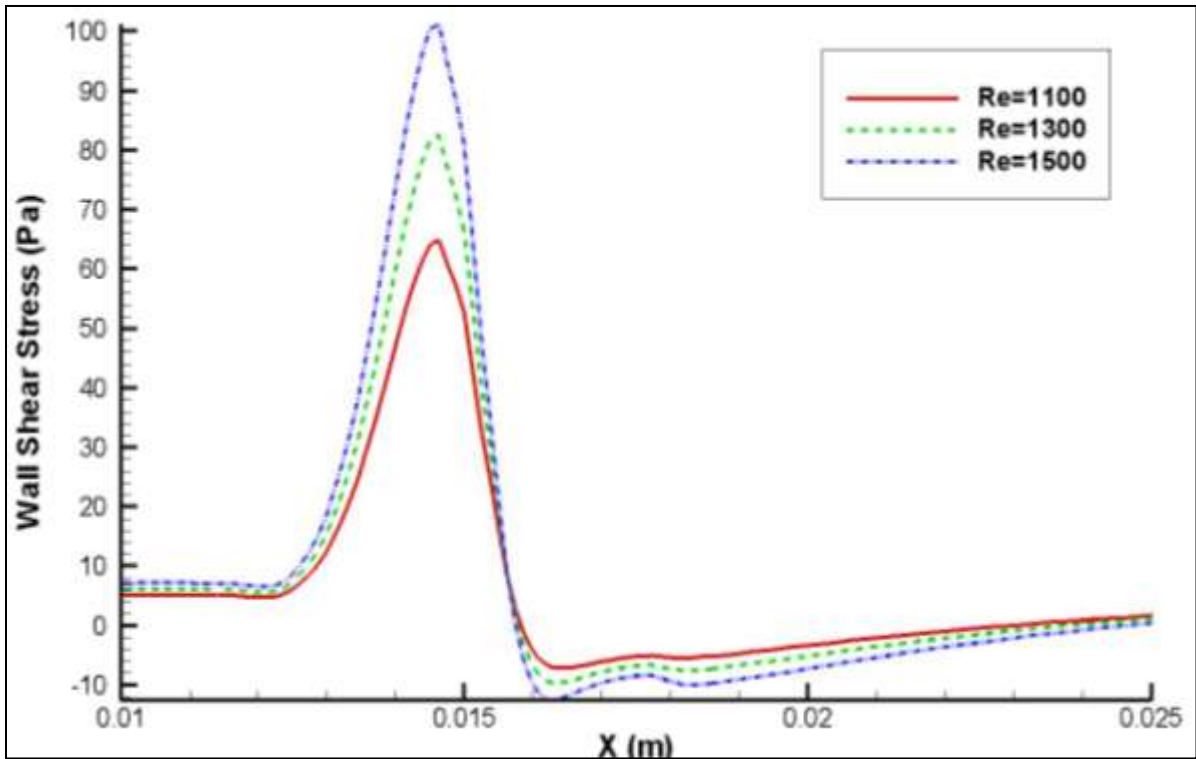


Figure 6.24 Comparison of WSS for $Re = 1100\text{--}1500$ with $T_{int} = 0.1$ for $T_{\kappa-\omega}$ model.

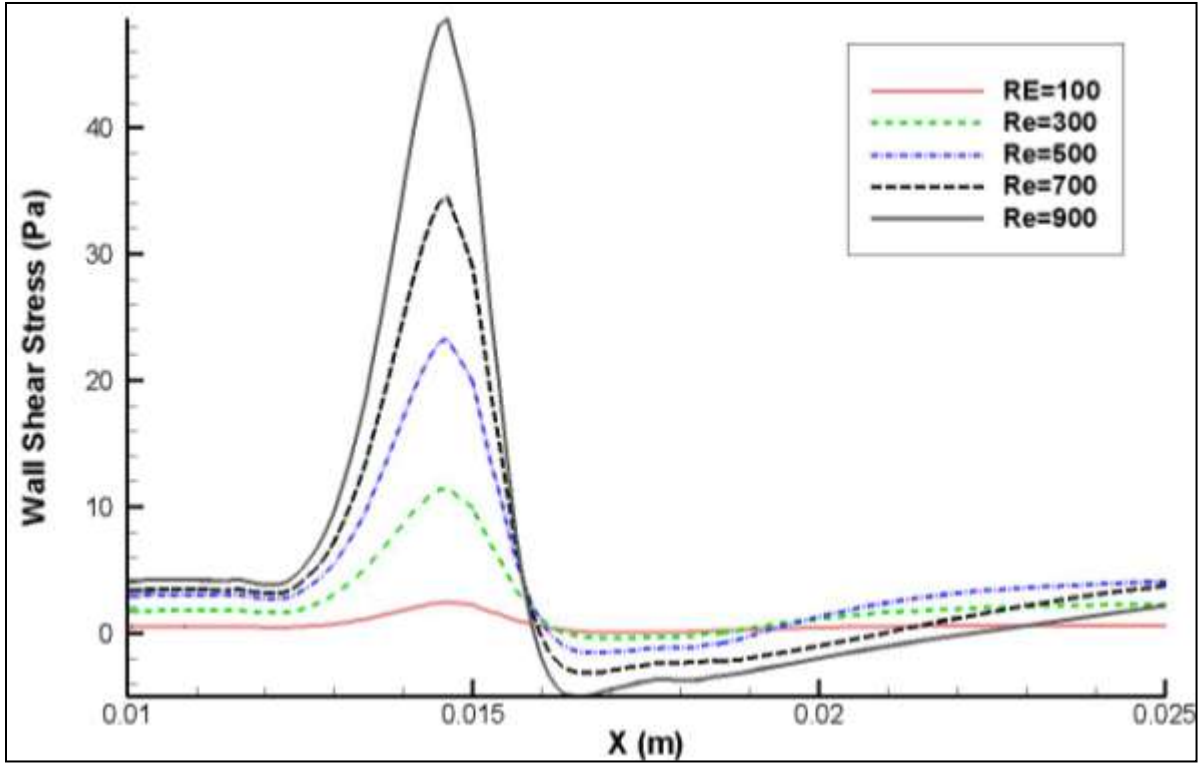


Figure 6.25 Comparison of WSS for $Re = 100\text{--}900$ with $T_{int} = 2.0$ for $T_{\kappa-\omega}$ model.

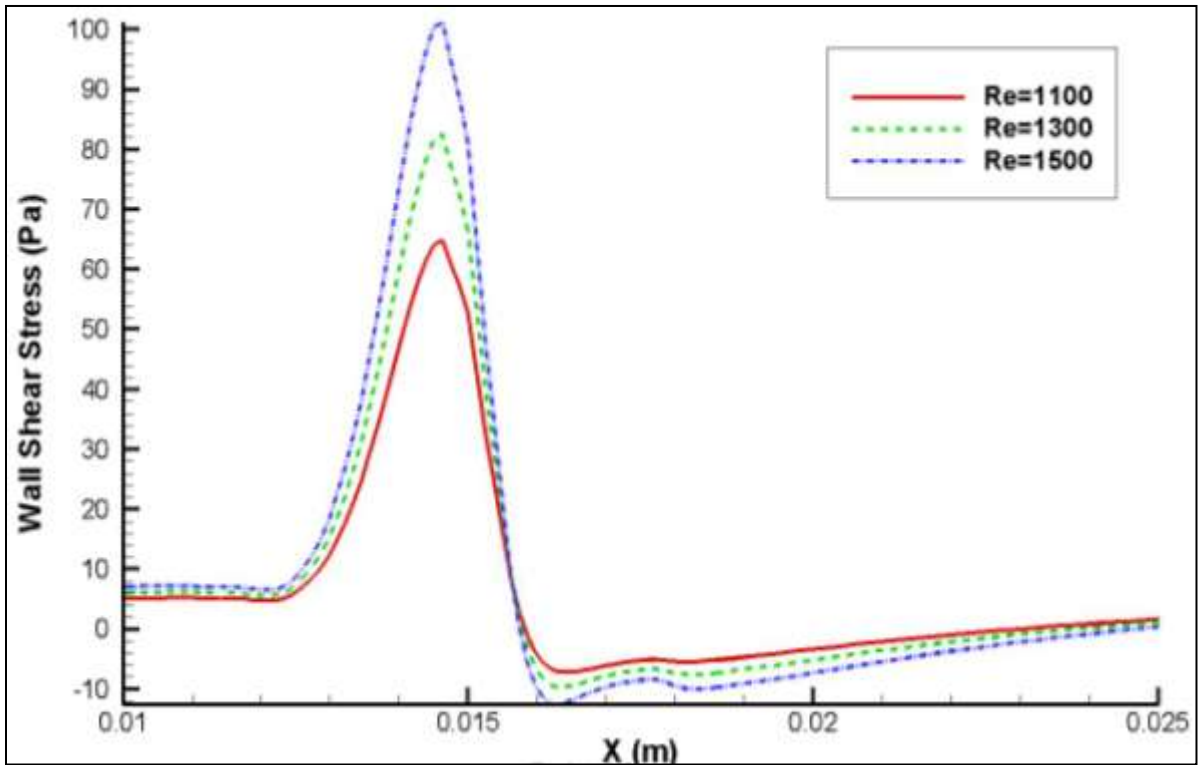


Figure 6.26 Comparison of WSS for $Re = 1100\text{--}1500$ with $T_{int} = 2.0$ for $T_{\kappa-\omega}$ model.

Figure 6.27 illustrates the recirculation length as a function of the Reynolds number with 25 percent diameter reduction under steady conditions using the $\kappa\text{-}\omega$ model with turbulent intensity ranging from 0.1 to 1.0 to 2.0 to 4.0. Figure 6.28 also illustrates the recirculation length as a function of the Reynolds number with 25 percent diameter reduction under steady conditions using the $T_{\kappa\text{-}\omega}$ model with turbulent intensity of 0.1 and 2.0. Both results are compared in Figure 6.29. No significant change in the length of recirculation was observed. The recirculation length remains the same in both of the models. It can also be seen that the separation point slightly moves upstream of the stenosis as the Reynolds number increases.

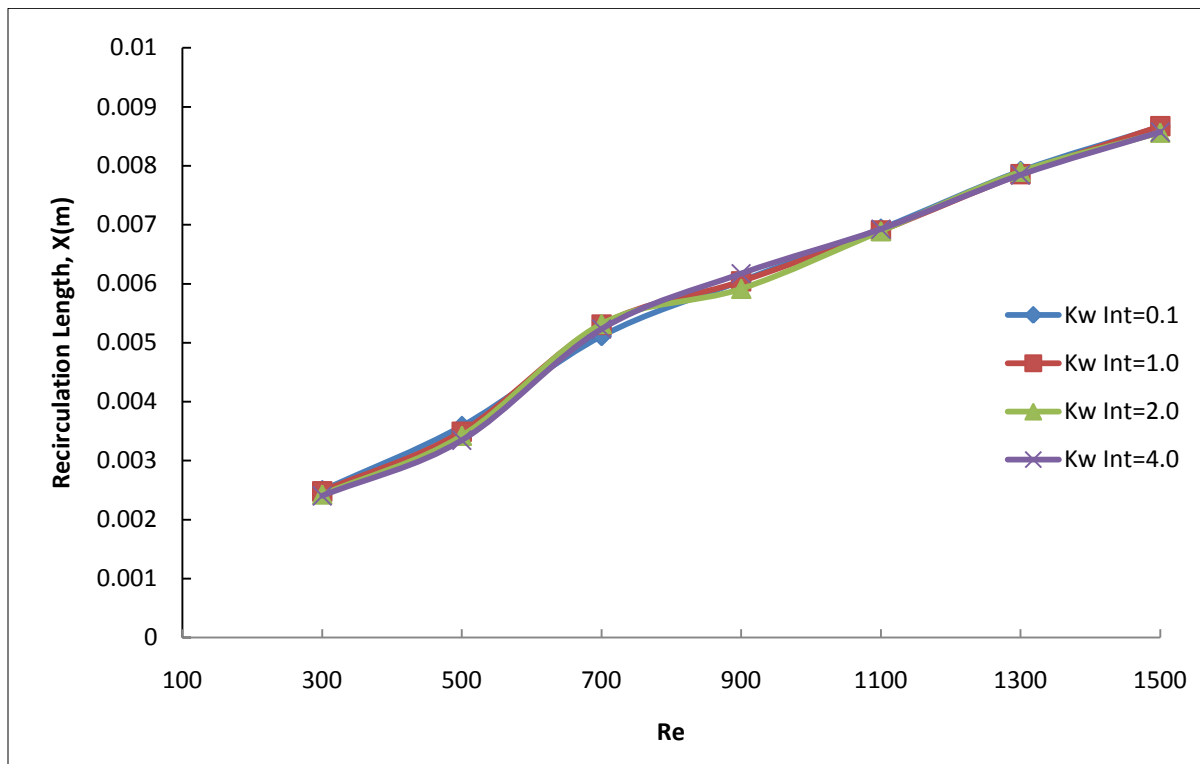


Figure 6.27 Recirculation as a function of Reynolds numbers with 25 percent diameter reduction under steady condition for $\kappa\text{-}\omega$ model with $T_{\text{int}} = 0.1, 1.0, 2.0, 4.0$.

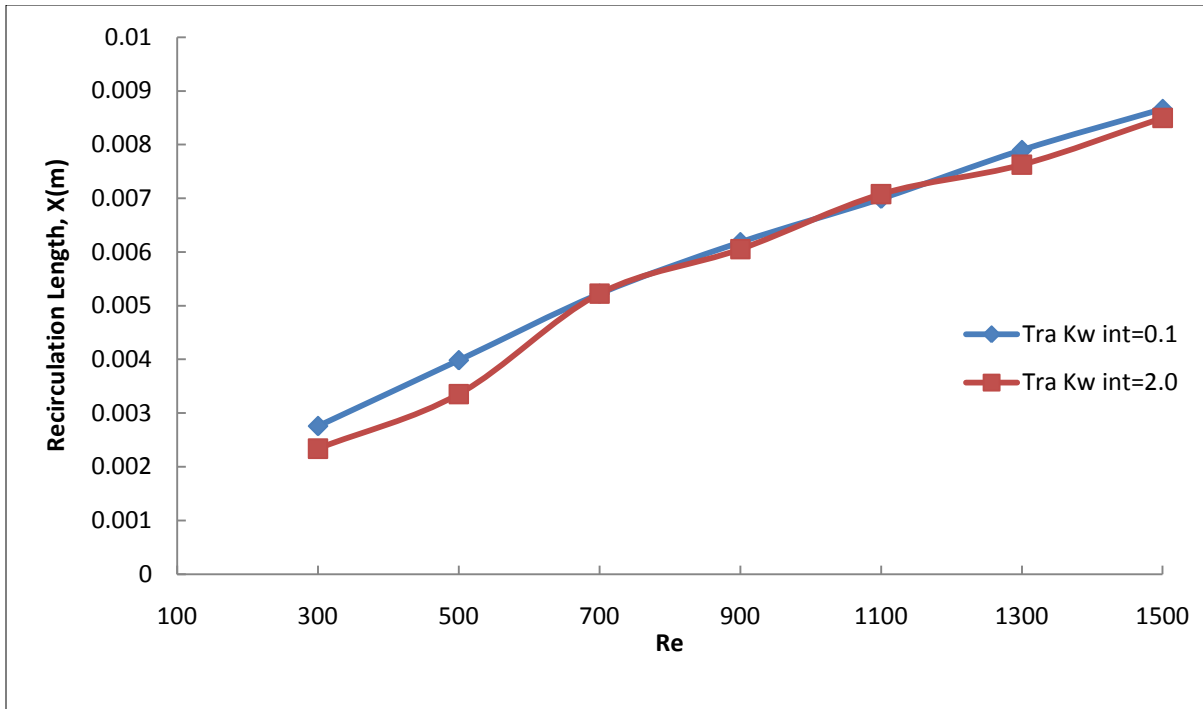


Figure 6.28 Recirculation as a function of Reynolds numbers with 25 percent diameter reduction under steady condition for $T_{\kappa-\omega}$ model with $T_{int} = 0.1, 2.0$.

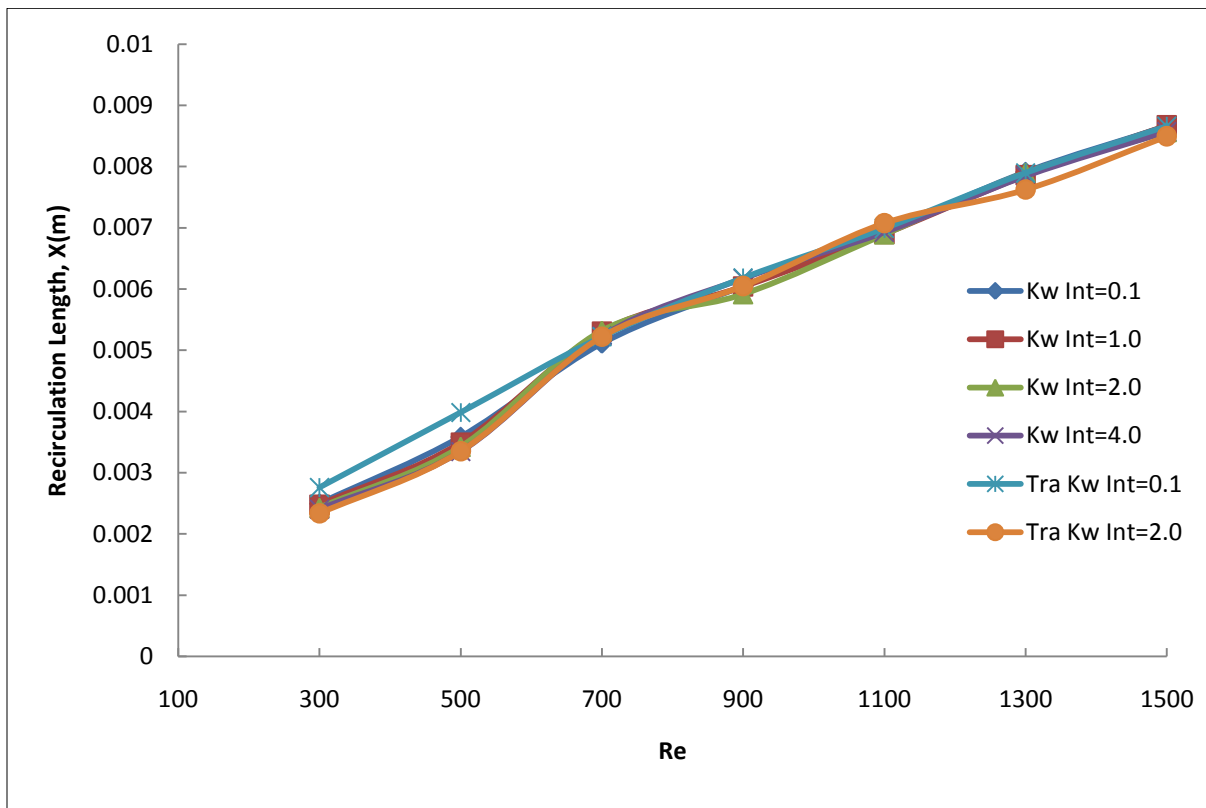


Figure 6.29 Comparison of recirculation length as a function of Reynolds number with 25 percent diameter reduction of $\kappa-\omega$ and $T_{\kappa-\omega}$ models with different turbulent intensities.

Validation for Pulsatile Flow Case

Figure 6.30 illustrates the WSS of a tapered stenosed artery with 50 percent diameter reduction. A tapered artery with 50 percent diameter reduction was simulated for $Re = 398$. The simulation was run for five different cycles. Results were drawn from the fifth cycle since by then the flow was properly developed.

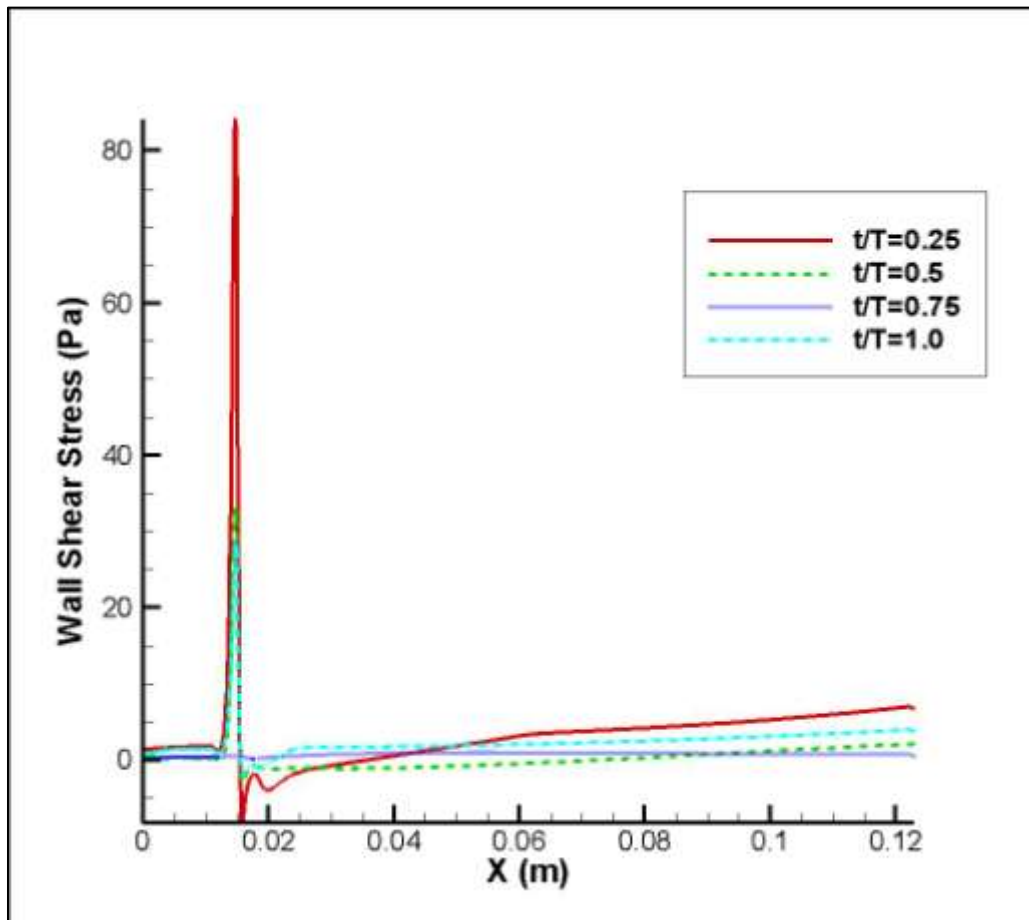


Figure 6.30 Validation for pulsatile case.

The inlet flow imposed was sinusoidal with a Womersley frequency of 6.1. The model used for validation was model 5 of the work by Dietiker and Hoffmann [67] and Liu et al. [68]. The WSS at the four different time intervals did not match with the original numerical simulation. Liu et al. simulated model 5 in 2-D, and Dietiker and Hoffmann simulated the same

model in 3-D. The WSS of Dietiker and Hoffmann did not match with the results of Liu et al. The correct answer is still unknown but Dietiker and Hoffmann stated that the difference in WSS was due to the 3-D effects. Even the WSS of the simulation in this thesis did not match with the WSS of Dietiker and Hoffmann and Liu et al. The pattern of WSS obtained by Dietiker and Hoffmann did not match with the pattern of WSS obtained by Liu et al. The pattern of WSS illustrated by Liu et al. matched with the pattern of WSS in this simulation. All parameters, such as the geometric model, inlet, and outlet boundary conditions, were similar to those by Dietiker and Hoffmann [67] and Liu et al. [68]. To further verify the results, the outlet length was almost doubled, but the pattern and magnitude of WSS were kept the same. No change in WSS and pattern was observed. The grid size was also doubled, and a denser grid was employed at the wall. Again, no significant change was observed. The inlet user-defined function was the same as used by Dietiker and Hoffmann, which was a sine wave. The frequency was on the upper range of a human heart beat, but this was just an approximation. Since the WSS pattern in this thesis investigation was similar to the one by Liu et al. [68], the results were considered to truly represent the WSS of stenosed tapered artery in 3-D. The difference in WSS may be attributed to the 3-D effects taking place. To date, no other data is available to validate the experimental and numerical results for a stenosed tapered artery. Because of this, the results obtained by the current validation may be considered a benchmark.

Pulsatile Flow

As discussed previously, for a tapered stenosed artery, no experimental results are available for unsteady pulsatile flow. Liu et al. was the first to simulate the tapered stenosed artery with unsteady pulsatile flow in 2-D. Dietiker and Hoffmann simulated the geometry of Liu et al. in 3-D and published the results. Both researchers used a pulsatile wave form at the inlet as

discussed in Section 4.3 of Chapter 4. The other conditions used in this thesis simulation were the same as used by Dietiker and Hoffmann [67] and Liu et al. [68]. The inlet UDF was the same as used by Dietiker and Hoffmann, and was a sine wave, which is a long distance from the actual wave form of a human heart. The investigation in this thesis focused on reproducing the results found by Dietiker and Hoffmann [67] and Liu et al. [68]. The κ - ω model was used for the current unsteady pulsatile simulation. The simulation for the tapered stenosed artery was run at Reynolds numbers ranging from 100 to 1500 at a turbulent intensity of 0.1. The simulation for AAA was run at $Re = 396$, also at a turbulent intensity of 0.1. The pressure at the outlet was defined to be zero. The pressure difference between the inlet and outlet drove the blood flow.

Figures 6.31 to 6.34 show the comparison of all shear stress at Reynolds numbers ranging from 100 to 1500. Results here are discussed for four time intervals: $t/T = 0.0, 0.25, 0.75,$ and 1.0 . Figure 6.31 represents WSS at $t/T = 0.25$ when the flow begins to accelerate from $t/T = 0.0$. The WSS increased to the maximum positive value at the stenosis. It was also observed that soon after the stenosis, the wall shear stress changed its direction and attained a negative value. This clearly shows the flow separation as discussed by Dietiker and Hoffmann [67] and Liu et al. [68]. The region of separation between these two zero values was a negative WSS. At $t/T = 0.5$, the maximum positive WSS decreased, and the blood separation region increased. It can be seen that the WSS at $Re = 100$ was almost zero. At $t/T = 0.75$, the WSS showed a wavy pattern and oscillated, as can be seen in Figure 6.33. The WSS was negative in the entire region. During this time period, the flow was completely reversed from outlet to inlet. Figure 6.34 illustrates WSS at $t/T = 1.0$. The WSS magnitude was the same as shown in Figure 6.32 with slightly less WSS magnitude.

It can be observed in Figures 6.31 to 6.34 that WSS and flow do not have any effect upstream of the stenosis. Liu et al. mentioned the critical value of WSS to be 34.4 Pascals (344 Dyne /cm²). If the WSS goes beyond this critical value, then the endothelium may tear and formation of thrombosis may start, which later on may rupture from the wall and block other arteries, making the patient vulnerable to stroke. In this thesis investigation, WSS did overshoot the critical value, as shown in Figure 6.31, at $t/T = 0.25$ from Reynolds numbers 700 to 1500. Apart from causing wall damage and thickening of tunica intima, this high shear stress may even activate platelets, causing aggregation of platelets and ultimately the formation of thrombus, as discussed in Chapter 1 when describing the high-blood-flow theory.

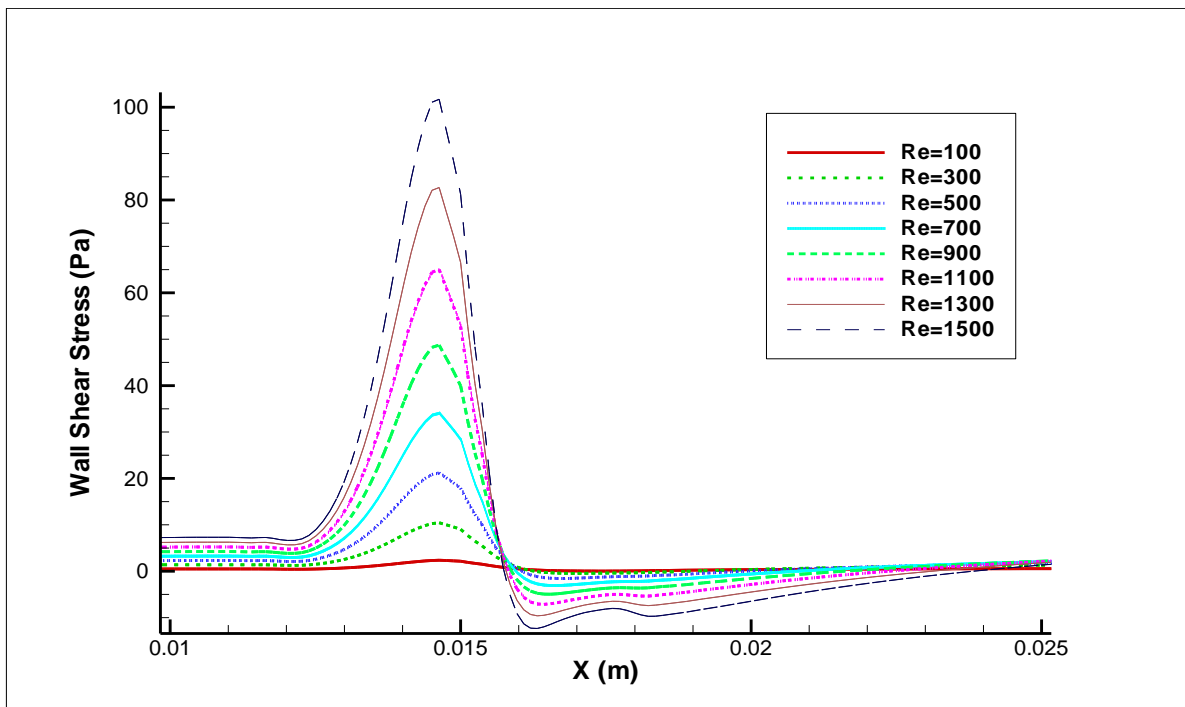


Figure 6.31 Comparison of WSS using unsteady κ - ω model with $T_{int} = 0.1$ at $t/T = 0.25$.

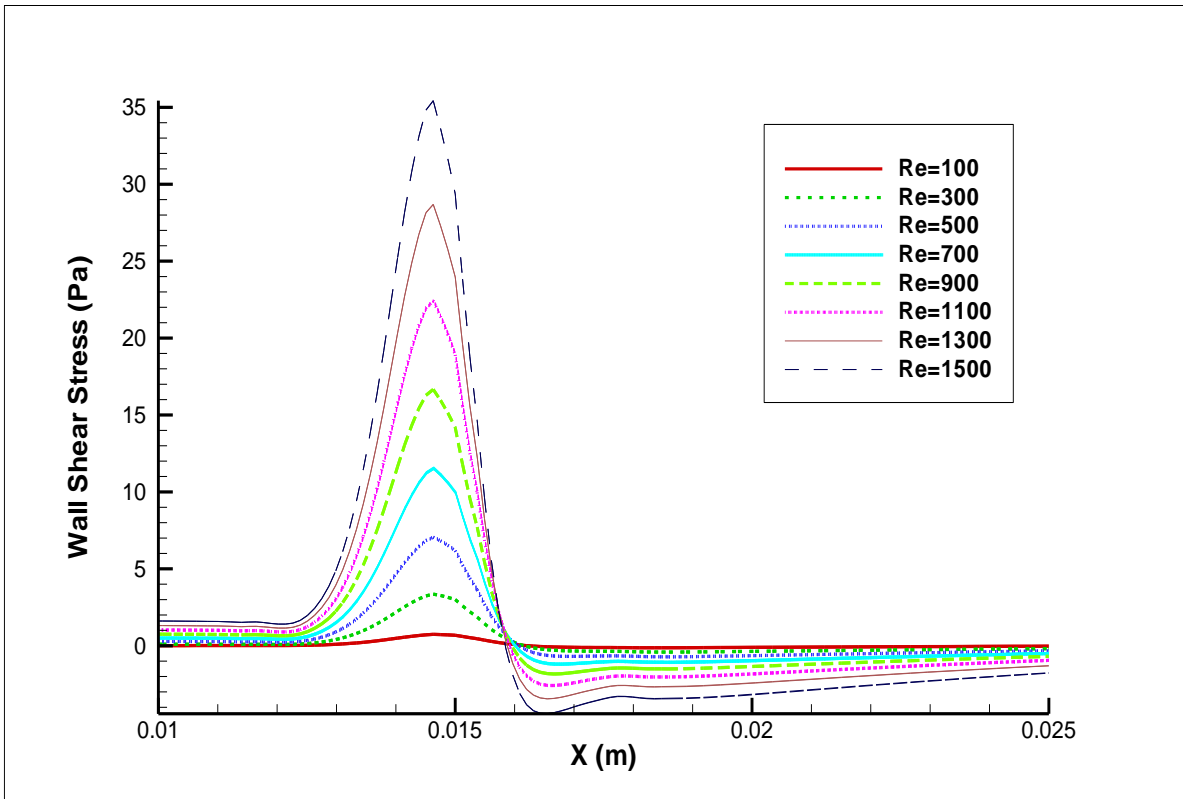


Figure 6.32 Comparison of WSS using unsteady κ - ω model with $T_{int} = 0.1$ at $t/T = 0.5$.

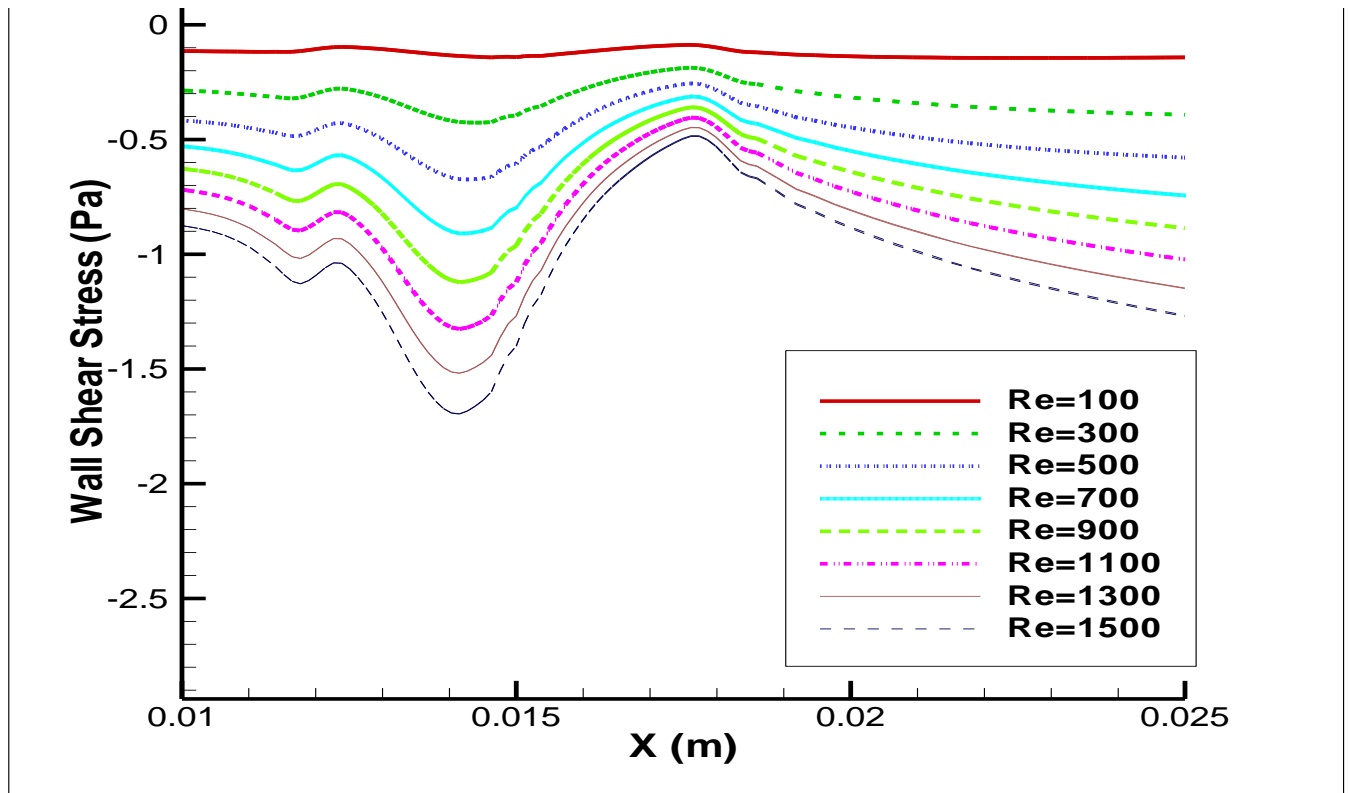


Figure 6.33 Comparison of WSS using unsteady κ - ω model with $T_{int} = 0.1$ at $t/T = 0.75$.

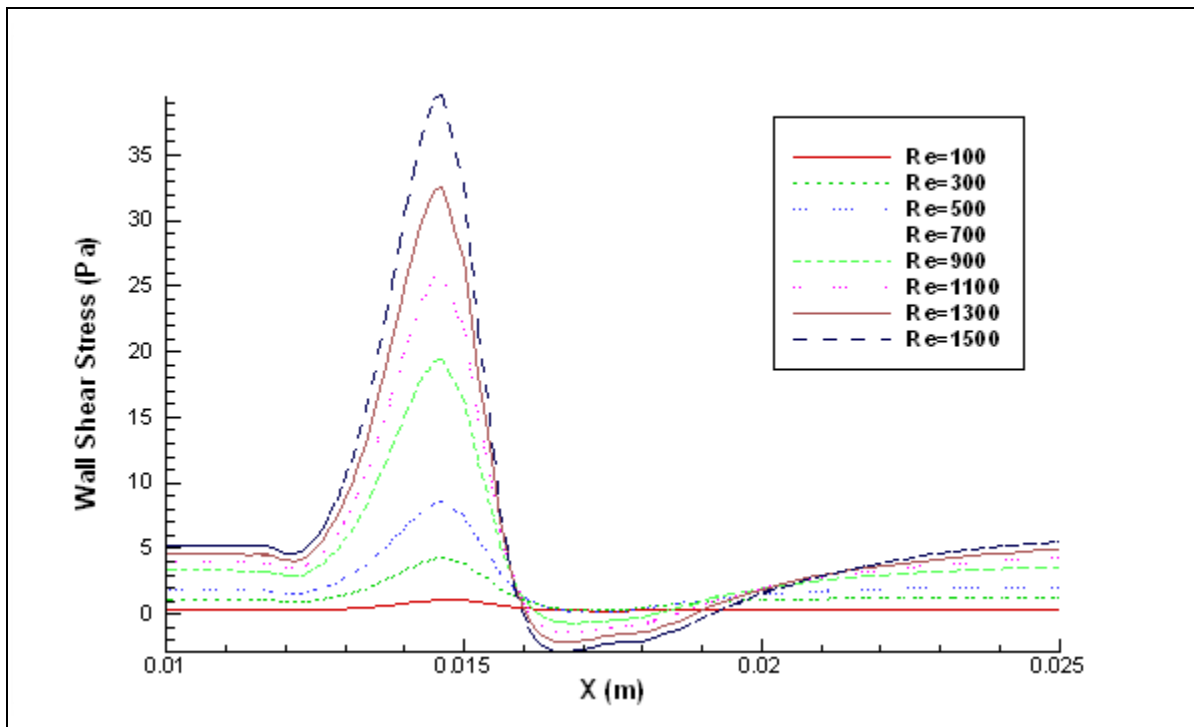


Figure 6.34 Comparison of WSS using unsteady κ - ω model with $T_{int} = 0.1$ at $t/T = 1.0$.

The unsteady simulation of AAA was done at $Re = 396$ using the κ - ω model. Figures 6.35 to 6.38 represent the WSS of AAA at four different time intervals. The pulsatile flow is sinusoidal as discussed in equation 4.20. Figure 6.35 represents the WSS at $t/T = 0.25$. It is noted that the wall shear stress drops abruptly at the bulged region of the aneurysm. The magnitude of WSS goes to negative region at the center of the aneurysm and then again WSS increases. Budwig et al. [43] reported that an aneurysm has two peaks of WSS: one at the flow separation and the other at the point where the flow reattaches. The same phenomenon was observed in this thesis investigation. The peak in WSS at the separation had a lower magnitude than at the place where the flow reattached. WSS at $t/T = 0.5$ followed a pattern similar to at $t/T = 0.25$, but it had a lower magnitude for WSS as shown in Figure 6.36. Figure 6.37 illustrates the WSS at $t/T = 0.75$. Figure 6.37 has two WSS lines, which is due to some of the default settings in Tecplot 360.

In fact, there should be only one line. Effort was made to extract the correct data and plot a graph with a single line, but the effort was unsuccessful. At this time period, the flow completely reversed from the outlet to the inlet. This effect can be seen in Figures 6.41 and 6.42. The WSS was negative at the wall surface throughout, which represents the flow reversal. WSS at $t/T = 1.0$ is illustrated in Figure 6.38. The flow was laminar and no separation or reversal was observed. For the steady case, Scherer [90] noted that the shear stress in the recirculation zone was ten times more than the inlet length. Similar results were obtained in this investigation at $t/T = 0.25$ when the flow was not fully developed and laminar. At time interval $t/T = 0.5$, the inlet length shear stress was six times more than the shear stress in the recirculation region. Results show the negative shear stress at $t/T = 0.25, 0.5, \text{ and } 0.75$. WSS was found to be oscillating throughout the aneurysm region. The oscillating shear stress was correlated with the oscillating velocity and time period. In this investigation, the WSS did not exceed the critical value of WSS at the described Reynolds number.

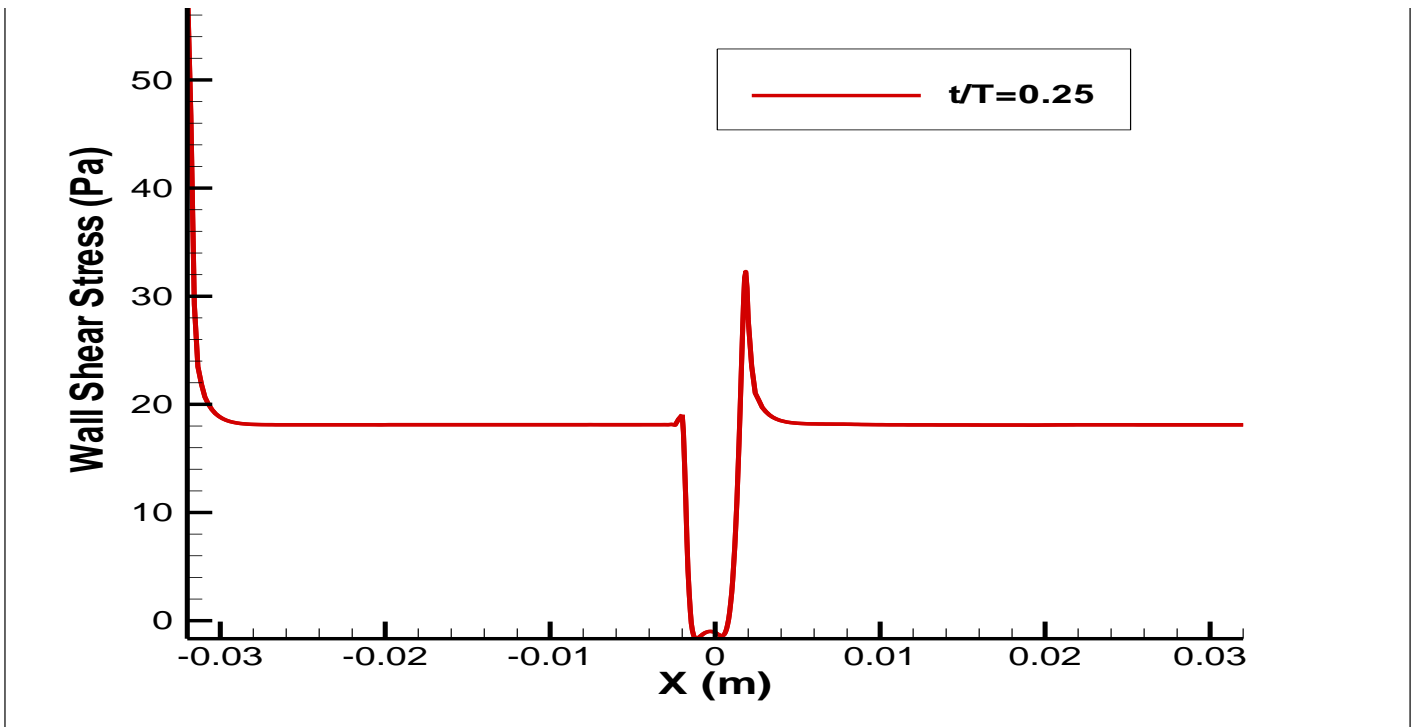


Figure 6.35 WSS of AAA using unsteady $\kappa\text{-}\omega$ model with $T_{\text{int}} = 0.1$ at $t/T = 0.25$.

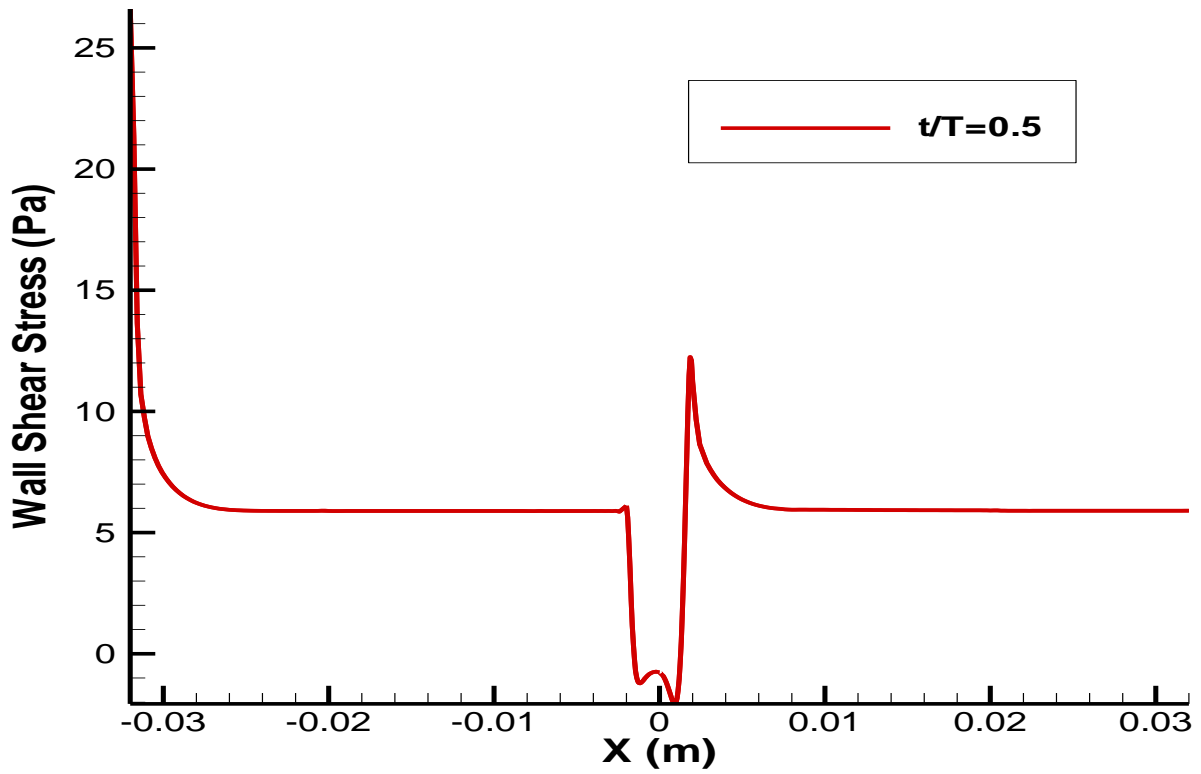


Figure 6.36 WSS of AAA using unsteady κ - ω model with $T_{int} = 0.1$ at $t/T = 0.5$.

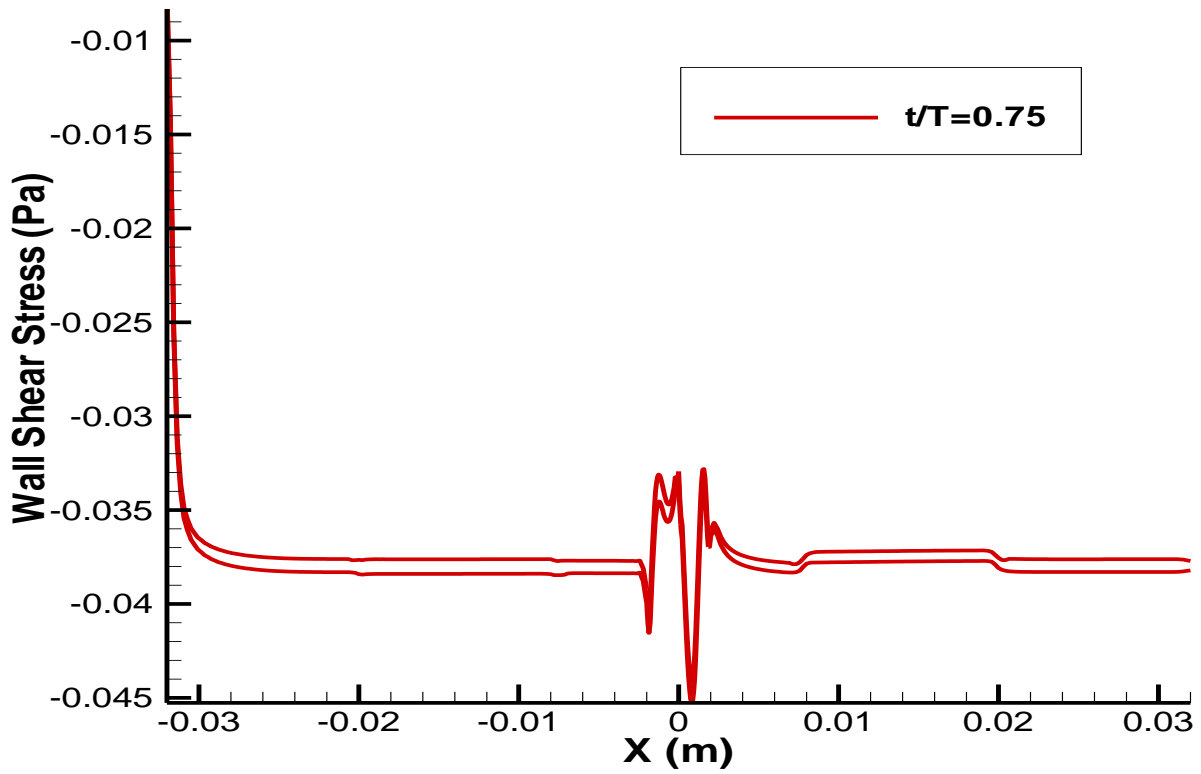


Figure 6.37 WSS of AAA using unsteady κ - ω model with $T_{int} = 0.1$ at $t/T = 0.75$.

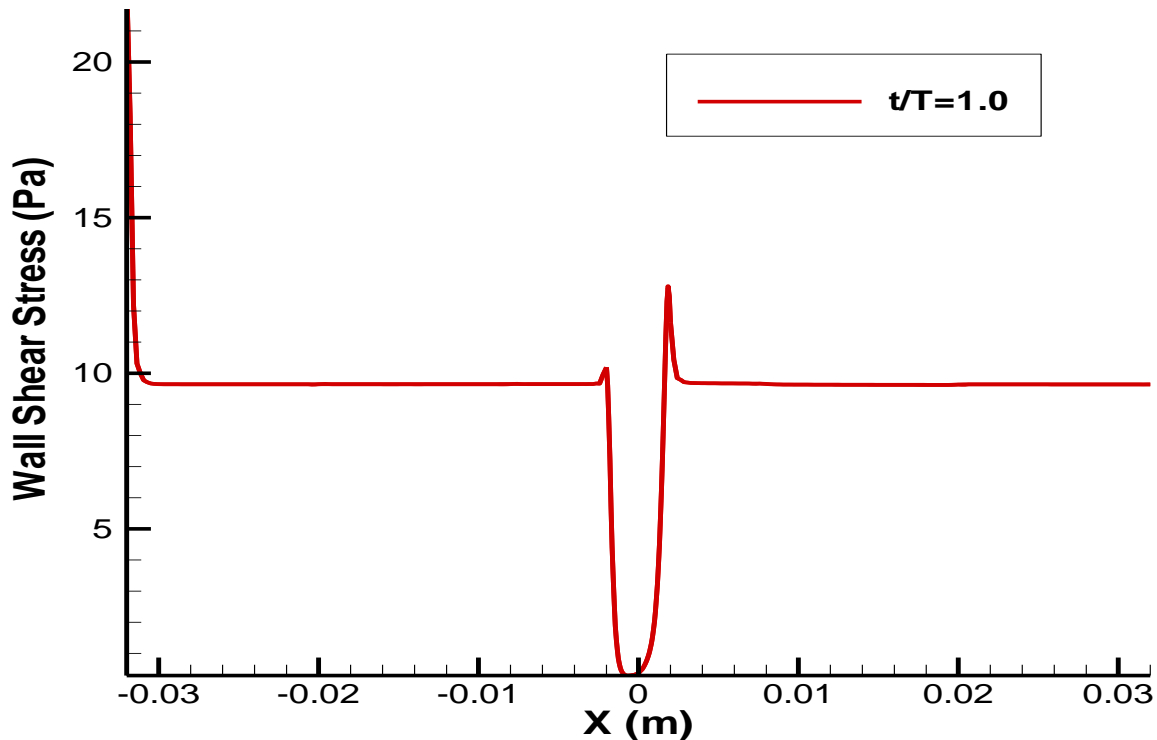


Figure 6.38 WSS of AAA using unsteady $\kappa\text{-}\omega$ model with $T_{\text{int}} = 0.1$ at $t/T = 1.0$.

Figures 6.39 to 6.43 represent the X-velocity contour and the streamlines for the blood flow using the unsteady $\kappa\text{-}\omega$ model. Figure 6.39 illustrates the X-velocity contour and streamlines for $t/T = 0.25$. It can be seen that flow separation begins where the bulging of the artery begins. Again, the flow reattaches before the bulging ends. This area is completely under the negative shear stress and low velocity.

Figure 6.40 represents the X-velocity contour and streamlines for $t/T = 0.5$. The flow separation is clearly visible, indicating that the flow reattachment was further from the place where it reattached in Figure 6.39. The separation bubble was constrained within the aneurysm and did not travel further downstream.

Figures 6.41 and 6.42 illustrates the X-velocity contour and streamlines for $t/T = 0.75$ where the flow completely reversed from outlet to inlet, and all surfaces of the artery were under negative shear and WSS. The flow was very complicated in the bulged region. At the center, the

velocity was from the outlet to the inlet, and at the top and bottom, the velocity was from the outlet to the inlet. The separation bubble lay between these two flow patterns, while the top of the separation bubble had flow from the outlet to the inlet, the bottom of the separation bubble had flow from the inlet to the outlet. This pattern tried to break the bubble and further complicate the flow.

The X-velocity contour and streamlines for $t/T = 1.0$ are shown in Figure 6.43. As can be seen, the flow was laminar and had no separation bubble. The flow was also unidirectional. Budwig et al. [43] reported that the center of the vortex traveled downstream from the proximal to the distal end of the aneurysm within the time period. Comparing the figures reveals the same pattern. The flow in Figure 6.43 is characterized by a jet of fluid passing through the vortex bubbles in an aneurysm region. It is noted that the minimum high shear stress peak in the diverging section of the aneurysm is due to deceleration of the local velocity, and the maximum shear stress peak at the reattachment point in the converging section of aneurysm is due to the acceleration of the local velocity in the aneurysm.

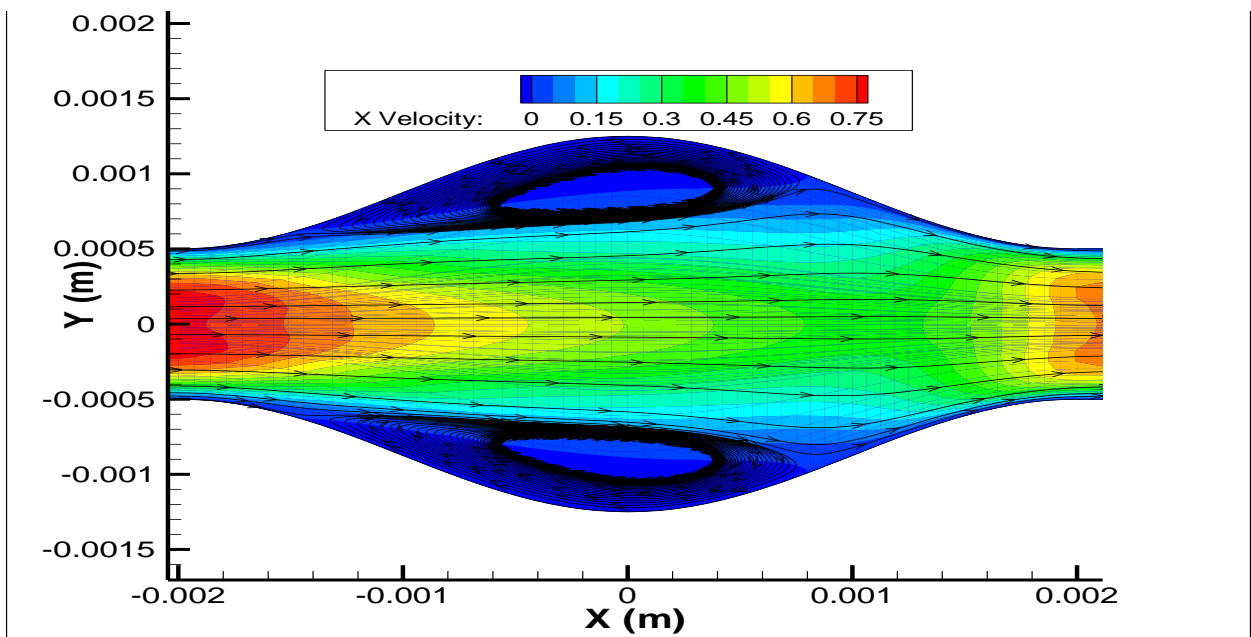


Figure 6.39 X-velocity contour and streamlines for $t/T = 0.25$.

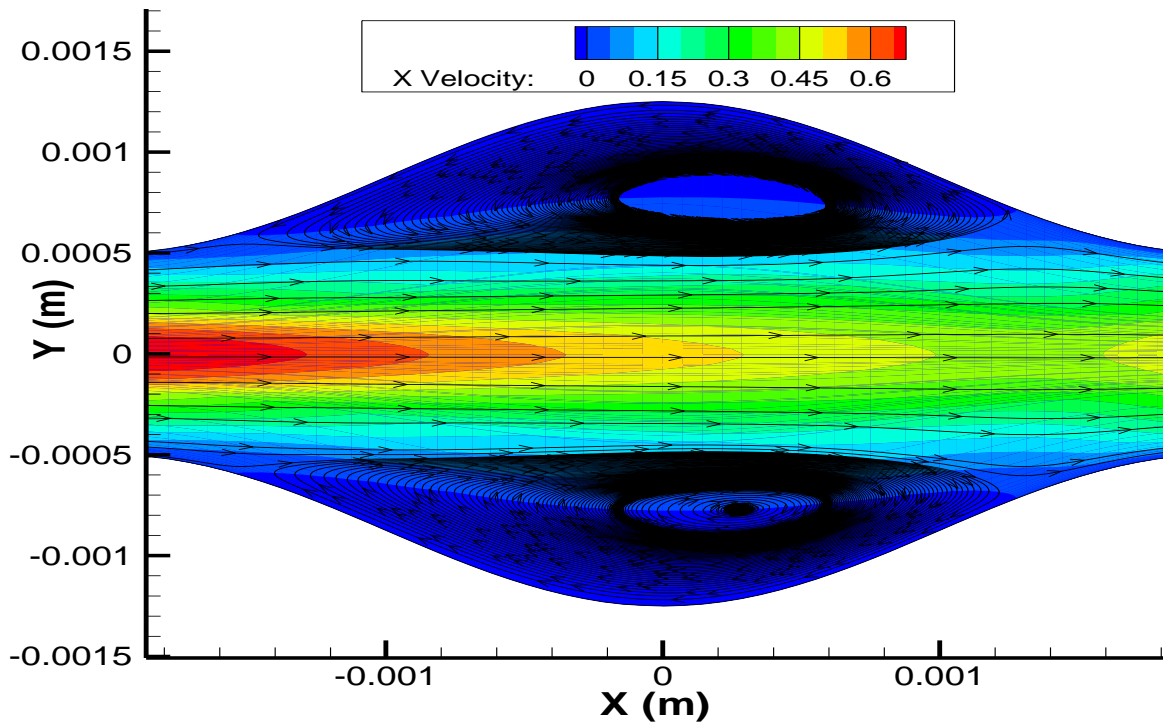


Figure 6.40 X-velocity contour and streamlines for $t/T = 0.5$.

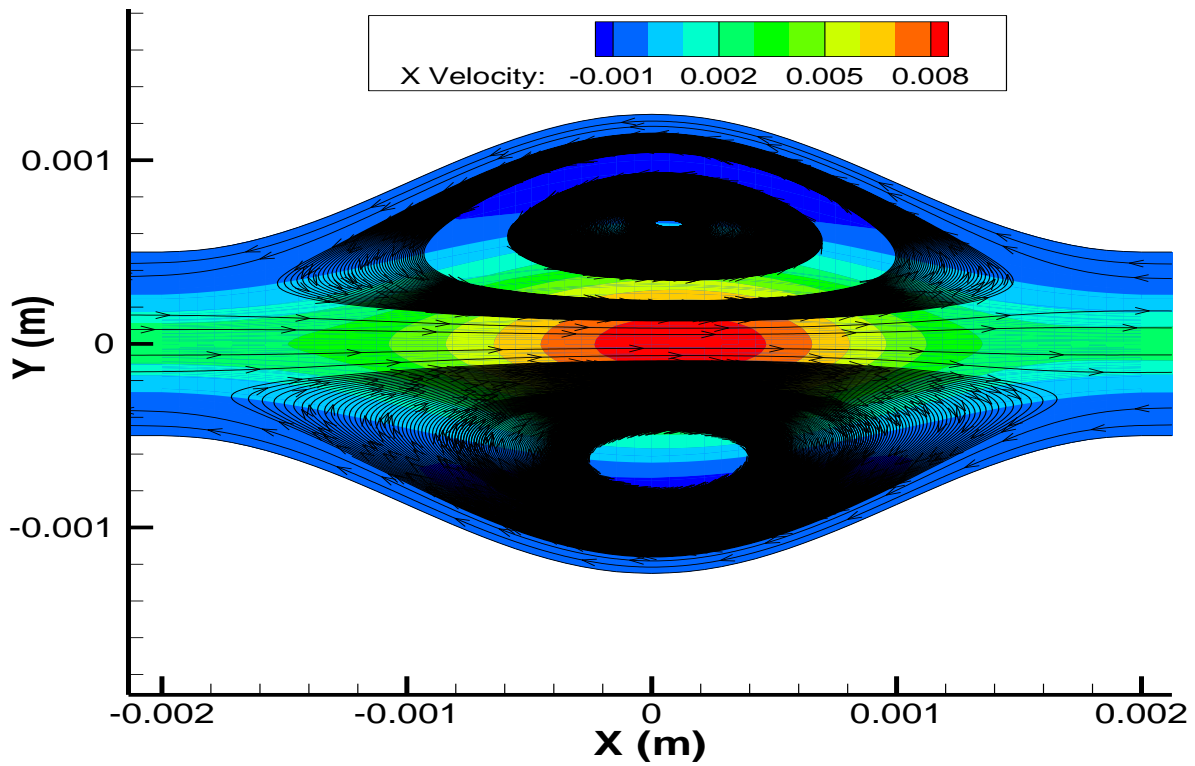


Figure 6.41 X-velocity contour and streamlines for $t/T = 0.75$.

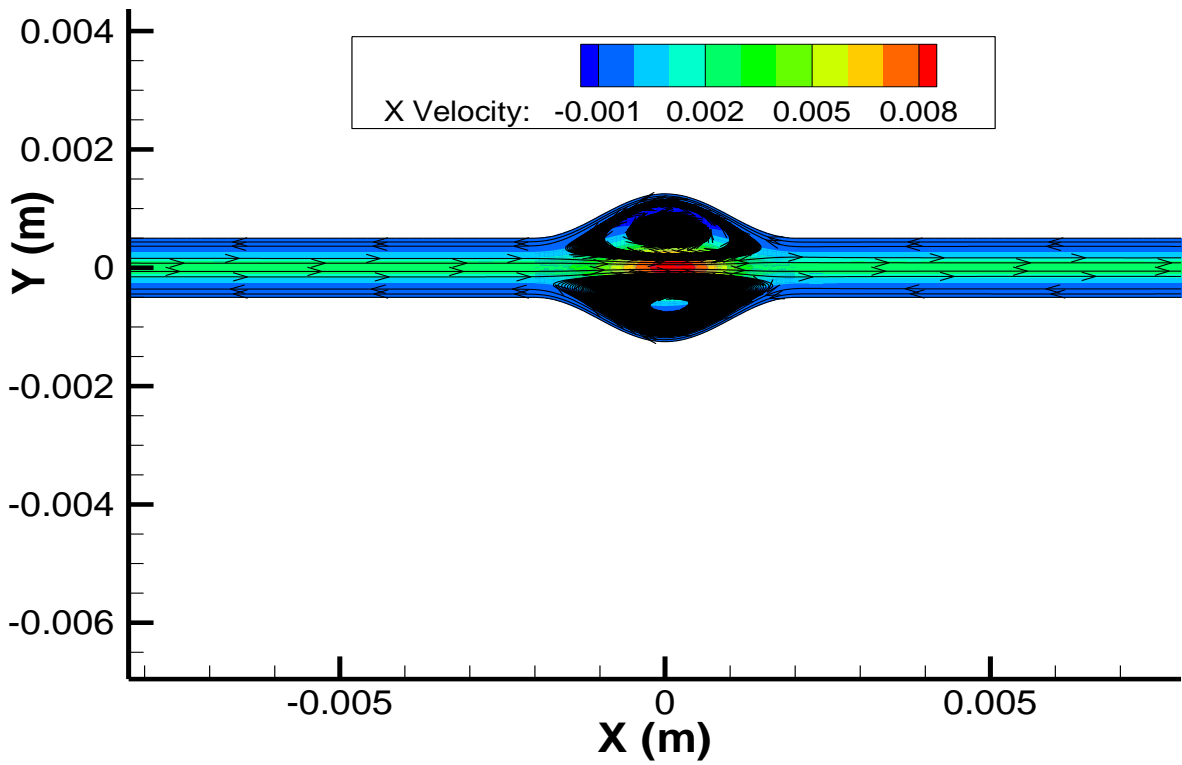


Figure 6.42 Schematic of geometry showing X-velocity contour and streamlines for $t/T = 0.75$.

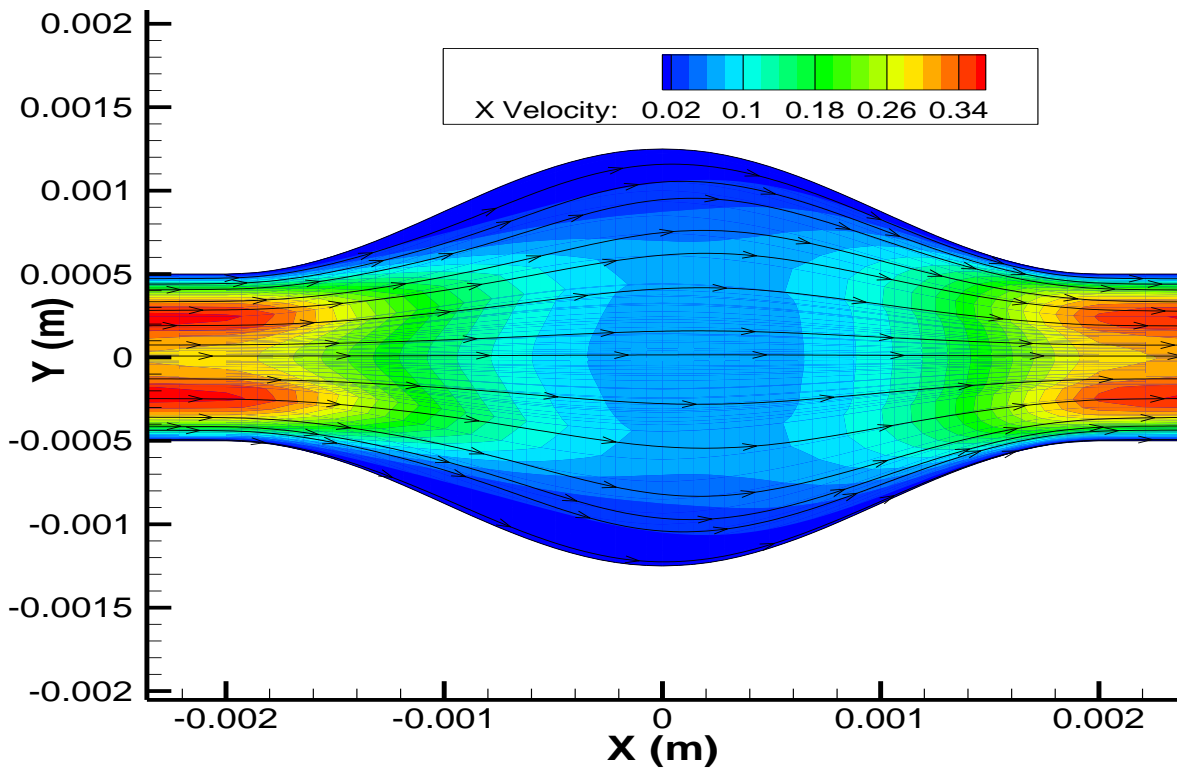


Figure 6.43 X-velocity contour and streamlines for $t/T = 1.0$.

CHAPTER 7

CONCLUSIONS

This study was undertaken to understand the flow behavior in a tapered stenosed artery, since many arteries in the human body are tapered. Systematic investigation of flow behavior was done by using the simple $\kappa\text{-}\omega$ model and transitional versions of the $\kappa\text{-}\omega$ models to determine the effect of each model in a tapered artery with stenosis. The unsteady simulation using the $\kappa\text{-}\omega$ model was run to obtain the pulsatile flow results. Great care was taken because the results obtained are very grid sensitive. A comparison of the experimental data and numerical data was done for validation of the steady case. No experimental data was available for the pulsatile case validation. Compared to the previous 2-D results, the WSS results did not match, which may be attributed to 3-D effects.

Concluding Remarks for Stenosed Tapered Artery

For steady cases, both the simple $\kappa\text{-}\omega$ and transitional version of the $\kappa\text{-}\omega$ model were simulated for a tapered artery with 25 percent stenosis. Results were compared for WSS and recirculation length after the stenosis. The recirculation length was found to be the same in both models. No significant differences in results were noted. Therefore, it can be concluded that in a tapered artery, both the $\kappa\text{-}\omega$ and transitional $\kappa\text{-}\omega$ behave in the same way. A 25 percent stenosed artery was simulated using the simple $\kappa\text{-}\omega$ model having a turbulent intensity of 0.1, 1.0, 2.0 and 4.0. No change in the wall shear stress was reported in this investigation. Therefore, it can be concluded that the increase in turbulent intensity has no effect on the wall shear stress and recirculation length. As the Reynolds number increased in the simple $\kappa\text{-}\omega$ and transitional $\kappa\text{-}\omega$ models, the length of recirculation also increased.

For the unsteady case, only the simple $\kappa\text{-}\omega$ model was simulated for Reynolds numbers ranging from 100 to 1500 at a turbulent intensity of 0.1. The wall shear stress pattern was plotted at intervals of $t/T = 0.25, 0.5, 0.75,$ and 1.0 . The shear stress steadily increased with the increase in the Reynolds number. Flow reversal was noted in $t/T = 0.25, 0.5,$ and 0.75 . The flow was laminar at $t/T = 1.0$. WSS higher than 34.4 Pascals can break the endothelium. At a higher Reynolds number, the WSS overshoots 34.4 Pascals at $t/T = 0.25$. At $t/T = 0.75$, the WSS was negative. The artery was constantly under oscillating shear, which may damage the endothelium.

From this investigation, it can be concluded that both the $\kappa\text{-}\omega$ and transitional version of the $\kappa\text{-}\omega$ model predict the same behavior in a tapered stenosed artery. Both models are promising for simulating steady flow in a tapered stenosed artery. Before using this model, the user needs to thoroughly understand the model and its limitations, cases where it yields the best results and cases where it underpredicts results.

Conclusion for Abdominal Aortic Aneurysm

Only one case was run for the abdominal aortic aneurysm using the simple $\kappa\text{-}\omega$ model. The bulged area of the aneurysm remained constant under low shear stress, as can be seen in the velocity contours and wall shear stress plots. The recirculation bubble did not travel downstream. It was trapped within the bulged region. This lower shear stress may further worsen the walls of the aneurysm and start adhesion of platelet deposition on the wall.

CHAPTER 8

FUTURE RECOMMENDATIONS

An experimental study should be carried out to compare this investigation's numerical results with the experimental results.

It is recommended that the tapered artery be simulated with real-life conditions and that the boundary conditions be defined as they occur in real life.

Rather than considering both the aneurysm and the tapered artery to be rigid, a simulation could involve a flexible artery.

Also, a tapered artery with severe stenosis could be simulated to study the initiation of turbulence and transition from laminar flow to turbulent flow.

Since no experimental results show certainty, it is recommended that higher turbulence models such as LES and RANS be simulated for further verification. For higher-turbulence model simulation, the computational cost involved would be more and the time consumed would be much greater. Therefore, the two-equation κ - ω model should be used first.

It is also recommended to simulate the non-symmetric aneurysm and stenosis using various turbulence models, since in an actual case, both diseases grow asymmetrically.

REFERENCES

REFERENCES

- [1] <http://www.who.int/whr/2004/en/index.html> [cited 15th July 2008].
- [2] Heart Disease and Stroke Statistics, American Heart Association. <http://www.americanheart.org/presenter.jhtml?identifier=3000090> [cited 17th September 2010, Data subjected to change with the updating of the report]
- [3] Vital Statistics of the U.S., Data Warehouse, NCHS, <http://www.cdc.gov/nchs/datawh.htm> [cited 7th August 2009]
- [4] Chugh, S. S., Jui, J., Gunson, K., et. al., –Current burden of sudden cardiac death: Multiple source surveillance retrospective death certificate-based review in large US community,” *J. Am. Coll. Cardio.*, Vol. 44, 2004, pp. 1268-1275.
- [5] Greenland, P., Deloria, M., Stamler, J., Newton, J. D., et. al., –Major risk factors as antecedents of fatal and nonfatal coronary heart disease events,” *JAMA*, Vol. 290, 2003, pp. 891-897.
- [6] Fields, L. E., Burt, V. L., Cutler, J. A., et. al., –The burden of adult hypertension in the United States 1999 to 2000: A rising tide,” *Hypertension*, Vol. 44, 2004, pp. 398-404.
- [7] Hoffman, J. I., Kaplan S., Liberthson, R. R., –Prevalence of congenital heart disease,” *Am. Heart Journal*, Vol. 147, 2004, pp. 425-439.
- [8] www.hcup.ahrq.gov/HCUPnet.jsp. [cited 23rd september 2009]
- [9] Karino, T., and Goldsmith, H. L., –Aggregation of human platelets in an annular vortex distal to a tubular expansion,” *Microvasc. Res.*, Vol. 17, 1979, pp. 217-237.
- [10] Ku, D. N., and Giddens, D. P., –Pulsatile flow visualization in carotid artery,” *Arteriosclerosis*, Vol. 3, 1983, pp. 31-39.
- [11] Ohja, M., Ethier, C. R., and Johnston, K. W., 1990. –Steady and pulsatile flow fields in an end-to-side anastomosis model,” *J. Vasc. Surg.*, Vol. 12, 1990, pp. 747-753.
- [12] Keynton, R. S., Rittgers, S. E., and Shu, M. C., –The effect of angle and flow upon hemodynamics in distalvascular graft anastomoses: as in vitro study,” *J. Biomech. Eng.*, Vol. 113, 1991, pp. 458-464.
- [13] Nerem, R. M., and Seed, W. A., –An in vivo study of aortic flow disturbances,” *Cardiovascu.Res.*, Vol. 6, 1972, pp. 1-14.

REFERENCES (continued)

- [14] Friedman, M. H., Barger, C. B., Hutchins, G. M., Mark, F. F., and Deters, O. J., "Hemodynamics measurements in human arterial casts and their correlation with histology and luminal area," *J. Biomech. Eng.*, Vol. 102, 1980, pp. 247-251.
- [15] Khalifa, A. M. A., and Giddens, D. P., "Characterization and evolution of post stenotic flow disturbances," *J. Biomech.*, Vol. 14, 1981, pp. 279-296.
- [16] Ku, D. N., and Giddens, D. P., 1987. "Laser Doppler anemometer measurements of pulsatile flow in a model carotid bifurcation," *J. Biomech. Eng.*, Vol. 20, pp. 407-420.
- [17] Meier, D., Maier, S., and Boesiger, P., 1988. "Quantitative flow measurement on phantoms and on blood vessels with MR," *Mag. Reson. Med.*, Vol. 8, 1988, pp. 25-34.
- [18] Kim, W. Y., Walker, P. G., Pedersen, E. M., Poulsen, J. K., and Oyre, S., "Left ventricular blood flow patterns in normal subjects: a quantitative analysis by three-dimensional magnetic resonance velocity mapping," *J. Am. Coll. Cardiol.*, Vol. 26, 1995, pp. 224-238.
- [19] Ku, D. N., Zarins, C. K., Giddens, D. P., and Glagov, S., 1985b. "Pulsatile flow and atherosclerosis in the human carotid bifurcation: positive correlation between plaque localization and low and oscillating shear stress," *Arteriosclerosis*, Vol. 5, 1985b, pp. 292-302.
- [20] Moore, J. E. Jr., Maier, S. E., Ku, D. N., and Boesinger, P., "Hemodynamics in the abdominal aorta: a comparison of in vitro and in vivo measurements," *J. Appl. Physiol.* Vol. 76, 1994b, pp. 1520-1527.
- [21] He, X., and Ku, D. N., 1996. "Pulsatility flow in the human left coronary artery bifurcation: Average conditions," *J. Biomech. Eng.*, Vol. 118, 1996, pp. 74-82.
- [22] https://www.nhlbi.nih.gov/health/dci/Diseases/Angioplasty/Angioplasty_All.html [cited 2nd February 2010]
- [23] Ku, D. N., and Allen, R. C., *Vascular Grafts in the Biomedical Engineering handbook*, 2nd ed., CRC Press Inc., Boca Raton, FL, 1995, pp. 1871, 1878.
- [24] Hofstra, L., Bergmans, D. C. J. J., and Hoeks, A. P. G., et al., "Mismatch in elastic properties around anastomosis of interposition grafts for hemodialysis access," *J. Amer. Soc. of Nephrol.*, Vol. 5, 2000, pp. 701-708.
- [25] Echave, V., Koornick, A. R., and Haimov, M., "Intimal hyperplasia as a complication of the use of the polytetrafluoroethylene graft for femoral-popliteal bypass," *Surgery*, Vol. 86, 1979, pp. 791-798.

REFERENCES (continued)

- [26] Carrel, A., and Guthrie, C. C., —Anastomosis of blood vessels by the patching method and transplantation of the kidney,” *JAMA*, Vol. 47, 1906, pp. 1648-1650.
- [27] Carrel, A., and Guthrie, C. C., —The transplantation of veins and organs,” *American Medicine*, Vol. 10, 1905, pp. 300-309.
- [28] Lemson, M. S., Tordoir, J. H. M., Daemen, M. J. A. P., and Kitslaar, P. J. E. H. M., —Intimal hyperplasia in vascular grafts,” *Eur. J. Vasc. Endovasc. Surg.*, Vol. 19, 2000, pp. 336-350.
- [29] Ender, A. F, and Cristina, H., —Blood flow in abdominal aortic aneurysms: Pulsatile flow in hemodynamics,” *J. Biomech. Eng.*, Vol. 123, 2001, pp. 474-484.
- [30] Newman, A. B., Arnold, A. M., Burke, G. L., O’leary, D. H., and Manolio, T. A., —Cardiovascular disease and mortality in older adults with small abdominal aortic aneurysms detected by ultra sonography,” *Ann. Intern med.*, Vol. 134, 2001, pp. 182-190.
- [31] Quill, D. S., Colgan, M. P., and Sumner, D. S. —Ultrasonic screening for the detection of abdominal aortic aneurysms,” *Surg. Clin. North Am.*, Vol. 69, 1989, pp. 713-720.
- [32] Taylor, L. M., and Porter J. M., —Basic data related to clinical decision making in Abdominal Aortic Aneurysms,” *Ann. Vas. Surg.*, Vol. 1, 1986, pp. 502-504.
- [33] Armor, R. H., —Survivors of ruptured abdominal aortic aneurysms: The iceberg’s tip,” *Br. Med. J.*, Vol. 2, 1977, pp. 1055-1057.
- [34] Johannson, G., and Swedenborg, J., —Ruptured abdominal aortic aneurysms: A study of incidence and mortality,” *Br. Med. J.*, Vol. 73, 1986, pp. 101-103.
- [35] Nevitt, M. P., Ballard, D. J., and Hallett, J. W., —Prognosis of abdominal aortic aneurysms: A population based study,” *N. Eng. J. Med.*, Vol. 321, 1989, pp. 1009-1014.
- [36] Szilagyi, D. E., Smith, R. F., DeRusso, F. J., Elloit, J. P., and Sherrin, F. W., —Contribution of abdominal aortic aneurysm-ectomy to prolongation of life,” *Ann. Surg.*, Vol. 64, 1966, pp. 678-699.
- [37] Darling, R. C., —Ruptured arteriosclerotic abdominal aortic aneurysms: A pathologic and clinical study,” *Am. J. Surg.*, Vol. 119, 1970, pp. 397-401.
- [38] Willie, S., —Pulsatile pressure and flow in an arterial aneurysm simulated in a mathematical model,” *J. Biomech. Eng.*, Vol. 3, 1981, pp. 153-158.

REFERENCES (continued)

- [39] Perktold, K., Gruber, K., Kener, T., and Florian, H., "Calculation of pulsatile flow and particle paths in an aneurysm models," *Basic Res. Cardiol.*, Vol. 79, 1984, pp. 253-261.
- [40] Perktold, K., "On the paths of fluid particles in an axisymmetrical aneurysm," *J. Biomech.*, Vol. 20, 1987, pp. 311-417.
- [41] Fukushima, T., MatsU.S.wa, T., and Homma, T., "Visualization and finite element analysis of pulsatile flow in models of the abdominal aortic aneurysms," *Biorheology*, Vol. 26, 1989, pp. 109-130.
- [42] Elger, D., Slippy, J., Budwig, R., Khraishi., T., and Johnson, K., "A Numerical study of the hemodynamics and in a model abdominal aortic aneurysm (AAA)," *Proc. ASME Symposium on Biomedical Fluids Engineering*, R. A. Gerbsch and K. Ohba, eds., ASME FED- Vol. 212, 1995, pp. 15-22.
- [43] Budwig, R., Elger, D., Hooper, H., and Slippy, J., "Steady flow in abdominal aortic aneurysm models," *J. Biomech. Eng.*, Vol. 115, 1993, pp. 418-423.
- [44] Graboswki, E., 1995, "Thrombosis flow and vessel wall interactions," *J. Vascular Interventional Radi.*, Vol. 6, No. 2, 1995, pp. 25S-29S.
- [45] Fox J. L., and Hugh A. E., "Location of atheroma: a theory based on boundary layer separation," *Br. Heart. J.*, Vol. 26, 1996, pp. 288-299.
- [46] Glagov, S., Zarins, C. K., Giddens, D. G., and Ku, D. N., "Hemodynamics and atherosclerosis, insights and perspectives gained from studies of human arteries," *Arch. Pathol. Lab. Med.*, Vol. 112, 1988, pp. 1018-1031.
- [47] Hademoenos, G. J., "The physics of cerebral aneurysms," *Phys. Today*, Vol. 48, 1995, pp. 24-30.
- [48] Lei, M., Kleinstreuer, D. P., Zarins, C. K., and Glagov, S., "Pulsatile flow and atherosclerosis in the human carotid bifurcation: positive correlation between plaque location and low oscillating stress," *Atherosclerosis*, Vol. 5, 1995, pp. 293-302.
- [49] Malek. M., Alper, S. L., and Izumo, S. "Hemodynamics shear stress and its role in atherosclerosis," *JAMA*, Vol. 282, 1999, pp. 2035-2042.
- [50] Pedersen, E., Sung. H., Burlson, A., and Yoganathan., "Two dimensional velocity measurement in a pulsatile flow models of normal abdominal aortic stimulating different hemodynamic conditions," *J. Biomech.*, Vol. 26, 1993, pp. 1237-1247.
- [51] Soliman. E., "Cerebral aneurysm," *eMED. Jou.*, Vol. 2, No. 9, 2001.

REFERENCES (continued)

- [52] Peattie, R. A., Riehel, T. J., and Bluth, E. I., "Pulsatile flow in fusiform models of abdominal aortic aneurysms: Flow fields, velocity patterns and flow-induced wall stresses," *J. Biomech. Eng.*, Vol. 126, 2004, pp. 438-446.
- [53] Stringfellow, M. M., Lawrence, P. F., and Stringfellow, R. G., "The influence of aorta-aneurysm geometry upon stress in the aneurysm wall," *J. Surg. Res.*, Vol. 42, 1987, pp. 425-433.
- [54] Elger, D. F., Blacketter, D. M., Budwig, R. S., and Johansen, K. H., "The influence of shape on the stresses in model abdominal aortic aneurysms," *J. Biomech. Eng.*, Vol. 118, 1996, pp. 326-332.
- [55] Vorp, D. A., Raghavan, M. L., and Webster, M. W., "Mechanical wall stress in abdominal aortic aneurysm: Influence of diameter and asymmetry," *J. Vasc. Surg.*, Vol. 27, 1998, pp. 632-639.
- [56] Ryval, J., Straatman, A. G., and Steinman, D. A., "Two- equation turbulence modeling of pulsatile flow in a stenosed tube," *J. Biomech. Eng.* Vol. 126, 2004, pp. 625-635.
- [57] Arteriosclerosis, "Report of the working group on arteriosclerosis of the national heart, lung and blood institute," NIH Publication No. 81-2304.
- [58] Feldman, C. L., and Stone, P. H., "Intravascular hemodynamic factors responsible for progression of coronary atherosclerosis and development of vulnerable plaque," *Curr. Opin. Cardiol.*, Vol. 15, No. 6, 2000, pp. 430-440.
- [59] Richardson, P. D., "Biomechanics of plaque rupture: Progress, problems and new frontiers," *Ann. Biomed. Eng.*, Vol. 30(4), 2002, pp. 524-536.
- [60] Stein, P. D., and Sabbah. H. N., "Turbulent blood flow in the ascending aorta of humans with normal and diseased aortic valves," *Circ. Res.*, Vol 39, No. 1, 1976, pp. 58-65.
- [61] Ghalichi, F., Deng, X., De Champlin, A., Douville, Y., King, M., and Guidon, R., "Low Reynolds turbulence modeling of blood flow in arterial stenosis," *Biorheology*, Vol. 35, Nos. 4 and 5, 1998, pp. 281-294.
- [62] Lee, T. S., Liao, W., and Low, H. T., "Numerical simulation of turbulent flow through series stenosis," *Int. J. Numer. Methods, Fluids*, Vol. 42, No. 7, 2003, pp. 717-740.
- [63] Ahmed, S. A., and Giddens, D. P., "Velocity measurements in steady flow through axisymmetric stenosis at moderate Reynolds number," *J. Biomech.*, Vol. 16, No. 7, 1983, pp. 505-516.

REFERENCES (continued)

- [64] Ahmed, S. A., and Giddens, D. P., "Flow disturbance measurements through a constricted tube at moderate Reynolds number," *J. Biomech.*, Vol. 16, No. 12, 1983, pp. 955-963.
- [65] Deshpande, M. D., and Giddens, D. P., "Turbulence measurements in a constricted tube," *J. Fluid. Mech.*, Vol. 97, 1980, pp. 65-89.
- [66] Stroud, J. S., Berger, S. A., and Saloner D., "Numerical analysis of flow through a severely stenotic carotid artery bifurcation," *J. Biomech. Eng.*, Vol. 124, No. 1, 2002, pp. 9-20.
- [67] Dietiker, J. F., and Hoffmann, K. A., "Computation of three dimensional blood flow in arteries," *36th AIAA Fluid Dynamics Exhibit and conference*, 2006-3213, pp. 1-15.
- [68] Liu, G. T., Wang, X. J., Ai, B. Q., and Liu, L. G., "Numerical study of pulsating flow through a tapered artery with stenosis," *Chinese J. of Physics*, Vol. 42, No. 4-I, 2004, pp. 401-409.
- [69] Fry, D. L., "Acute vascular endothelial changes associated with increased blood velocity gradients," *Circ Res.*, Vol. 22, 1968, pp. 165-197.
- [70] Fry, D. L., "Certain histological and chemical responses of the vascular interface to acutely induced mechanical stress in the aorta of the dog," *Circ. Res.*, Vol. 24, 1969, pp. 93-108.
- [71] Caro, C. G., Fitz-Gerald, J. M., and Schroter, R. C., "Atheroma and arterial wall shear: Observation, correlation and proposal of a shear dependent mass transfer mechanism for atherogenesis," *Proc. R. Soc. Lond. B. Biol. Sci.*, Vol. 177, 1971, pp. 109-159.
- [72] Gonzales, R. S., and Wick, T. M., "Hemodynamics modulation of monocytic cell adherence to vascular endothelium," *Ann. Biomed. Eng.*, Vol. 24, 1996, pp. 382-393.
- [73] Bao, X., Lu, C., and Frangos, J. A., "Temporal gradient in shear but not steady shear stress induces PDGF-A and MCP-1 expression in endothelial cells: Role of NO, NF kappa B, and egr-1," *Arterioscle.r Thromb. Vasc. Biol.*, Vol. 19, 1999, pp. 996-1003.
- [74] Reape, T. J., and Groot, P. H., "Chemokines and atherosclerosis," *Atherosclerosis*, Vol. 147, 1999, pp. 213-225.
- [75] Cheng, G. C., Briggs, W. H., Gerson, D. S., Libby, P., Grodzinsky, A. J., Gray, M. L., and Lee, R. T., "Mechanical strain tightly controls fibroblast growth-2 release from cultured human vascular smooth muscle cells," *Circ. Res.*, Vol. 80, 1997, pp. 28-36.

REFERENCES (continued)

- [76] Clowes, A. W., Reidy, M. A., and Clowes, M. M., –Mechanism of stenosis after arterial injury,” *Lab. Invest.*, Vol 49, 1983, pp. 208-215.
- [77] <http://radiopaedia.org/articles/intimal-hyperplasia> [cited March 22nd 2010]
- [78] Salsac, A. V., –Changes in the hemodynamics stresses occurring during the enlargement of abdominal aortic aneurysms,” Ph.D. Dissertation, University of California, San Diego, 2005.
- [79] Thubrikar M. J., Labrose M, Robicsek, F., Al-Soudi J., and Fowler, B., –Mechanical properties of abdominal aortic aneurysm wall,” *J. Med. Eng. Technol*, Vol. 25, 2001, pp. 133-142.
- [80] Davies P. F., Dewey, C. F., Bussolari, S., Gordon, E., and Gibrone M. A., –Influence of hemodynamic forces on vascular endothelial function,” *J. Clin. Invest.*, Vol. 73, 1984, pp. 1121-1129.
- [81] Chapell D. C., Verner, S. E., Nerem, R. M., and Alexander, R. W., –Oscillatory shear stress stimulates adhesion molecule expression in cultured human endothelium,” *Circ. Res.*, Vol. 82, 1998, pp. 532-539.
- [82] Nakatani, H., Hasimoto, N., Kang, Y., Yamazoe, N., and Kikichi, H., –Cerebral blood flow patterns at major vessel bifurcations and aneurysm in rates,” *J. Neuro. Surg.*, Vol. 74, 1991, pp. 256-262.
- [83] Fukuda, S., Hashimoto, N., Naritomi, H., Nagata, I., and Nozaki, K., –Prevention of rat cerebral aneurysm formation by inhibition of nitric oxide synthesis,” *Circulation*, Vol. 101, 2000, pp. 2535-2538.
- [84] Guzman, R. J., Abe, K., and Zarins, C., –Flow-induced arterial enlargement is inhibited by suppression of nitric oxide synthase activity in vivo,” *Surgery*, Vol. 122, 1997, pp. 273-279.
- [85] Griffith, T. M., –Modulation of blood flow and tissue perfusion by endothelium-derived relaxing factor,” *Exp. Physiol.*, Vol. 779, 1994, pp. 873-913.
- [86] Liepsch, D. W., –Flow in tubes and arteries: a comparison,” *Biorheology*, Vol. 23, 1986, pp. 395-433.
- [87] Crawford, T., –Some observations of the pathogenesis and natural history of intracranial aneurysms,” *J. Neurol. Neurosurg. Psychiatry.*, Vol. 22, 1959, pp. 259-266.

REFERENCES (continued)

- [88] Crompton, M., –Mechanism of growth and rupture in cerebral berry aneurysms,” *Br. Med. J.*, Vol. 1, 1966, pp. 1138-1142.
- [89] Taylor, T. W., and Yamaguchi, T., –Three-dimensional simulation of blood flow in an abdominal aortic aneurysm—steady and unsteady flow cases,” *J. Biomech. Eng.*, Vol. 116, 1994, pp. 89-97.
- [90] Scherer, P. W., –Flow in axisymmetrical glass aneurysm models,” *J. Biomech. Eng.*, Vol. 6, 1973, pp. 695-700.
- [91] <http://uvahealth.com/services/heart/treatment/14765> [cited 1st December 2010]
- [92] <http://indiahealthtour.com/treatments/cardiology/coronary-stenting-surgery.html> [cited 1st December 2010]
- [93] <http://www.vsegypt.org/index.php/vascular-surgery-cme/articles/133-peripheral-aneurysms.html> [cited 1st December 2010]
- [94] http://www.nhlbi.nih.gov/health/dci/Diseases/arm/arm_types.html [cited 1st December 2010]
- [95] <http://www.aneurysmsupport.com/types.html> [cited 1st December 2010]
- [96] http://www.eucatech.de/de/news/3D_MULTILAYER_TECHNOLOGY_.php [cited 1st December 2010]

APPENDIXES

APPENDIX A
UDF FOR STEADY CASE

```

/*****
LIST OF UDF FOR BIOFLUID COMPUTATIONS (FLUENT)
*****/

#include "udf.h"

/*****
UDF for Pulsatile velocity profile boundary condition
for a 3D / axisymmetric flow. x-Axis is the axis of symmetry
*****/

DEFINE_PROFILE(inlet_r_velocity, thread, position)

{

real p[ND_ND];
real r,x,y,z;
face_t f;

begin_f_loop(f, thread)

    {
        F_CENTROID(p, f, thread);
        x = p[0];
        y = p[1];
        z = p[2];
        r = sqrt(z*z + y*y);
        F_PROFILE(f, thread,position) =.1262*(1.-r*r/.000009);
    }

end_f_loop(f, thread)

}

```

APPENDIX B

UDF FOR PULSATILE CASE

```

/*****
LIST OF UDF FOR BIOFLUID COMPUTATIONS (FLUENT)
*****/

#include "udf.h"

/*****
UDF for specifying transient velocity profile boundary condition
for a 3D / axisymmetric flow. x-Axis is the axis of symmetry
*****/

DEFINE_PROFILE(Threed_Unsteady_Inlet_Velocity, thread, position)
{
    real x[ND_ND]; /* this will hold the position vector */
    real xx,yy,zz,r,radius,vmax,pi,Period;
    face_t f;
    real t = CURRENT_TIME;

    begin_f_loop(f, thread)
    {
        F_CENTROID(x,f,thread);
        xx = x[0];
        yy = x[1];
        zz = x[2];
        r = sqrt(yy*yy + zz*zz);

        pi = 3.14159265359;
        Period = 0.4;
        radius = 0.003;

        F_PROFILE(f, thread, position) = 0.25*( 1.0 + sin(2*pi*t/Period))*(1-
                                                (r/radius)*(r/radius));
    }
    end_f_loop(f, thread)
}

```